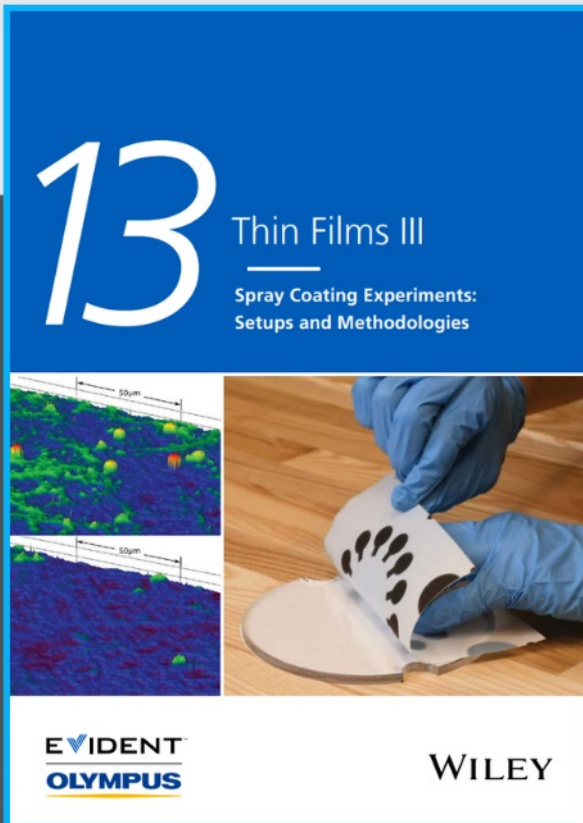




Spray Coating Experiments: Setups and Methodologies



**The latest eBook from
Advanced Optical Metrology.
Download for free.**

Spray Coating Experiments: Setups and Methodologies, is the third in our Thin Films eBook series. This publication provides an introduction to spray coating, three article digests from Wiley Online Library and the latest news about Evident's Image of the Year Award 2022.

Wiley in collaboration with Evident, are committed to bridging the gap between fundamental research and industrial applications in the field of optical metrology. We strive to do this by collecting and organizing existing information, making it more accessible and useful for researchers and practitioners alike.

EVIDENT
OLYMPUS

WILEY

Emerging 2D Copper-Based Materials for Energy Storage and Conversion: A Review and Perspective

Xuehua Ren, Haoyu Wang, Jun Chen, Weili Xu, Qingqing He, Huayu Wang, Feiyang Zhan, Shaowei Chen,* and Lingyun Chen*

2D materials have shown great potential as electrode materials that determine the performance of a range of electrochemical energy technologies. Among these, 2D copper-based materials, such as Cu–O, Cu–S, Cu–Se, Cu–N, and Cu–P, have attracted tremendous research interest, because of the combination of remarkable properties, such as low cost, excellent chemical stability, facile fabrication, and significant electrochemical properties. Herein, the recent advances in the emerging 2D copper-based materials are summarized. A brief summary of the crystal structures and synthetic methods is started, and innovative strategies for improving electrochemical performances of 2D copper-based materials are described in detail through defect engineering, heterostructure construction, and surface functionalization. Furthermore, their state-of-the-art applications in electrochemical energy storage including supercapacitors (SCs), alkali (Li, Na, and K)-ion batteries, multi-valent metal (Mg and Al)-ion batteries, and hybrid Mg/Li-ion batteries are described. In addition, the electrocatalysis applications of 2D copper-based materials in metal–air batteries, water-splitting, and CO₂ reduction reaction (CO₂RR) are also discussed. This review also discusses the charge storage mechanisms of 2D copper-based materials by various advanced characterization techniques. The review with a perspective of the current challenges and research outlook of such 2D copper-based materials for high-performance energy storage and conversion applications is concluded.

1. Introduction

With the aggravation of environmental pollution and the gradual exhaustion of non-renewable energy resources, development of clean and renewable energy technologies has been attracting


extensive interest,^[1–3] such as SCs,^[4] rechargeable ion batteries,^[5] water splitting,^[6] metal–air batteries,^[7] and CO₂RR.^[8] However, the practical applications of SCs and rechargeable ion batteries are limited by low energy density and low power density, respectively.^[9,10] The multiple-electron transfer reactions in water splitting have posed a significant challenge that limits the catalytic efficiency and cycle stability.^[11] At present, the urgent issue of metal–air battery is to design high-performance bifunctional electrodes.^[12] For CO₂RR, the technical realization is limited by the activity and selectivity of the catalyst, and the selectivity of its product beyond that of CO.^[13,14] In these electrochemical devices, electrodes represent the core component, which dictates the efficiency, energy and power density, as well as catalytic activity and durability.

Since the birth of graphene, 2D materials have attracted great attention due to their unique electrochemical, mechanical, and optical properties and diverse applications, as manifested in over 3000 academic papers each year.^[15,16] 2D materials possess some structural advantages

over the 0D and 1D counterparts by interlayer gap bonding and weak out-of-plane Van der Waals interaction, which provides an interesting platform for energy storage and conversion research.^[17,18] So far, the 2D material family mainly includes transition metal dichalcogenides, transition metal carbides, layered metal oxides, layered double hydroxides and other graphene-like materials, such as black phosphorus. Of these, copper-based materials have received extensive attention because of high natural abundance, low price, high strength, arc erosion resistance, easy preparation of various nanoshapes, wear resistance, etc. (Figure 1),^[19,20] leading to excellent electrochemical performance and advancement of electrochemical energy storage and conversion (Figure 2). For example, with a large surface area and potential size effect, CuO nanostructures, a p-type semiconductor, have excellent physical and chemical properties for SCs, as well as interesting magnetic and superhydrophobic properties, as compared with other metal oxides, such as TiO₂, ZnO, WO₃, and SnO₂.^[21] Cu–S compounds are a promising lithium cathode with a high energy density and long cycling stability.^[22] Cu–Se is also considered as a novel cathode

X. Ren, H. Wang, J. Chen, W. Xu, Q. He, H. Wang, F. Zhan, L. Chen
Department of Applied Chemistry
School of Chemistry and Chemical Engineering
Chongqing University
Chongqing 401331, P. R. China
E-mail: lychen@cqu.edu.cn

S. Chen
Department of Chemistry and Biochemistry
University of California
1156 High Street, Santa Cruz, CA 95060, USA
E-mail: shaowei@ucsc.edu

 The ORCID identification number(s) for the author(s) of this article can be found under <https://doi.org/10.1002/smll.202204121>.

DOI: 10.1002/smll.202204121

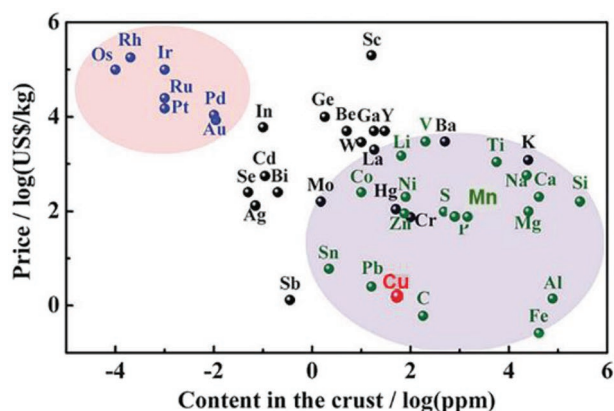


Figure 1. Material costs obtained from the Handbook of Chemistry and Physics versus natural abundance in the earth's crust of various elements (noble elements: blue, common elements: olivine, Cu element: red, other elements: black; noble element zone: light pink, satisfactory element zone: light purple). Reproduced with permission.^[26] Copyright 2015, The Royal Society of Chemistry.

material for batteries, because of the “softer” selenide anions than oxides and sulfides, which is beneficial to the construction of the cathode skeleton.^[23] Cu–N and Cu–P have also been recently studied in both water splitting and CO₂RR.^[24,25]

However, there are certain limitations and nonoptimal electrochemical properties with copper-based materials in energy-related applications, which are mainly related to the composition, crystal phase, and morphology.^[27] Experimentally, the morphology can be controlled by the synthesis process and parameters, such as hydrothermal method, sol-gel route, and electrodeposition.^[28] Further structural engineering can be achieved by defect design, heterostructure fabrication, and surface functionalization, where the materials structures can be characterized by various techniques, including in situ microscopy, X-ray, and vibration analysis.^[29]

There have been several previous reviews on the applications of copper-based materials in energy-related technologies. For instance, Zhang et al. discussed the recent progress and emerging challenges of CuO nanostructures.^[21] Mustaqeem and co-workers summarized the architecture design for improving the specific capacitance, power density, cycling stability, multifunctional capabilities of CuO-based materials in SC applications.^[30] Gawande et al. reviewed the performance of Cu and copper-based nanoparticles for electrocatalysis, photo-

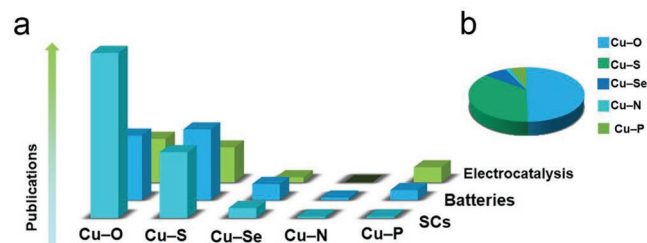


Figure 2. a) Number of publications of 2D copper-based materials for electrochemical energy storage and conversion in the last ten years. b) Pie chart of the percentage of different copper-based materials for electrochemical energy storage and conversion in the total publications within the past ten years.

catalysis, or gas-phase catalysis.^[31] However, as far as we know, there has been no review focusing on the emerging 2D copper-based electrode materials.

Herein, we provide a comprehensive review of the development of 2D copper-based materials for electrochemical energy storage and conversion (Figure 3). Figure 4 shows the timeline of the development of 2D copper-based materials for energy storage and conversion. It is worth noting that the 2D materials introduced in this review include not only conventional 2D materials like metal hydroxides, LDHs and MOFs, but also nanostructured materials like nanosheets, nanodisks, and nanoplates. These materials can be further exploited for the construction of 3D nanostructures for more complicated structural modifications. Specifically, 2D copper-based materials, such as Cu–O, Cu–S, Cu–Se, Cu–N, and Cu–P, will be discussed as electrode materials and electrocatalysts. After a brief introduction of their crystal structures and synthesis methods, optimization strategies will be presented and discussed to improve the electrochemical performance within the context of the reaction mechanism. Finally, remaining challenges and opportunities of further research are put forward, so as to further the exploration of 2D copper-based materials for the advancement of electrochemical energy technologies.

2. Crystal Structures

The crystal structure of electrode materials has an important influence on electrochemical performance. Cu–O compounds mainly consist of CuO and Cu₂O. Both are p-type semiconductors having a tunable bandgap energy of 1.22–1.55 eV and 2.0–2.40 eV, hole mobility of 0.1–10 cm² V⁻¹ s⁻¹ and 250 cm² V⁻¹ s⁻¹, respectively. CuO is more stable than Cu₂O and hence more important in practical applications.^[30] Cu₂O possesses a cubic structure with the space group *Pn3m*, belonging to the isometric system. The cubic structure consists of close packing of copper atoms and tetrahedral positions of cubic lattice positions ($\frac{3}{4}, \frac{3}{4}, \frac{3}{4}$) and ($\frac{1}{4}, \frac{1}{4}, \frac{1}{4}$), in which the coordination of copper atoms is half of that of the oxygen atoms.^[32] Therefore, the tetrahedron of a copper atom surrounds each oxygen atom, and each copper atom has two adjacent oxygen atoms (Figure 5a).^[33] Cu₂O has found diverse applications in the fields of catalysis, gas sensors, photovoltaics, magnetic semiconducting electronics, batteries, etc.^[34] It is well known that CuO exhibits the *C62h* symmetry, and the coordination number of copper is 4, where each unit of copper oxide is composed of four formula units.^[35] On the (110) plane (Figure 5b), four oxygen atoms are coplanar and surrounded by copper in the form of a twisted tetrahedron, forming a rectangular parallelogram. Figure 5c depicts the crystal structure of CuO (the monoclinic space group *C2/c*), with four units in the elementary cell ($a = 4.68 \text{ \AA}$, $b = 3.42 \text{ \AA}$, $c = 5.13 \text{ \AA}$, $a = \beta = 90^\circ$, $\gamma = 99.5^\circ$).^[35] CuO has also found applications in solar cells, magnetic phase transitions, catalysis, electrocatalysis, photoelectrochemical oxidations, gas sensors, batteries, and SCs.^[36]

The Cu–S compounds (Cu_{2–x}S, $x = 0–1$) exhibit many different stoichiometric compositions, with phases varied from the copper-rich side to the copper-deficient side, including Cu₂S,

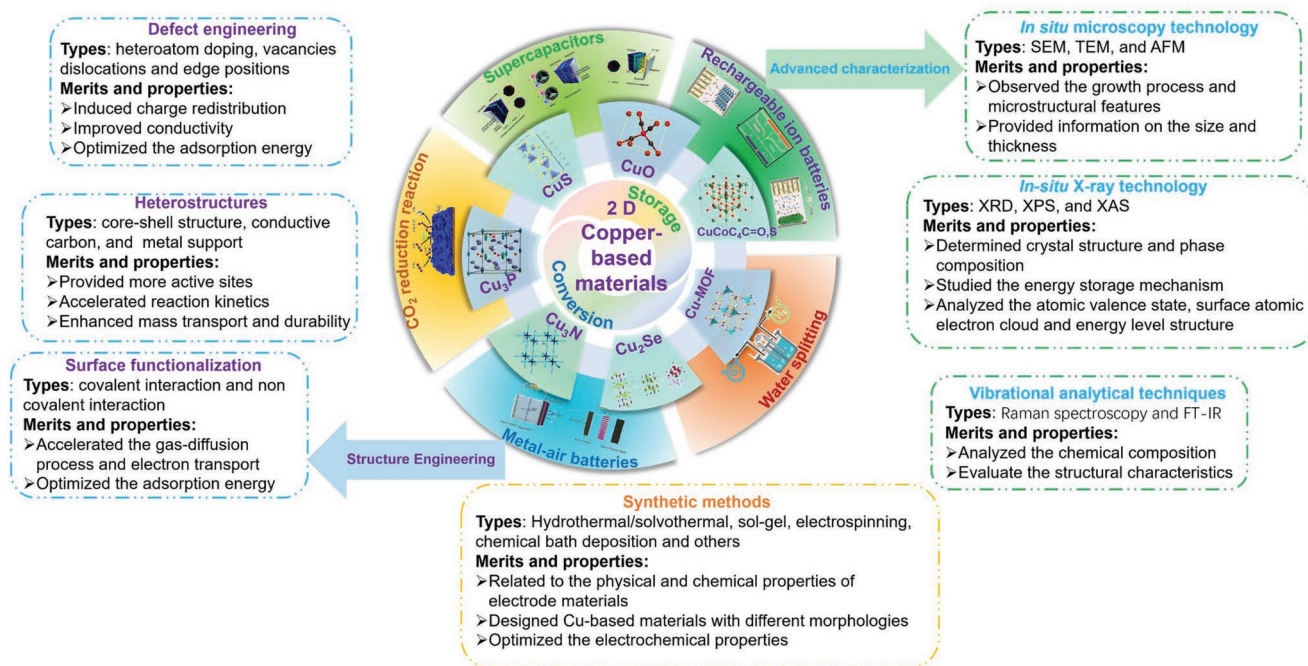


Figure 3. Overview of copper-based materials for electrochemical energy storage and conversion.

$\text{Cu}_{1.94}\text{S}$, $\text{Cu}_{1.81}\text{S}$, $\text{Cu}_{1.8}\text{S}$, $\text{Cu}_{1.75}\text{S}$, and CuS (Figure 5d–k).^[37–39] Copper deficiency generates free holes in the valence band of the material, making it a self-doped p-type semiconductor, and the bandgaps (1.2–2.4 eV) varies with the stoichiometry (x value).^[40] Cu^+ in chalcocite Cu_2S only occupies the trigonal centers of S^{2-} . Under environmental conditions, Cu_2S tends to lose copper ions, leaving behind undercoordinated S^{-1} . The

further loss of Cu^+ leads to the formation of disulfide bonds and the increase of hole concentration in the valence band, hence an increase of the conductivity. The degree of disulfide bond formation is also an indicator of copper ion mobility.^[41] With the increase of disulfide bond concentration, copper ions are more likely to occupy the tetrahedron center and lose their mobility. Heavily cation-deficient Cu_{2-x}S exhibits strong optical

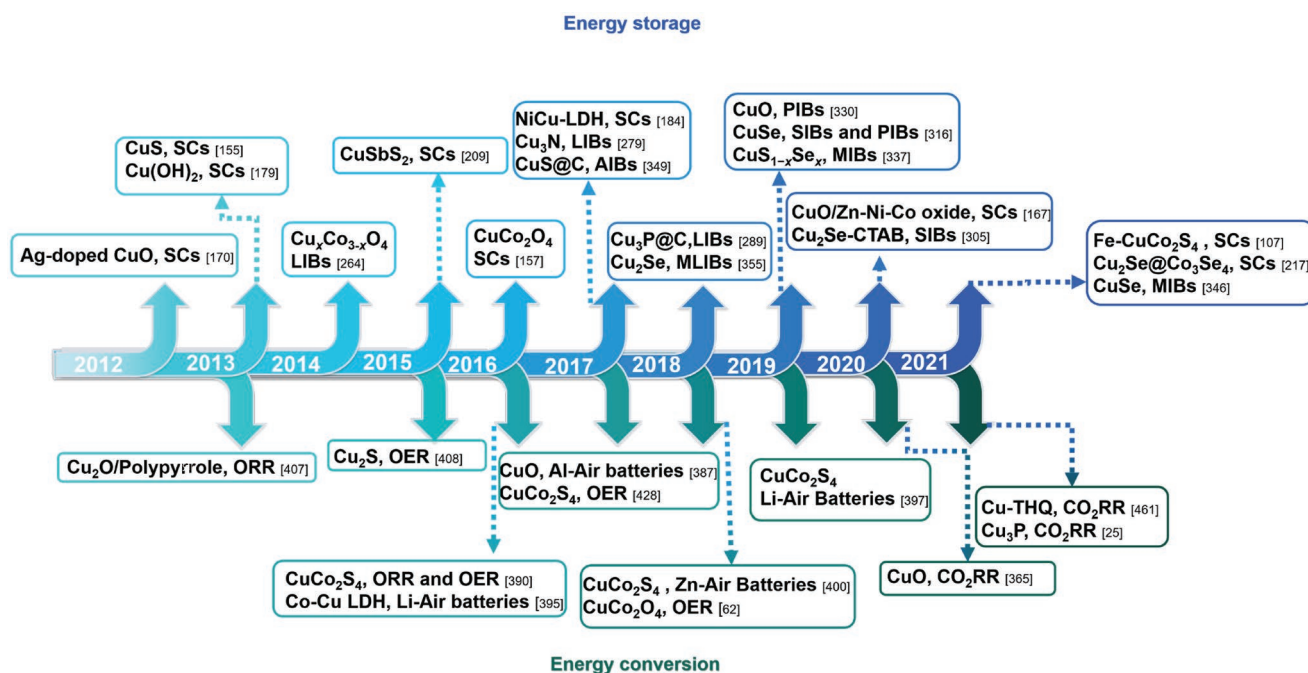


Figure 4. Timeline of the development of 2D copper-based materials in the field of electrochemical energy storage and conversion in the past ten years.

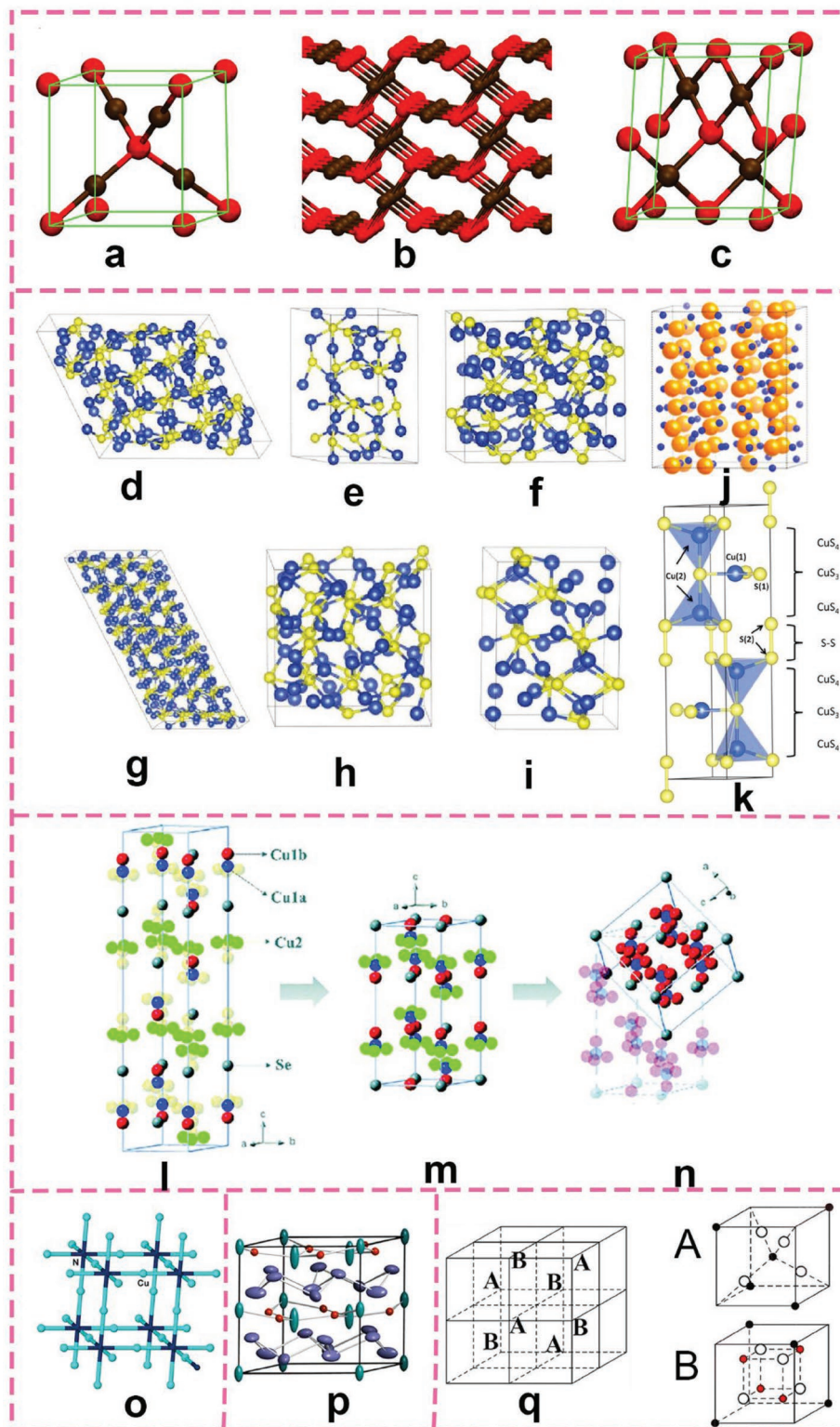


Figure 5. a) Crystal structures of cuprous oxide Cu_2O . b) Cupric oxide CuO . c) Side views of CuO (110). d) Crystal structures of Low-chalcocite Cu_2S . e) High-chalcocite Cu_2S . f) Cubic-chalcocite Cu_2S . g) $\text{Cu}_{1.94}\text{S}$, h) $\text{Cu}_{1.8}\text{S}$. i) $\text{Cu}_{1.75}\text{S}$., j) $\text{Cu}_{1.81}\text{S}$. k) CuS . l) Symmetry-related phase transitions in $\alpha\text{-Cu}_{2-x}\text{Se}$, m) Intermediate structure with symmetry increment. n) High-temperature $\beta\text{-Cu}_{2-x}\text{Se}$. o) Crystal structures of Cu_3N , p) Cu_{3-x}P , q) The unit cell structure of the spinel CuCo_2C_4 . a–c) Reproduced with permission.^[33] Copyright 2015, Elsevier. d–i) Reproduced with permission.^[37] Copyright 2012, American Institute of Physics. j) Reproduced with permission.^[38] Copyright 2016, American Chemical Society. k) Reproduced with permission.^[39] Copyright 2014, American Chemical Society. l–n) Reproduced with permission.^[47] Copyright 2017, International Union of Crystallography. o) Reproduced with permission.^[48] Copyright 2021, Elsevier. p) Reproduced with permission.^[50] Copyright 2018, American Chemical Society. q) Reproduced with permission.^[51] Copyright 2020, Elsevier.

absorption in the near-infrared region, due to localized surface plasmon resonance. Copper sulfides are of great significance in a wide range of applications, including sensors, photocatalysis, thermoelectronics, optoelectronic devices, solar cells, and SC.^[42] Especially, Cu₂S and CuS with good electrical conductivities, e.g., $8.3 \times 10^{-4} \text{ S cm}^{-1}$ for Cu₂S and $9.5 \times 10^{-3} \text{ S cm}^{-1}$ for CuS,^[43] are considered to be promising materials in advanced energy storage applications, due to their good crystal structure, conductivity, high theoretical charge capacity and outstanding discharge characteristics. There are three phases with Cu₂S. The monoclinic phase with space group *P21/c* (low chalcocite, $a = 15.27 \text{ \AA}$, $b = 11.93 \text{ \AA}$, and $c = 13.45 \text{ \AA}$) is formed below 104 °C (Figure 5d), the hexagonal phase with space group *P63/mmc* (high chalcocite, $a = 7.87 \text{ \AA}$, $b = 8.19 \text{ \AA}$, and $c = 13.36 \text{ \AA}$) is formed between 104 °C and 436 °C (Figure 5e), and the cubic phase (orthodontic chalcocite, $a = 12.04 \text{ \AA}$, $b = 12.26 \text{ \AA}$, and $c = 10.04 \text{ \AA}$) is formed above 436 °C (Figure 5f).^[44] CuS has a complex crystal structure with the space group *P6₃/mmc*. As shown in Figure 5k, Cu and S atoms have two different crystallographic sites, namely Cu(1), Cu(2), S(1), and S(2). CuS is composed of alternating layers of CuS₃ units (tetrahedral coordination with S(1) and S(2) atoms triangles) and CuS₄ units (triangular symmetry tetrahedra) linked together by the S–S bonds along the *c*-axis.^[22] The lattice constants are $a = 3.7851 \text{ \AA}$, $b = 3.792 \text{ \AA}$, and $c = 16.102 \text{ \AA}$.

Similar to CuS, Cu–Se consists of various stoichiometric and nonstoichiometric phases, including cubic berzelianite (Cu₂Se, Cu_{1.8}Se and Cu_{2-x}Se), hexagonal klockmannite (CuSe and Cu_{0.87}Se), tetragonal umangite (Cu₃Se₂), and orthorhombic atabascaite (Cu₅Se₄ and CuSe).^[45] Cu₂Se possesses a β -phase (monoclinic structure) with the space group of *C2/c* at low-temperature and a high-temperature α -phase (cubic structure) with the space group of *Fm $\bar{3}$ m*, and the exact transition temperature depending on the degree of copper deficiency.^[46] Figure 5l shows the symmetry-related phase transitions of Cu_{2-x}Se, as viewed from above, where the layered structure is composed of copper-rich layer and copper-deficient layer alternately along the *c*-axis.^[47] When the temperature rises, a small amount of Se rearranges and copper ions migrate from the copper-rich layer to the copper-deficient layer, forming β -Phase Cu₂Se with an antifluorite cubic cell (Figure 5m,n), which involves a rigid face centered cubic sublattice formed by Se atoms and a less dependent sublattice composed of disordered Cu ions at tetrahedral and randomly distributed triangular sites.

Cu₃N exhibits a cubic anti-ReO₃ structure with a space group of *pm $\bar{3}$ m* (Figure 5o).^[48] Each N atom is coordinated by six Cu atoms, and each Cu atom is linked to two N atoms. Due to the existence of the empty body center interstitial sites, Cu₃N can accommodate other metal atoms to adjust its optical and electrical properties.^[49] Cu_{3-x}P shows an acentric hexagonal crystal structure with a space group of *P6₃cm* (Figure 5p), with the corresponding lattice parameters of $a = b = 6.959 \text{ \AA}$, $c = 7.143 \text{ \AA}$.^[50] CuCo₂O₄ and CuCo₂S₄ belong to the spinel structure, conforming to the general structural formula of CuCo₂C₄, where C represents O and S. Zhao et al. described the structural unit of spinel, which is composed of eight small cubic units connected by four A-type units and four B-type units (Figure 5q).^[51] There are 32 cubic C in the unit cell, which occupy four effective lattice points of face centered cubic and

distribute uniformly in each A-type and B-type unit. Cu ions fill the tetrahedral voids (the center and half of the vertices of type A units and the half of the vertices of type B units), the 16 Co ions in the unit cell occupy half of the octahedral space in the O-dense packing, while S/O is at the polyhedral vertices. Therefore, the general cell formula of copper-based spinels is Cu₈Co₁₆C₃₂ and the chemical formula is simplified to CuCo₂C₄.

3. Synthesis

To date, a variety of methods have been reported for the preparation of copper-based nanostructures, including hydrothermal/solvothermal, sol-gel, chemical vapor deposition (CVD), microwave irradiation, successive ionic layer adsorption and reactions (SILAR), electrospinning, chemical bath deposition (CBD), and spray pyrolysis (Table 1), with different pros and cons (Figure 6). The crystal structure, composition, morphology, and size of 2D porous materials can be successfully controlled by various experimental parameters, such as reaction methods, molar ratio of reactant ions, concentration, pH value of reaction solution, heating temperature and reaction time. In hydrothermal method, for example, the strong polarity of water may be favorable to the oriented growth of nanocrystals.^[52] In fact, CuO nanostructures of various morphologies have been prepared by hydrothermal method, exhibiting different optical, electrical and catalytic properties.^[53–55] Gao et al. reported that the temperature in the hydrothermal treatment remarkably influenced the crystalline structures and morphology of CuO nanorods.^[56] In this section, we do not intend to summarize all the reported preparation methods in detail, but mainly emphasize several commonly used methods.

3.1. Hydrothermal/Solvothermal Method

Hydrothermal method refers to the chemical reaction in aqueous solutions above the boiling point of water, while solvothermal method is carried out in non-aqueous solutions at high temperatures.^[57] Importantly, the reaction can be carried out at a temperature higher than the normal boiling point of the solvent, which cannot be achieved in other synthesis methods. The resultant nanomaterial structures can be affected by the reactant concentration, reaction media, solution pH, reaction time, and temperature.^[58] To prevent recrystallization or nanoparticle aggregation, Demel and co-workers prepared CuO nanosheets by stratifying acetate and converted the hydroxide into oxide by in situ dissolution in 1-butanol.^[59] Maier et al. demonstrated that with polyvinylpyrrolidone (PVP) as the shape control agent, the morphologies of CuCo₂O₄ evolved from nanowires to nanosheets with the increase of reaction time (Figure 7a).^[60] In another study, Gao et al. fabricated CuCo₂O₄ nanomaterials using different alkali sources and NH₄F doses,^[61] producing completely different morphologies (Figure 7b–d). CuCo₂O₄ could be transformed from porous 2D nanosheets through cubes and particles to condensed spheres by using different solvents.^[62] However, at relatively high temperatures and pressures, the reactivity and solubility of the reactants will be greatly

Table 1. Comparison with different synthesis methods of copper-based materials.

Synthesis	Influencing factors	Products	Characteristics	Morphology	Products applications
Hydrothermal/ solvothermal	The type of precursors, pH, growth time, and growth temperature	Copper-based materials	Uniform products with fine-tuned morphology and size	Nanoparticles/wires/rods/tubes/sheets/blades, and 3D nanoarchitectures	Sensing, catalysis, SCs, batteries, photovoltaics
Sol-gel	The type of precursors, reaction time and temperature, and solution pH	CuO, CuS, Cu ₂ S, Cu ₂ Se, CuCo ₂ O ₄	Uniform product	Nanoparticles/sheets, and 3D architectures	Sensing, catalysis, SCs, batteries
CBD	The type of precursors, reaction, temperature, reactant concentration, and surfactant	CuO, CuS, Cu ₂ S, Cu ₂ Se, CuSe	Be apt to agglomerate; phase-pure single crystallites	Nanoparticles/wires/belts/platelets/sheets	Catalysis, SCs, batteries, photovoltaics
SILAR	Adsorption and rinsing durations, temperature, etc. control the stoichiometry of the deposited system	CuO, Cu ₂ O, CuS, Cu ₂ S	Homogeneous, compact and of uniform thickness, properties of porosity	Films and nanorods	Catalysis, SCs, batteries, photovoltaics
Electrospinning	Solution concentration, viscosity, temperature, humidity, voltage, flow rate, distance between needle and collector	CuO, CuS, Cu ₃ N, CuCo ₂ O ₄	Highly crystalline with low crystal defects	Nanofibers/wires/rods/sheets	Photovoltaics, catalysis
Sputtering techniques	Sputtering parameters such as the partial pressure of the reactive gas	Cu ₂ O, CuO, Cu ₃ N	High purity, density, and good uniformity	Films	Photovoltaics, catalysis
Spray pyrolysis	Temperature of the heated substrate; Solution concentration	Cu ₂ O, CuO, CuS, Cu ₂ S	Uniform and vertically aligned with low impurity	Films	Photovoltaics, sensors

increased, resulting in impure products and low yield, along with risks during the experimental procedure.^[63]

3.2. Sol-Gel Method

The sol-gel method is a low-temperature humidification method used to prepare highly reproducible metal compounds

by homogeneously mixing materials, especially for controlling their shape, texture, and surface properties, which usually converts the solution of metal precursors into a sol, and then into a gel, and has been widely used for the preparation of glass, ceramics, nanosheets, nanoparticles, and so forth.^[64,65] For example, Kadi and Mohamed synthesized CuO nanosheets using copper nitrate as the copper source and F₁₂₇ triblock copolymer to shape the oriented nanosheets.^[66] Usha et al.

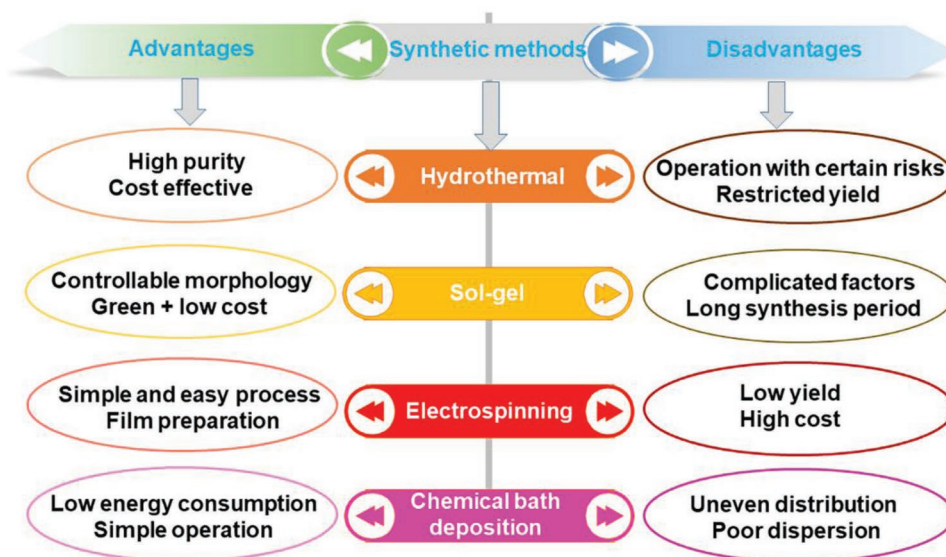


Figure 6. Advantages and disadvantages of several commonly used synthesis methods.

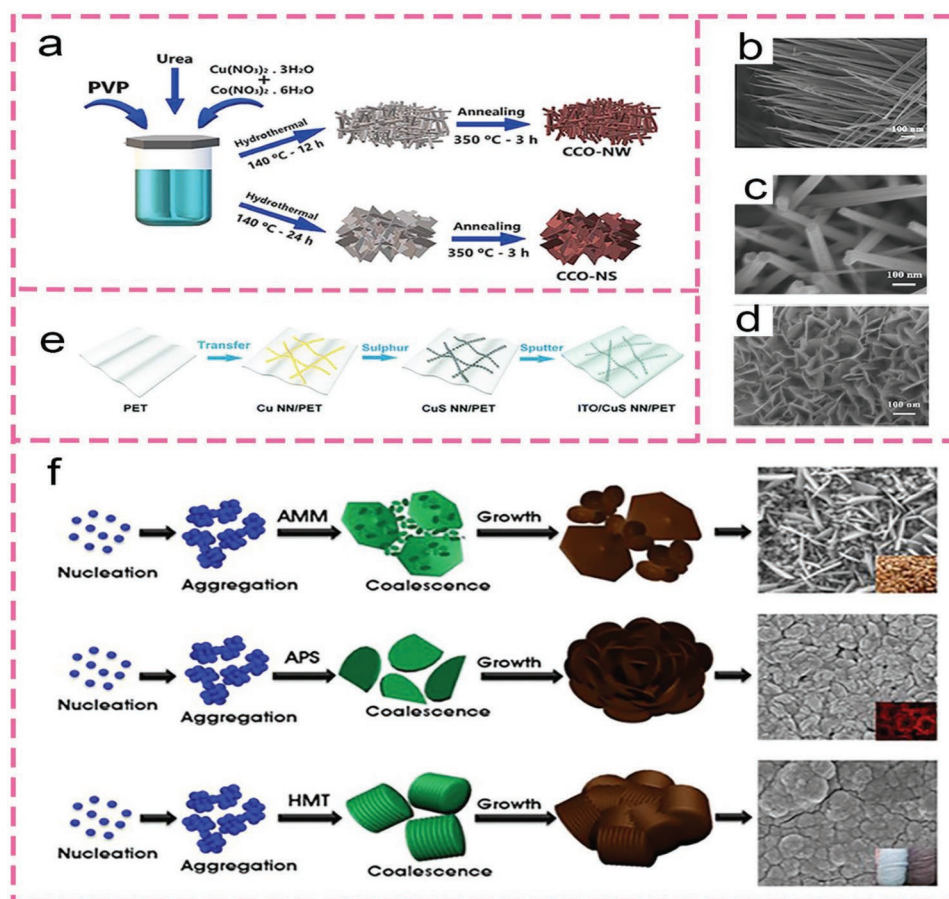


Figure 7. a) Schematic illustration of the formation of CCO-NW and CCO-NS. b) Scanning electron microscope (SEM) images of CuCo₂O₄ nanoneedle. c) Nanorod and d) nanosheet arrays. e) The schematic image of the fabrication processes of the transparent ITO/CuS NN composite film. f) Schematic illustration of formation mechanism of nanosheets as well as micro-rose and micro-woolen-like arrangement of nanosheets. a) Reproduced with permission.^[60] Copyright 2019, Elsevier. b–d) Reproduced with permission.^[61] Copyright 2019, Elsevier. e) Reproduced with permission.^[72] Copyright 2016, The Royal Society of Chemistry. f) Reproduced with permission.^[76] Copyright 2013, Elsevier.

successfully prepared CuO nanostructure by using CuCl₂, NaOH or KOH as the main precursors, and the crystallinity of CuO prepared with NaOH was better than that with KOH.^[67] Yuan et al. demonstrated a facile sol-gel method without complex craft to synthesize various CuO nanocrystalline at room temperature,^[68] and observed a change of CuO morphology with precursor concentration and reaction time.

3.3. Electrospinning Method

Electrospinning is a continuous, simple, universal electrostatic field-assisted spinning technology, which is used to prepare ultraclean fibers with a high specific surface area, porosity and small diameter for biomedical, food engineering, energy storage and conversion applications.^[69] The material structures can be affected by the molecular weight, temperature, humidity, solution concentration, and conductivity of the polymers.^[70] In recent years, the electrospinning technique, in combination with other synthetic methods, has been widely used in the preparation of copper-based composites. For example, polyaniline (PAN)–CuS hierarchical heterostructures are synthesized

in situ on PAN fibers prepared by electrospinning through a simple hydrothermal sulfuration growth process, exhibiting a “flowering branches” morphology.^[71] Zhang et al. synthesized flexible indium-doped tin oxide (ITO)/CuS nanosheet network films by combining the electrospinning and sputtering techniques (Figure 7e).^[72]

3.4. Chemical Bath Deposition

CBD is suitable for industrial production because of its cheap raw materials, low energy consumption, and simple operation.^[73] Yet critical issues remain, such as uneven distribution, large particle size, and poor dispersibility. Therefore, it is important to add surfactants, dispersants, and other additives to optimize the process conditions in combination with other synthesis methods to improve the product performance.^[74] Sudha et al. demonstrated that CuO nanosheets were formed from CuCl₂ 2H₂O and polyethylene glycol (PEG).^[75] It is noteworthy that PEG could control the growth process of CuO by adjusting the viscosity of the solution. However, the low yield of this method limits the application. Dubal et al. synthesized

different CuO nanostructures through CBD using various complexing agents at 343 K without any surfactant (Figure 7f).^[76] They obtained microwoolen-like CuO nanosheets of 10–40 nm in thickness, which gathered together to form a uniform surface morphology. In an alkaline environment, these metal salt chelated effectively avoiding uniform nucleation after metal ion binding, and facilitated heterogeneous nucleation, which was helpful to improve the yield. Likewise, CuS counter electrodes were synthesized via CBD on a fluorine-doped tin oxide (FTO) substrate for different deposition times.^[77] When the deposition time was 60 min, CuS with a dense nanoplatelet structure and non-porosity exhibited good adhesion to the FTO matrix in the presence of HCl. In another study, Shinde and co-workers synthesized CuO nanosheets and studied the effects of ionic liquids on the morphological evolution.^[78]

3.5. Others

There are other methods for preparing copper-based materials. CVD method can produce 2D materials of high-quality and large lateral size,^[79] because it is based on direct deposition of heterogeneous nucleation and does not require any post-treatment, such as annealing or coating with other materials. It is mainly used for the deposition of metal oxide films

by immersing a matrix into a water bath of metal ion composites.^[80] In addition, as an adhesive-free technology, the electrodeposition method allows for low-temperature and large-scale preparation, and can produce uniform and tunable morphology. Carbonized cloth, Ni foam, and so on can be used as the structural framework, avoiding the use of adhesives. As depicted in Figure 8a, carbonized cloth with remarkable conductivity could not only serve as the structural skeleton of composite materials, but also as a collector of CuS active materials, which provided a large active center for material growth.^[81] Different from depositing CuS on carbonized cloth, 3D Cu₂Se nano-cauliflower with 2D CuS nanosheets as a composite was successfully fabricated via a simple electrodeposition method on Ni foam.^[82] In some cases, electrodeposition is used to generate intermediates before final products are obtained by post-treatments, such as thermal annealing.^[83]

SILAR consists of a layer by layer growth mode,^[84] based on alternating immersion of a substrate into cationic and anionic precursor solutions.^[85] Annealing temperature has been known to affect the surface morphology, uniformity, density and smoothness of the synthesized nanomaterials.^[86] For typical colloidal synthesis, under inert conditions, organic anions and metal salts or organic metal precursors are combined with organic solvents with boiling points up to 360 °C as the metal sources.^[87] It usually includes heating in the presence

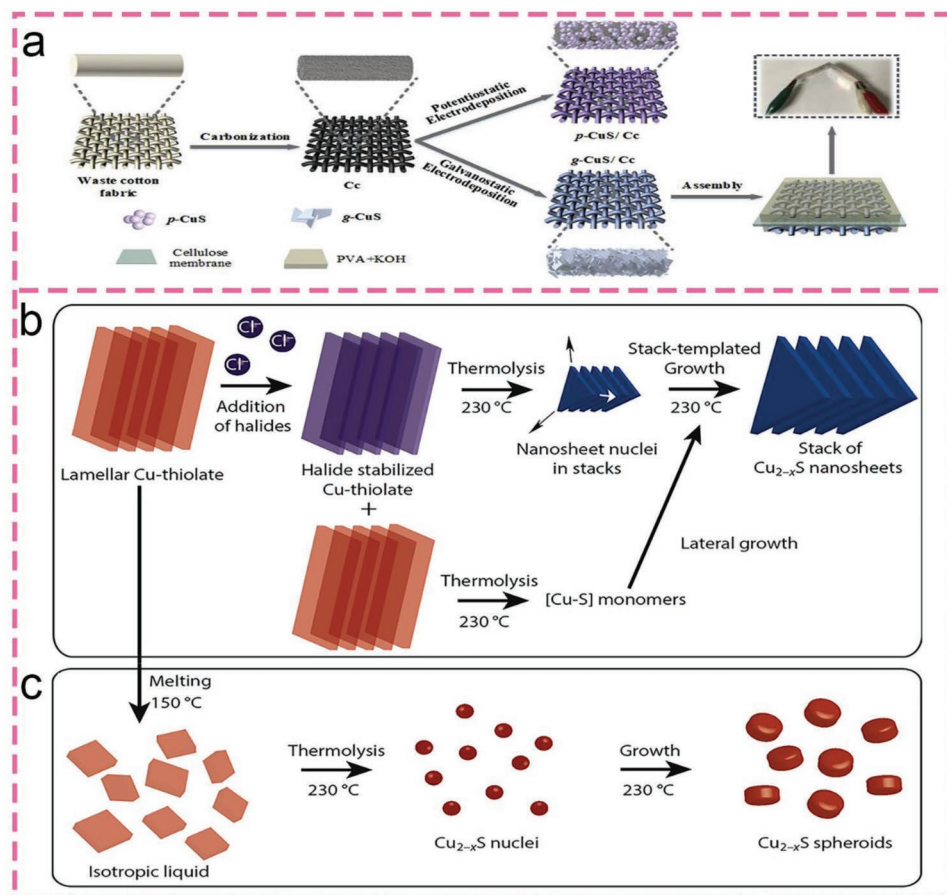


Figure 8. a) Schematic illustration of the preparation process of p-CuS/Ccs, g-CuS/Cc and g-CuS/Cc-SC. b) Formation of ultrathin Cu_{2-x}S nanosheets. c) Cu_{2-x}S nanocrystals. a) Reproduced with permission.^[81] b,c) Reproduced with permission.^[90] Copyright 2016, American Chemical Society.

of ligands and organic solvents, and thermal injection that induces supersaturation by generating a temperature gradient between anions and metal precursors. A key advantage of this method is that the optical and electronic properties of colloidal nanocrystals can be adjusted by controlling the size, shape, and composition. Vikulov et al. synthesized klockmanite CuSe nanosheets with lateral dimensions up to 3 μm and conductivity up to 645 S m^{-1} .^[88] In addition, some foreign ions, such as metal ions, halide ions, and exogenous seeds, can be used to control and tune the morphology of semiconductor nanocrystals.^[89] Van der Stam et al. showed that the lamellar stacks of copper-thiolate precursor complexes were generally melted at about 150 $^{\circ}\text{C}$, but remained intact in the presence of chlorides up to 230 $^{\circ}\text{C}$.^[90] The thermal stability of the Cl^{-} modified complexes ensured the structural integrity of the layered stack after Cu-catalyzed thermolysis, resulting in the nucleation in the 2D lamellar template formed thin nanosheets of Cu_{2-x}S (Figure 8b,c).

4. Strategies for Enhancing Electrochemical Performance

Defect engineering, heterostructure construction, and surface functionalization are the three major strategies for structure engineering of copper-based materials (Figure 9). They can adjust the material electronic structure leading to optimized characteristics and functions.^[91] This section presents recent advances in the structural engineering of copper-based materials and their applications in energy storage and conversion.

4.1. Defect Engineering

Defect engineering has been proved by experiment and theory to be an effective method to modify the surface and change

the electronic properties of copper-based materials, by not only inducing charge redistribution, improving conductivity, but also optimizing the adsorption energy of the materials.^[92] Defects exist in many forms, such as heteroatom doping, vacancies, dislocations, and edge positions.

Doping a small amount of metal and non-metal atoms is a promising strategy to improve the electrochemical activity of copper-based materials.^[93] For instance, inspired by the good connectivity between the collector and the Cr-doped CuO film, Durai et al. adjusted the material conductivity by Cr doping, and realized a higher area capacitance than that of pristine CuO.^[94] Defects are usually considered as active centers in the electrocatalytic process of 2D nanomaterials, and the type, quantity, and location of doping atoms greatly affect the catalytic performance.^[95] Ma et al. systematically studied the effect of bimetallic doping on Cu_2MoS_4 interface engineering and electronic modulation.^[96] Simultaneous doping of Ni and Co narrowed the nanomaterials bandgap, and facilitated the transition of electrons in Cu_2MoS_4 from the valence band to the conduction band. Nonmetallic doping has also been proved to be beneficial for electrocatalysis. Zhang et al. synthesized multilamellar mesoporous CuO nanosheets through Br^{-} doping and cetyltrimmonium (CTA^{+}) cation adsorption,^[97] where the Br^{-} dopants not only tuned the electronic structure of the catalyst to the optimal state, but also reduced the activation energy of CO_2 molecules and adjusted the intermediate species and their adsorption state, which facilitated the conversion of the $^*\text{OCH}_2\text{CH}_3$ intermediate to $\text{C}_2\text{H}_5\text{OH}$ (Figure 10a).

Production of vacancies has also been proved to be effective in adjusting the energy band structure and regulating the electronic environment in the close proximity.^[98,99] Target-oriented generation of anionic vacancies in the lattice of active materials can change the electrical properties and increase electrochemical active sites.^[100] Oxygen vacancies (OVs) can exist in copper-based materials as point defects.^[101] The existence of OVs

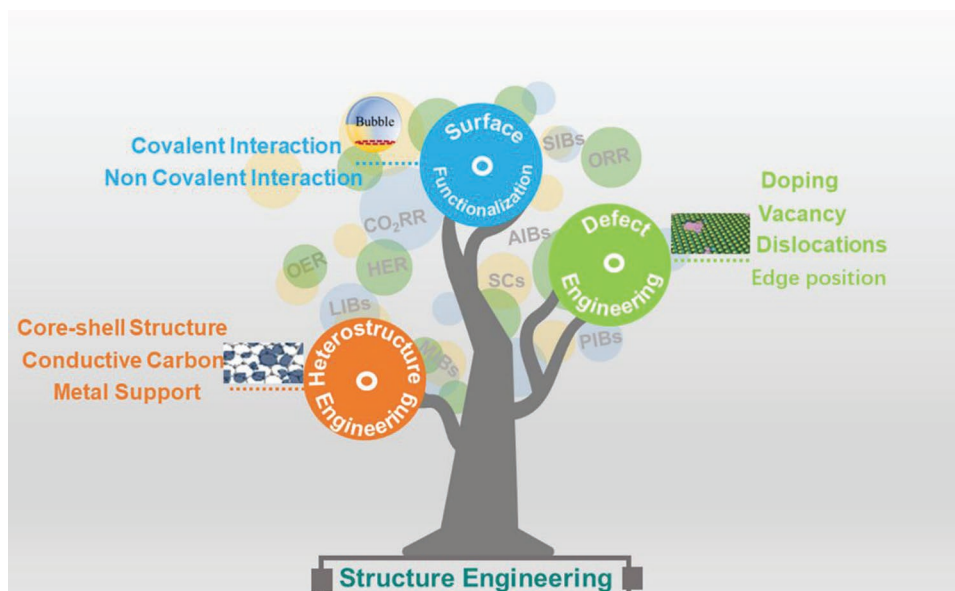


Figure 9. Schematic illustration of structure engineering strategies for 2D copper-based materials toward sustainable energy devices.

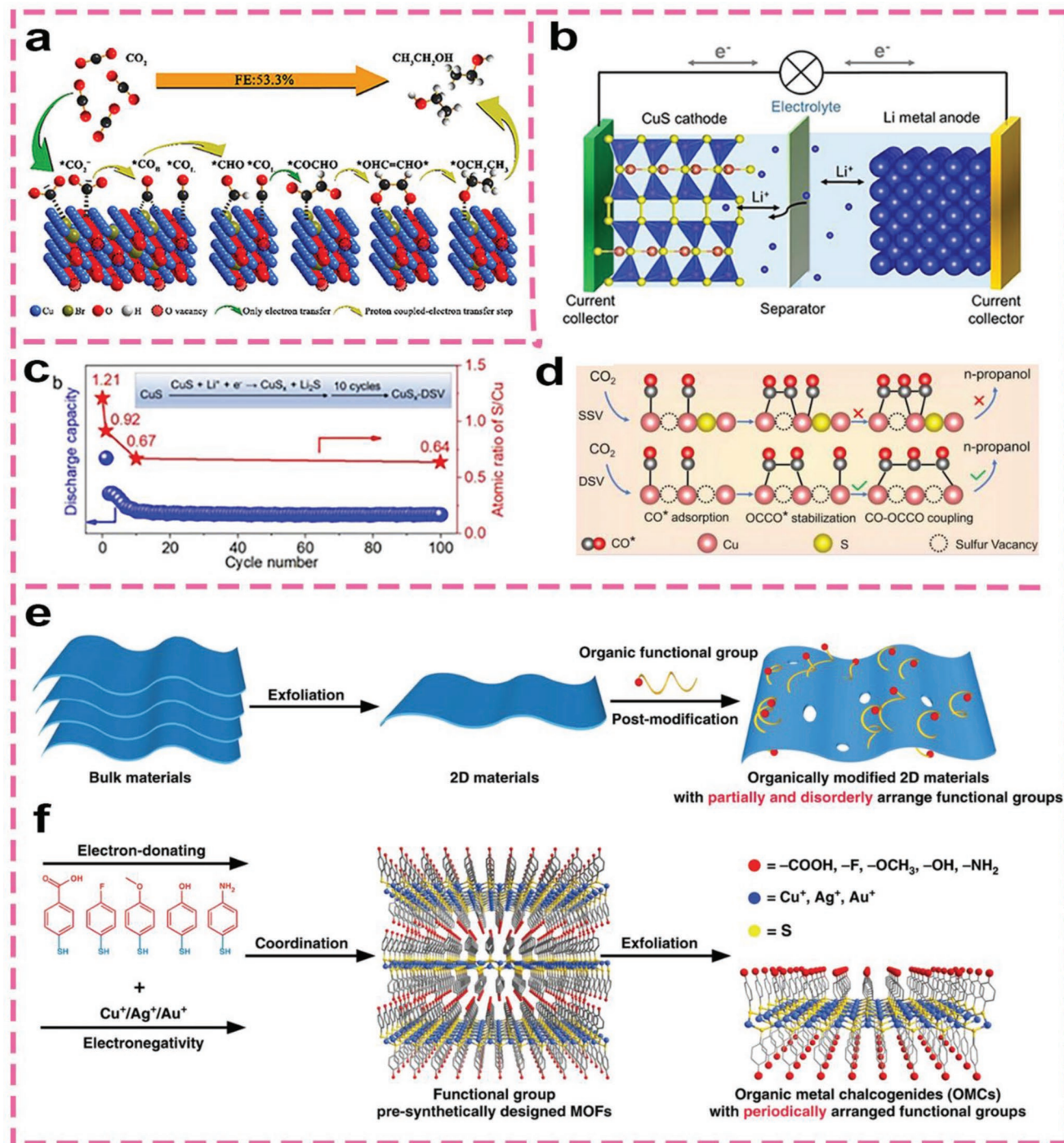


Figure 10. a) Catalytic mechanism diagram of Br-Doped CuO multilamellar mesoporous nanosheets for CO₂ER to ethanol. b) Schematic diagram of lithium-ion battery assembled with CuS (cathode) and Li metal (anode). c) Discharge capacity of CuS (blue dots) and the atomic ratio of S/Cu (red stars) with respect to the cycle number at a constant current of 0.044 mA cm⁻² in the voltage range of 0.01–3 V. d) Mechanism of n-propanol formation on adjacent Cu_x-DSV, showing the dimerization of CO–CO followed by CO–OCCO coupling and then exfoliation (M–E) strategy for organic metal chalcogenides. e) Organic modification (E–M) strategy for the known 2D materials. a) Reproduced with permission.^[97] Copyright 2021, American Chemical Society. b–d) Reproduced with permission.^[106] Copyright 2021, Springer Nature. e, f) Reproduced with permission.^[137] Copyright 2021, Springer Nature.

alters the adjacent local coordination and electron energy level without changing the inherent lattice periodicity.^[102] Liang's group showed that the in situ formation of abundant OVs led

to the increase of rich unsaturated metal sites, greatly enhanced the covalency of Cu 3d–O 2p linkage, increased the d-band center, ensured the optimal adsorption of CuO on oxygen-

containing intermediates, and was conducive to the catalytic reaction.^[103] S vacancies in copper-based materials are another lattice defect,^[104] which can be produced by high-temperature annealing and wet chemical reduction, and dispersed within a finite hierarchical structure.^[105] For instance, hexagonal CuS nanocrystals with a nanoflower morphology have been synthesized by hydrolysis at low temperatures, and S vacancy-rich CuS_x through an electrochemical lithium tuning method (Figure 10b), because of the partial conversion reaction,^[106] where the density of S vacancies was largely affected by the number of charge/discharge cycles (Figure 10c). Density functional theory (DFT) calculations revealed that some new electronic states were created. When double sulfur vacancies were generated on CuS, they could be used as active electrocatalytic sites to stabilize the dimer of CO* and OCCO* and promote the coupling of CO–OCCO to form n-propanol (Figure 10d), resulting in excellent selectivity and high partial current density towards CO₂RR. There are also studies on vacancy in SCs. For instance, Kang et al. demonstrated that F-doped CuCo₂S₄ with S vacancies exhibited intensified pseudo-capacitive properties due to the improved inherent electrical conductivity and the enhanced electrochemical reaction kinetics.^[107] Taken together, OVs and S vacancies can be used to regulate the adsorption energy of reaction intermediates, and to optimize ion diffusion paths, which renders the vacancy a catalytic active site.^[108] Metal vacancies in these structures can be used to regulate the intrinsic activity of the catalytic active sites.^[109] For SCs, for example, OVs can effectively change the donor density of metal oxides, subtly induce impurity states in the bandgap, accelerate the surface redox reaction kinetics, and thus improve the capacitance of metal oxides.^[110] For rechargeable batteries, the introduction of vacancies in ultrathin 2D nanomaterial-based electrodes can be used to control ion diffusion kinetics, electron and ion transport, and the adsorption of active intermediates, all of which can lead to an improved performance.^[111] For catalytic reactions, the generation of vacancies can activate new catalytic sites and/or promote the exposure of active sites. The formation of holes can improve the degree of electron delocalization by narrowing the bandgap or creating new hole states, thus improving the conductivity. The increase of conductivity is due to the change of electronic structure and the acceleration of charge separation and transfer process, which leads to rapid kinetics of the electrocatalytic reaction. Vacancies in electrocatalysts have been widely proven to effectively reduce the adsorption free energy of oxygen evolution reaction (OER) and hydrogen evolution reaction (HER) intermediates, thus providing a more favorable kinetic energy barrier for catalytic reactions.^[112]

Rational design of dislocation can significantly reduce the diffusion path length and polarization of metal ions (e.g., Li⁺) during charge and discharge, while maintaining a high exposed surface and improving electronic conductivity.^[101] By adjusting the annealing temperature, CuO nanosheets with controllable defect contents and crystallinity can be obtained.^[113] In the reconstructed models of the defect-rich structure, the reduction of dislocations caused by high crystallinity could be revealed. Designing nanostructures with more edge sites has been proved to be one of the most effective strategies to improve charge storage dynamics and catalytic efficiency, as

the rich defects lead to crystal cracking, thereby increasing the accessible surface area.^[114] The interface of electrode materials can show rich edge defects.^[115] Xu et al. reported that edge-rich structures increased active sites in the external surface, and promoted the capacitive contribution to fast redox reactions.^[116] Even at low surface areas, the obtained materials exhibited excellent ultrastable and high-rate performance. Both edge-rich defects and heteroatom-doped defects are thought to redistribute the local electron density and provide strong affinity for intermediates.^[117] More active edges and nanoscale holes can be formed on Cu₂MoS₄ nanosheets by chemically etching with diluted nitric acid as the etchant.^[118] The catalytic active sites of Cu₂MoS₄ nanosheets are related to their edges, but not to the basal planes. The obtained Cu₂MoS₄ has indented edges and good hydrophilicity, which can reduce the adsorption potential barrier of H₂O molecules and further enhance its catalytic activity for HER.

4.2. Heterostructures

Due to the synergistic effect of multiple interfaces, formation of 2D heterostructures can lead to the design of new copper-based materials and improve the electrochemical performance.^[119] In fact, the optimization of electron configurations can be realized by electron transfer at heterostructure interfaces.^[120,121] For instance, NiO/CuO nanosheet heterostructures with rich defects and interfaces have been synthesized by electrochemical oxidation, which improved the adsorption energy of the active sites to intermediate species and promoted electrochemical reaction kinetics.^[122] In fact, heterostructures constructed in the form of core–shell structures have attracted wide interest because they can promote ion transport and buffer the volume change during charge–discharge.^[123] In principle, the inner “core” materials with high conductivity can ensure a stable and effective electron transport path, while the outer “shell” materials with a large accessible surface area can provide abundant electroactive sites.^[124] By integrating the advantages of “core” and “shell,” various core–shell heterostructures with different structures show an impressive electrochemical performance. For instance, Wang et al. fabricated novel hierarchical Co₃O₄/CuO heterostructure arrays.^[125] Interestingly, interconnected Ni(OH)₂ nanosheets were controllably deposited on the outer surfaces of the CuCo₂O₄ nanosheets to form a tough hierarchical core–shell structure with abundant defects and a large specific surface area, showing a superb performance with a specific capacitance of 2160 F g^{−1} at 1 A g^{−1}.^[126] Furthermore, Liu et al. first developed 2D CuO-phosphomolybdic acid-Ag sub-1 nm nanosheet heterostructures (CuO-PMA-Ag THSNHs) by employing the “cluster-nuclei co-assembly strategy.”^[127] It is revealed that the synergetic effect of the multicomponents and unique sub-1 nm nanoscale heterostructures profoundly affected the total potential energy, and improved their catalytic activity for the epoxidation of alkenes. Indeed, heterostructures have been widely used in energy storage and conversion, and the interactions between the multiple components are very important. How to give full play to the best characteristics of each component and reduce its shortcomings has remained a big challenge.

Combining copper-based materials with conductive carbon or metal supports can not only improve the conductivity of the hybrid electrode, but also absorb the stress in the electrochemical reactions.^[128,129] CuCo₂S₄ decorated with carbon nanotubes has been known to exhibit a significantly improved specific capacitance in alkaline media.^[130] Carbon materials doped with heteroatoms can also be adopted as catalyst supports.^[131] Based on experimental results, Li and co-workers concluded that CuS nanoplatelets on the surface of graphene could act as spacers and not only prevent the aggregation of CuS nanoplatelets but also prevent the restacking of graphene.^[132] Hierarchical nanostructures can optimize the direct interfacial contact between transition metal atoms and graphene, maintain a large number of electroactive sites, and shorten the ion transport path, leading to a high specific capacitance and ideal rate performance.

4.3. Surface Functionalization

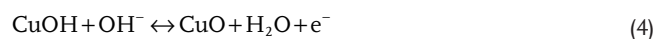
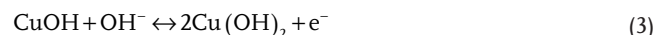
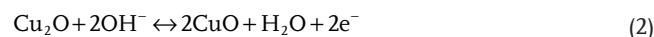
Surface functionalization is another meaningful method of structural engineering by grafting molecules or functional groups onto the materials surface.^[133] This can lead to significant changes in electronic structure and conveniently change their physical and/or chemical properties.^[134] Compared with the harsh conditions of defect engineering and heterostructure design, the process of molecular functionalization is relatively mild.^[135] According to the type of 2D material and molecule, the functionalization can be divided into covalent interactions and noncovalent interactions (e.g., hydrogen bonding, electrostatic interaction, Vander Waals force, coordination bond, and π - π stacking interaction).^[136] For 2D materials, such surface functionalization can have important influence on their catalytic, electrical and optical properties, but little progress has been made in structural regulation.^[41] Recently, Li et al. synthesized organically functionalized layered copper sulfide nanosheets with an adjustable bandgap through a metal-organic framework oriented organic modification and exfoliation strategy.^[137] This is in sharp contrast to the traditional modification strategy which not only limits the modulation range of the bandgap, but also results in an uneven distribution of the organic functional groups on the materials surface (Figure 10e,f). Liu et al. synthesized a new ultrathin copper sulfur monolayer with a thickness of 0.18 nm.^[138] Such organic functionalization may also be exploited for the control of the wetting property of the electrode materials.^[139] In the water cracking reaction, excess H₂ and O₂ bubbles are rapidly produced at high current density. When bubbles adhere to the electrode surface, the active area of the catalyst will decrease, electron transfer will be blocked, and the decomposition rate of water will slow down.^[140] For the oxygen reduction reaction (ORR), the design of micro- and nanostructured electrodes provides a new strategy for accelerating electron transfer and gas diffusion;^[141] For OER and HER, the design of a superhydrophilic surface that is superhydrophobic underwater can facilitate the rapid release of gas bubbles.^[142] In a recent study, a CuS/Cu foam was found to exhibit a superhydrophilic that was superaerophobic underwater, due to the formation of a micro- and nano-structure, which greatly facilitated the mass transfer.^[143]

5. 2D Copper-Based Materials for Supercapacitors

SCs, also known as electrochemical capacitors, is a new generation of energy storage device, which exhibit the characteristics of a high power density (>10 kW kg⁻¹), fast charge and discharge speed (within seconds), good cycle stability (>100 000 cycles), wide operating temperature range, long lifespan, and good safety. SCs possess the characteristics of both electrostatic capacitors and rechargeable batteries, and have attracted extensive attention.^[144] As shown in **Figure 11**, according to the charge storage mechanism, SCs can be divided into two categories: electrochemical double-layer capacitors (EDLCs) and pseudocapacitors (PCs).^[145] The former is based on reversible electrolyte ion adsorption/desorption at the electrode/electrolyte interface, while the latter is based on redox reactions of the electrode materials.^[146] EDLC and PC electrode materials can also be used to construct hybrid capacitors. Because of its excellent performance, SCs have been considered as a viable device for balancing power density and energy density, and can be used in hybrid electrical vehicles, portable electronic equipment, industrial power supply, etc.^[147] The performance of SCs is closely related to the electrode. According to $E = \frac{1}{2}CV^2$, the energy density (E) depends on the capacitance (C) and operating potential window (V). Therefore, the key strategy to improve capacitance performance is to use electroactive electrode materials with a high specific surface area and redox-active media.^[148] The key advantages of 2D materials for potential electrode fabrication include a large surface area that facilitates exposure of surface atoms, high morphological anisotropy and mechanical strength, accessible electrolyte ion channels due to open van der Waals gaps, and abundant electrochemical reaction sites originating from the edge.^[149] Indeed, 2D copper-based materials, such as Cu-O, Cu-S, Cu-Se, and Cu-MOF, have attracted significant attention.

5.1. Mechanistic Insights

When CuO is used as electrode materials in alkaline electrolytes, the relevant redox reactions may involve the transition between the Cu(I) and Cu(II) species:^[150,151]



Two parallel mechanisms/models of charge storage in neutral electrolytes have been proposed. The first mechanism is the intercalation and deintercalation of the smaller H⁺ and larger alkali metal cations into the matrix, that is, oxidation/reduction of the electrode, while the other is the adsorption of ions on the surface rather than in the bulk of the material, which can be expressed as (where A can be either an H⁺ or Na⁺):^[152]

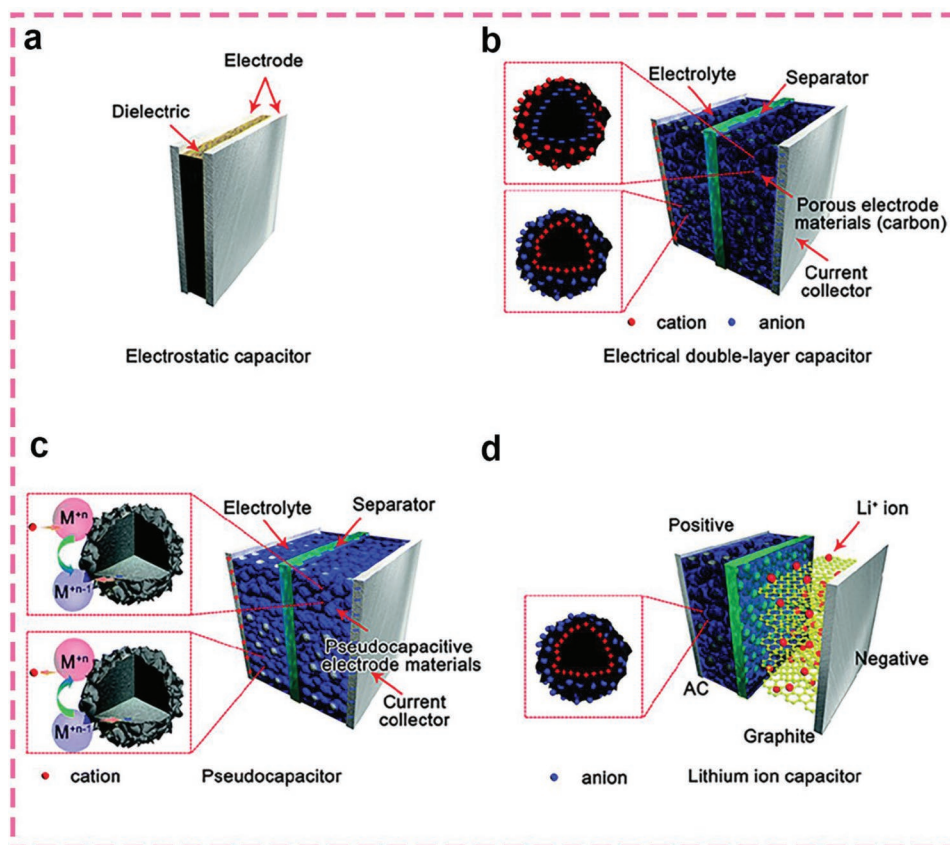
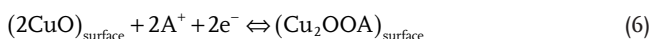


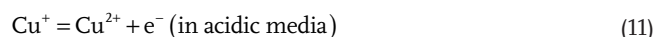
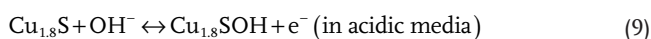
Figure 11. a) Schematic diagram of an electrostatic capacitor. b) An electric double-layer capacitor. c) A pseudocapacitor. d) A hybrid-capacitor. Reproduced with permission.^[145] Copyright 2015, The Royal Society of Chemistry.



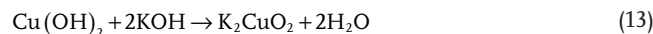
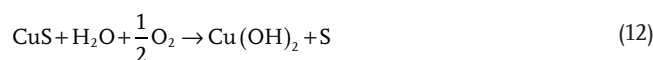
An et al. prepared a nanoporous Cu@Cu₂O hybrid array by a simple electrochemical corrosion method, and the charging mechanism in SCs with and without light is shown in **Figure 12a**.^[153] The charge storage mechanism of intercalating pseudocapacitive in Cu–S is quite conspicuous.^[42,154] The pseudocapacitance of the electrode produced by the interaction/extraction of Li⁺ within the thin film electrodes will be affected by the crystallinity of the heat-treated samples. In this reaction, Li⁺ interacts with CuS to occupy vacancies in the lattice and form the Li_xCuS complex. Finally, the Li_xCuS reacts with S to form Li₂S and CuS, and the product CuS promotes the cyclic reaction of the electrode,^[155] as shown below in Equations (7) and (8),



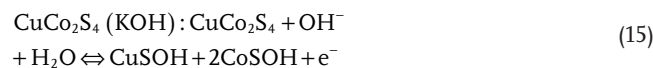
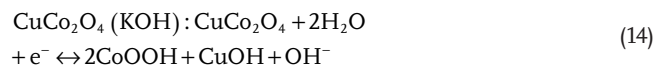
The possible reversible faraday transformations of Cu–S in aqueous media at different pH are shown in the following chemical equations:



After the conversion of CuS to the hydroxide phase, the following pseudocapacitance redox processes can occur:^[156]



Other materials can undergo electrochemical reactions in different electrolytes,^[157,158]



Therefore, to better understand the electrochemical charge storage behavior in copper-based materials, the composition and properties of the electrolyte used should be carefully examined.

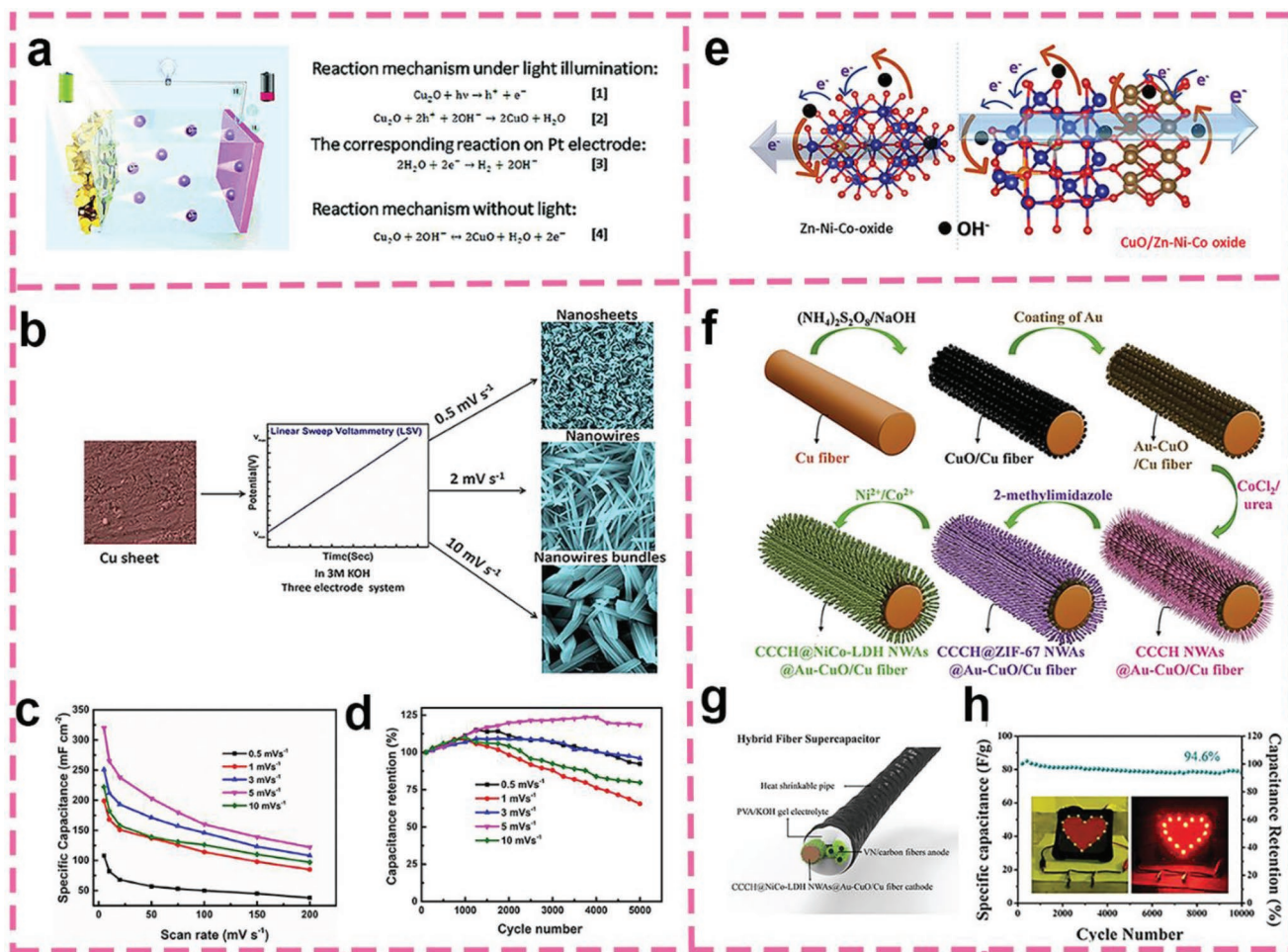


Figure 12. a) Schematic representation and the charging mechanism of the electrode reactions in supercapacitor with/without light illumination. b) Schematic showing the formation of different copper oxides nanostructures at different scan rates during the LSV process. c) Specific capacitance of copper oxides nanostructures calculated from charge–discharge cycles at different current densities. d) Cyclic stability calculated at a current density of 15 mA cm⁻². e) Schematic illustration of the mechanism involved in Zn-Ni-Co oxide and CuO/Zn-Ni-Co oxide. Blue, red, orange, gray, brown, and black balls represent Co, O, Ni, Zn, Cu, and OH⁻ (from electrolyte), respectively. f) Schematic illustration of the synthesis of CCCH@NiCo-LDH NWAs@Au-CuO/Cu fibers. g) Schematic diagram of the assembly of solid-state flexible device. h) Long-term cycling performance of the HFSC device and three serially connected HFSCs for powering LED. a) Reproduced with permission,^[153] Copyright 2019, The Royal Society of Chemistry. b–d) Reproduced with permission,^[161] Copyright 2020, Elsevier. e) Reproduced with permission,^[167] Copyright 2020, Elsevier. f–h) Reproduced with permission,^[172] Copyright 2019, Wiley-VCH.

5.2. Applications

5.2.1. Cu–O

CuO nanosheets have been found to show a maximum specific capacitance of 569 F g⁻¹ at 5 mA cm⁻²,^[159] whereas the performance of bulk CuO is limited because of low electrical conductivity and unstable cycling ability. To improve the reversible charge/discharge performance, Lu et al. developed an in situ anodization process to prepare novel graphene-like CuO nanofilms on a Cu foam consisting of interconnected ultrathin crystalline nanosheets.^[151] As an electrode material, the CuO nanofilms exhibited a specific capacitance of 919 F g⁻¹ and excellent stability, with 93% capacitance retention after 5000 cycles. The same strategy can be used to synthesize CuO of different morphologies, where the surface area is found to correlate with

the electrochemical performance.^[160] More recently, Parida et al. adopted a single-step linear sweep voltammetry technique to synthesize multiple-phase nanostructured copper oxide nanosheets and nanowires of CuO–Cu₂O–Cu(OH)₂ by changing the voltage sweep rate (Figure 12b).^[161] Electrochemical tests showed the relationship between the specific capacitance of all samples and the scanning rate (Figure 12c). At the scan rate of 5 mV s⁻¹, the electrode showed outstanding cycle stability and specific capacity of 320 mA cm⁻² (Figure 12d).

Another effective strategy is to design and prepare functional CuO composites, such that electron transport is accelerated by reducing the charge-transfer resistance. Carbon-based materials (e.g., graphene, nanoporous carbon, carbon-nanotubes (CNTs), etc.) have been explored as electrode materials, because of rapid electron transfer, high mechanical strength, good elasticity, and large surface area. Therefore, they are often blended with

CuO to prepare hybrid composites for energy storage,^[162–164] which helps improve the charge/discharge cycle stability and storage capacity of the nanostructured composites.^[165] Ghosh and co-workers synthesized nanocomposite with a stacked layered structure in which CuO nanosheets were deposited onto rGO.^[166] In comparison to the pristine 2D CuO electrode that retained 72% of the specific capacitance after 5000 cycles, 2D CuO/rGO electrode showed 81% capacitance retention. It is believed that the rGO highly improved the mechanical stability and electrical conductivity of the nanocomposites, and concurrently, the transport of electrolytic ions was enhanced. In addition, the introduction of various metal structures with high conductivity and large specific surface area can further improve the performance of the electrode. Hussain et al. developed nanoporous high-performance hybrid SCs, which achieved an energy density of 74 Wh kg⁻¹ at a power density of 1.02 kW kg⁻¹.^[167] For CuO/Zn-Ni-Co oxide nanocomposites on nickel foam, 2D CuO nanosheets were embedded between the nanowires, which provided elaborate transport pathways for electrons leading to an improved electrochemical performance. The action mechanism is described in Figure 12e, which shows that the addition of 2D CuO not only provides a stable structure for the integrated nanocomposite, but also increases the surface area and capacity.

Metal doping is another effective route toward controlling the performance of bulk semiconductors.^[168] For example, Shaikh and co-workers prepared Ru-doped CuO films and found that Ru doping simultaneously increased the power density and specific capacitance.^[169] Huang et al. reported that Ag-doped CuO nanosheets exhibited a lower polarization and higher electrochemical activity.^[170] Similarly, Lv et al. synthesized Mo-doped CuO composites with a specific capacitance of 1292 F g⁻¹ at 2 A g⁻¹.^[171] Multicomponent hierarchical nanostructures can be formed by combining CuO with highly conductive materials and metal doping, with a large accessible surface area, leading to significantly improved ion diffusion, reaction kinetics, and excellent supercapacitor performance. As shown schematically in Figure 12f, a multicomponent layered structure of Cu-doped CCCH@NiCo-LDH NWAs@Au-CuO/Cu (Cu-doped cobalt copper carbonate hydroxide@nickel cobalt layered double hydroxide) was synthesized by a simple in situ corrosion growth method.^[172] The unique structure afforded specific capacitances of 1237 F g⁻¹ with a retention rate of 79.2% with the current increased by a factor of 15. Additionally, they assembled a hybrid SC with CCCH@NiCo-LDH NWAs@Au-CuO/Cu wire and VN/CFs as the cathode and anode materials, respectively, to further analyze the practical application of the electrode (Figure 12g). After 10 000 cycles, 94.8% of the capacitance was retained (Figure 12h). In addition, the electrode exhibited a good energy storage performance with a power density of 1.41 kW kg⁻¹ at an energy density of 34.97 Wh kg⁻¹.

In summary, there are three leading strategies to improve the electrochemical performance of CuO, the synthesis of novel structures, formation of CuO hybrid materials, and metal doping.

Cu₂O is another ideal energy storage material with a higher theoretical capacitance than CuO.^[173] However, nanostructured Cu₂O materials have poor cyclic stability and conductivity. Nanostructured materials can be directly grown on the current

collector to form a binder-free electrode, producing a satisfactory capacitance on the total weight of the electrode.^[174] At present, Cu₂O and composites are mainly grown on Cu foams and foils. Liu et al. demonstrated a high performance of Ni(OH)₂/Cu₂O nanosheets, in a three-electrode system, which delivered a maximum specific capacitance of about 8234 mC cm⁻² at 20 mA cm⁻² and exhibited no decay after 10 000 cycles.^[175] Du et al. prepared hybrid Cu₂O/CuMoO₄ nanosheets on Ni foam, which possessed a maximum specific capacitance of 4264 F g⁻¹ at 1 A g⁻¹ and a mere initial capacitance loss of 13.4% even after 3000 charge/discharge cycles.^[176] Leaf-like CuO–Cu₂O nanocomposites were prepared via a one-step anodization method on copper foam and exhibited a relatively high specific capacity (1954 F cm⁻² at 2 mV s⁻¹) and remarkable durability (120% retention after 5000 cycles).^[177] Xu et al. successfully synthesized Cu₂O/CuO nanosheets by in situ growth on Cu-carbon cloth, and an asymmetric capacitor was constructed by using it as the positive electrode and activated carbon as the negative electrode, which exhibited a maximum energy density of 60.26 Wh kg⁻¹ with a power density of 299.73 W kg⁻¹ at an extended voltage of 1.8 V. Furthermore, it demonstrated excellent cycling stability with 90.35% capacitance retention after over 5000 cycles.^[178]

Cu(OH)₂, another 2D copper material, has been gradually attracting interest because of its unique morphology, excellent chemical stability and structure-dependent electrochemical properties.^[179] For example, Bulakhe et al. prepared Cu(OH)₂ of different morphologies by controlling the type of copper salts through the SILAR method and studied the supercapacitive performance.^[180] During the electrochemical process, the flower-like Cu(OH)₂ exhibited a high surface area and 3D interconnected conducting petal framework, resulting in higher reactivity and ion transport than other structures for EDLCs. In addition, LDHs accelerated the intercalation/deintercalation of charged ions due to the large interlayer spacing.^[181] Therefore, with the formation of binary hydroxide composites, the electrochemical performance of Cu(OH)₂ can be improved, while retaining the excellent durability and flexibility.^[182]

Owing to the similar lattice constants of Cu²⁺ and Ni²⁺ LDHs, the composition of NiCu-LDH can be easily adjusted by partially replacing lattice Ni²⁺ with Cu²⁺. The addition of Cu²⁺ is not only conducive to the electrochemical activity, but also improve the conductivity.^[183] Wang's group prepared NiCu-LDH nanosheet arrays and investigated the effect of Ni/Cu precursor ratios on the electrochemical performance.^[184] The optimum sample at the precursor ratio of Ni/Cu = 0.7 showed the highest specific capacitance of 1953.5 F g⁻¹ at 0.5 A g⁻¹ and capacitance retention rate. However, the cyclic stability of all samples was not ideal. In another work, Huang and co-workers demonstrated that the decoration of NiCu-LDH nanosheets on the surface of NiCo₂S₄ nanotube led to an increased areal capacity (632.0 μAh cm⁻² at 2 mA cm⁻²), corresponding to a volumetric energy density of 2.7 mWh cm⁻³ at a power density of 21.3 mW cm⁻³.^[185]

More recently, the Cu and Co LDH main layers are modified based on their variable oxidation state. The presence of Cu and Co in the LDH materials leads to the formation of CuOOH and CoOOH during the electrochemical process, respectively, which are instrumental in enhancing electron transfer during

the Faradaic reactions.^[186] Kumar et al. synthesized a series of CuCo-LDH nanosheets-based polyhedra by tailoring the Cu/Co ratio in the LDH host layers via hydrothermal synthesis.^[187] The optimum Cu_{1.65}Co₁-LDH sample exhibited a remarkable electrochemical performance, including an ultra-high energy density of 52.86 Wh kg⁻¹ at 2766 W kg⁻¹ and good coulombic efficiency at 4 A g⁻¹ after 10000 cycles (Figure 13a,b). However, up to now, there is still a lack in the knowledge of the influence of copper contents on the supercapacitor performance of LDHs.

CuCo₂O₄ is a spinel cobaltite and can be used as a cathode material of SCs.^[188,189] At present, the synthesis methods of 2D

CuCo₂O₄ nanostructures include hydrothermal, electrodeposition, and eutectic solvent methods. For example, Kim and co-workers synthesized CuCo₂O₄ using a simple hydrothermal method,^[60] which displayed a higher specific surface area and capacitive performance than nanowires, with a capacitance of 244 F g⁻¹ at a 1 A g⁻¹, energy density of 21.5 Wh kg⁻¹, power density of 400 W kg⁻¹, and 91.1% retention of capacitance after 5000 cycles (Figure 13c,d). Wang et al.^[190] prepared CuCo₂O₄/CuO/multiwalled carbon nanotubes (MWCNTs) hybrid nanocomposites, which were composed of many nanosheets with rich mesopores. Notably, doping of MWCNT into the nano-flowers not only formed a conductive network, but also had

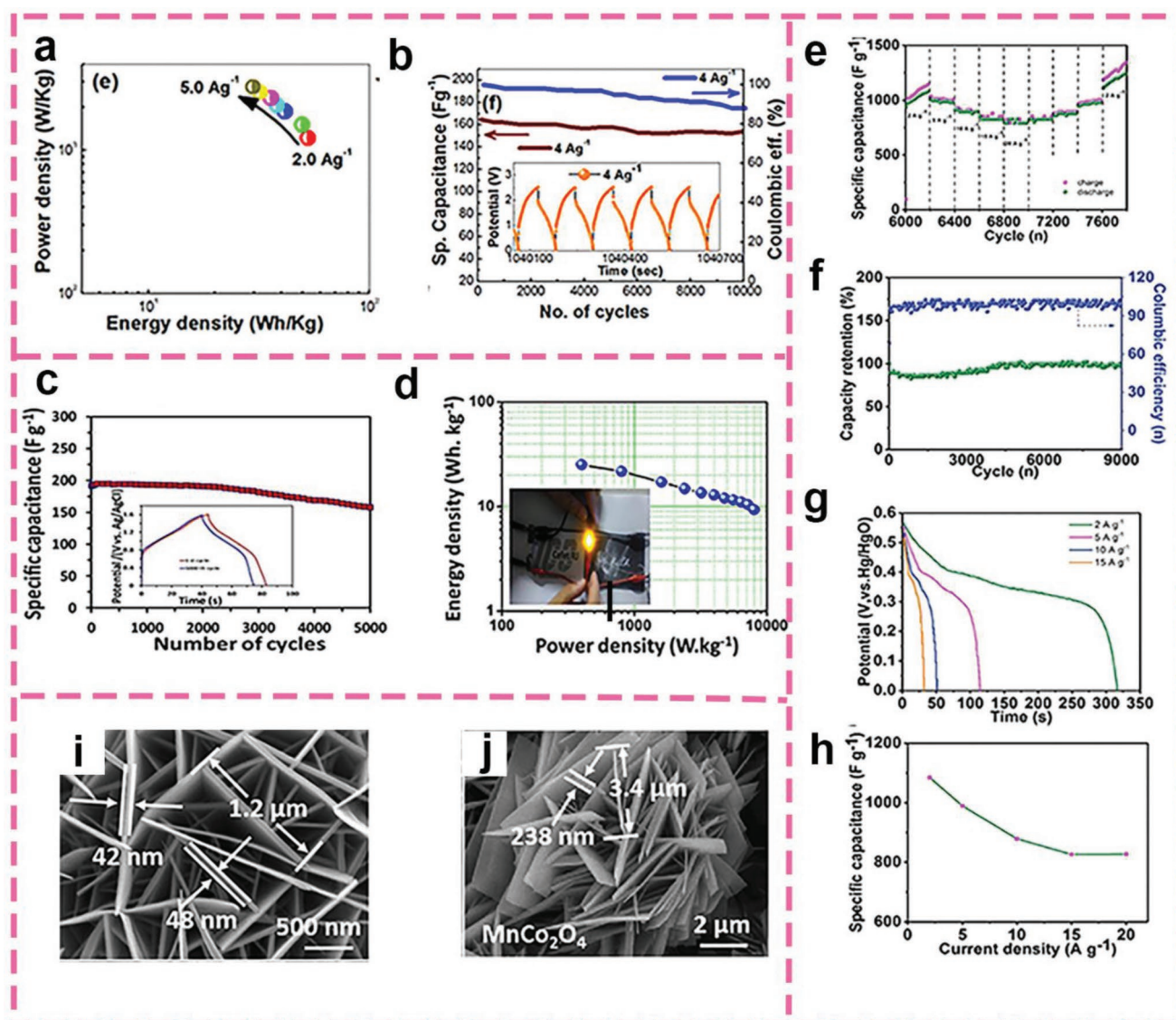


Figure 13. a) Ragone plot of the as-assembled flexible cell. b) Cycling performance of the cell up to 10 000 cycles (inset: few GCD cycles after elongated time at 0° bending). c) Ragone plot of the CCO-NS//HCP-CNF ASC device (inset: photograph of yellow LED powered by two solid-state ASC connected in a series). d) Cyclic performance of the CCO-NS//HCP-CNF ASC device. e) Galvanostatic discharge curves at various current densities of the CCO/CO/MW electrode. f) Specific capacitance. g) Rate performance. h) Cycling performance of the CCO/CO/MW electrode at 10 A g⁻¹. i) FESEM images of CuCo₂O₄ nanosheets. j) CuCo₂O₄/MnCo₂O₄ heterostructures. a,b) Reproduced with permission.^[187] Copyright 2021, American Chemical Society. c,f) Reproduced with permission.^[60] Copyright 2019, Elsevier. e-h) Reproduced with permission.^[190] Copyright 2021, Elsevier. i,j) Reproduced with permission.^[191] Copyright 2019, The Royal Society of Chemistry.

no significant effect on the primitive morphology and structure. The hybrid electrodes were found to deliver a large specific capacitance of 1084 F g^{-1} at 2 A g^{-1} , an excellent rate performance and a capacitance retention of 97.8% after 9000 cycles (Figure 13e–h). CuCo_2O_4 can also be combined with other metal oxides to construct heterostructures, leading to improved specific capacity and cyclic stability. Liu et al. successfully synthesized $\text{CuCo}_2\text{O}_4/\text{MnCo}_2\text{O}_4$ electrodes by employing a two-step hydrothermal method followed by postannealing treatment.^[191] Scanning electron microscopy (SEM) studies (Figure 13i,j) clearly showed that the as-prepared samples consisted of CuCo_2O_4 nanosheets of $1.2 \mu\text{m}$ in length and 45 nm in diameter. In contrast, the double-layer heterostructures displayed an open network structure of MnCo_2O_4 nanosheets perpendicular to the surface of the CuCo_2O_4 nanosheets. The stacked heterostructures exhibited a specific capacity of 1434 F g^{-1} at 0.5 A g^{-1} , an outstanding rate performance with 56.6% capacity retention even at 15 A g^{-1} , and a superior cycling ability with 81.4% capacity retention over 5000 cycles at 10 A g^{-1} . Furthermore, an electrochemical capacitor device with the prepared $\text{CuCo}_2\text{O}_4/\text{MnCo}_2\text{O}_4$ as the positive electrode and graphene as the negative electrode exhibited an energy density of 42.1 Wh kg^{-1} and power density of 400 W kg^{-1} , and excellent capacity retention of about 88.4% for 10 000 cycles. Later on, Chanda et al. prepared heterostructures consisting of 2D nanoforms of CuCo_2O_4 and MnO_2 on flexible carbon fabrics, and the composites exhibited a good performance including a specific capacity of 1458 F g^{-1} at 0.5 A g^{-1} and 93% capacity retention after 5000 cycles.^[192] All these indicate that the rational vertical stacking architectures have great potential as a new design method for next-generation energy storage applications.

2D CuCo_2O_4 materials can also be prepared by other methods. Abbasi and Arvand fabricated CuCo_2O_4 nanosheets through an electrodeposition method, which possessed a specific surface area up to $122.6 \text{ m}^2 \text{ g}^{-1}$ and a thickness less than 20 nm .^[193] The electrode displayed a high specific capacitance of 1330 F g^{-1} at a current density of 2 A g^{-1} and a good rate capability with 50.67% capacitance retention when the current density was increased from 1 to 20 A g^{-1} . Meanwhile, the electrode exhibited a high energy density of 29.55 Wh Kg^{-1} with a power density of 0.4 kW kg^{-1} and had an attractive cycling performance with only 6.4% degradation of capacitance after 5000 cycles. The remarkable performance was attributed to the following reasons: i) the electrodes prepared from nitrate precursors exhibited excellent ion/electron transport; ii) the nanoporous structures provided a large surface area, which effectively promoted electron and ion transport between the electrode and electrolyte; iii) since the space between the interconnected nanosheets acted as an ion buffer, the reduced ion diffusion paths increased the accessibility of ions to the inner surface and the high reactivity of the material; and iv) without the addition of conductive agents and binders, the hierarchical multilayer nanosheet arrays were directly grown on nickel foam, which improved the utilization rate of the active materials and reduced the electrode resistance. In Pawar's work, CuCo_2O_4 nanosheets were prepared in a similar way.^[194] The maximum specific capacitance was 1473 F g^{-1} at 1 A g^{-1} with about 93% capacity retention after 5000 cycles. In another study, CuCo_2O_4 hybrid nanostructures were synthesized by using a deep

eutectic solvent method followed by annealing at $250 \text{ }^\circ\text{C}$, and the specific capacity of the optimal CuCo_2O_4 electrode reached 421 mAh g^{-1} at 10 mA cm^{-2} .^[195]

5.2.2. Cu–S

This section will focus on nanostructured CuS as electrode materials. For example, Huang et al. fabricated CuS with various morphologies, of which the thickness of the CuS was tightly controlled by the surfactants and resulted in different electrochemical performances.^[196] The as-obtained 2D CuS exhibited an impressive specific capacitance of 833.3 F g^{-1} at 1 A g^{-1} . Naveed's team prepared CuS nanosheets, which displayed a mesoporous structure (pore size $<25 \text{ nm}$), large specific surface area (about $169 \text{ m}^2 \text{ g}^{-1}$),^[197] a specific capacitance of 2535 F g^{-1} at 0.5 A g^{-1} and a remarkable rate capability of 87% at 20 A g^{-1} . In addition, the power density of the mixture was 400 Wh kg^{-1} and the energy density was 63.2 kW kg^{-1} . Liu et al. successfully prepared CuS/MnS composites, which afforded a capacitance up to 1144 F g^{-1} at 1 A g^{-1} , and retained 85.9% of the initial capacitance after 10 000 cycles, revealing exceptional long-term cycling stability.^[198] With the help of $\text{Ni}(\text{OH})_2$, the performance of nanostructured CuS electrodes can be further enhanced. For example, for the first time, Reddy et al. prepared 2D CuS nanoflakes-reinforced $\text{Ni}(\text{OH})_2$ nanosheets and observed that the $\text{Ni}(\text{OH})_2@\text{CuS}$ films possessed a high specific capacitance of 640 F g^{-1} at 1 A g^{-1} and 82% capacitance retention after 1000 cycles, as compared to 142 F g^{-1} for $\text{Ni}(\text{OH})_2$.^[199] At the same time, the electrode exhibited a high energy and power density of about 256 Wh kg^{-1} and 92 kW kg^{-1} in the potential range of 0–0.5 V, respectively. In comparison, $\text{CuS}@\text{Ni}(\text{OH})_2$ was prepared via hydrothermal and electrodeposition processes.^[200] Chronoamperometry measurements at -0.9 V, with a time interval of 0, 3, 5, and 7 min, delivered a specific capacitance of 1895, 2055, 3585, and 2900 F g^{-1} at 1 A g^{-1} , respectively. A similar trend was observed in cycling performance, in which the nanostructures (7 minutes) showed better stability than the others in the 4000th cycles.^[201]

Bimetal sulfides, such as CuCo_2S_4 , Cu_3SbS_4 , and Cu_2WS_4 , have also attracted much attention. Bimetallic sulfides possess a lower bandgap than single metallic sulfides, so it has more redox reaction sites and higher conductivity.^[202] These properties are of great significance for improving their electrochemical performance. In a previous study, CuCo_2S_4 nanosheets were directly grown on flexible carbon fiber textile with a high specific capacitance of 3321.6 F g^{-1} at 5 A g^{-1} , retaining a good rate performance and coulombic efficiency after 3000 cycles.^[203] Clearly, the addition of conductive polymers has a huge impact on its electrochemical performance. To our knowledge, the basic properties of graphene and graphene quantum dots (GQD), such as high conductivity, large surface area and easy dispersion, are conducive to ion diffusion and charge transfer kinetics.^[204] Huang's group reported the synthesis of GQD-doped CuCo_2S_4 nanocomposites by employing a two-step hydrothermal method (Figure 14a), and the CuCo_2S_4 and nanocomposites showed a coral thicket-like nanosheet morphology (Figure 14b,c), with a specific capacity of 1725 F g^{-1} at 0.5 A g^{-1} and long cycle life (90% of the initial capacitance after

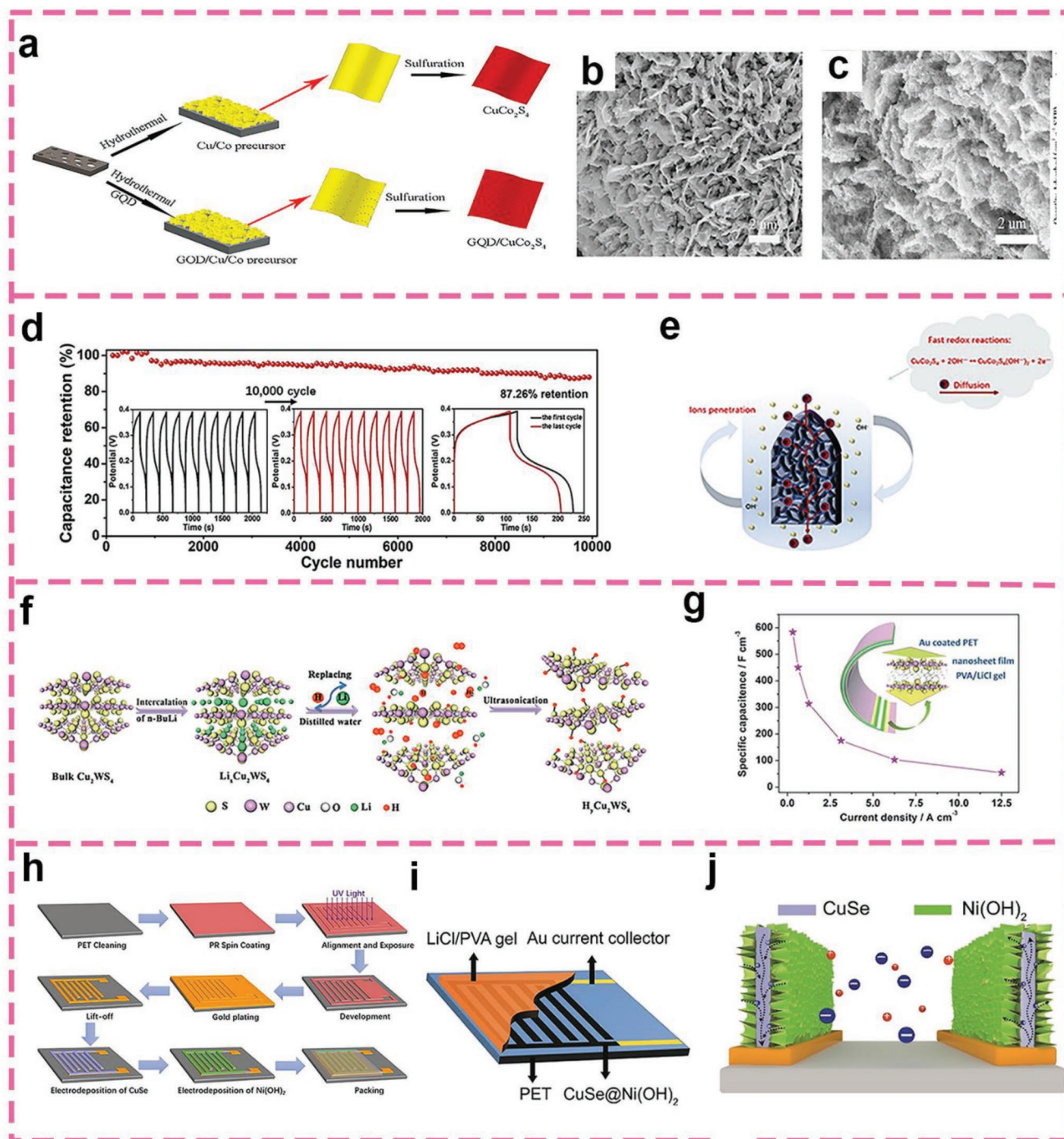


Figure 14. a) Schematic diagrams of the synthesis processes of the CuCo_2S_4 nanosheets and the GQD/ CuCo_2S_4 nanocomposites grown on the Ni foam. b) SEM image of the CuCo_2S_4 nanosheets. c) SEM image of GQD/ CuCo_2S_4 nanocomposites. d) Long-term cycling performance and Coulombic efficiency of the CuCo_2S_4 -55 electrode at a current density of 10 A g^{-1} for 10 000 cycles. The inset of (d) displays the GCD curves of the initial 10 cycles (left) and last 10 cycles (middle) as well as the comparison of the first and last cycles (right). e) Schematic illustration for the mechanism of charging and discharging processes for CuCo_2S_4 -45 electrode. f) Formation of hydrogenated- Cu_2WS_4 nanosheets. g) Specific capacitance versus current density from 0.3 to 12.5 A cm^{-3} . The inset shows a schematic illustration of the structure of the as-fabricated symmetrical supercapacitor. h) Schematic diagram for illustrating the preparation of vertically aligned CuSe@Ni(OH)_2 hybrid nanosheet films on Au interdigital electrodes/PET substrate. i) Schematic illustration for the configuration. j) Ion transport of CuSe@Ni(OH)_2 hybrid nanosheet films-based in-plane MSCs device. a–c) Reproduced with permission.^[205] Copyright 2018, Elsevier. d,e) Reproduced with permission.^[206] Copyright 2020, Elsevier. f,g) Reproduced with permission.^[212] Copyright 2016, Wiley-VCH. h–j) Reproduced with permission.^[218] Copyright 2018, American Chemical Society.

1000 cycles).^[205] Jiang et al.^[206] prepared 2D multilayer CuCo₂S₄/Co-MOF composites, which retained 87.26% of the capacity after 10 000 cycles at 10 A g⁻¹ (Figure 14d). From Figure 14e, the excellent electrochemical performance was possibly ascribed to the good synergistic properties between the ordered porous stable nanostructures and binary metals. Abuali et al.^[207] primarily fabricated CuCo₂S₄/polyaniline by hydrothermal and chemical polymerization. Polyaniline depolarized the electrode/electrolyte interface, so as to enhance the penetration of electrolyte into the electroactive materials and hence ionic diffusion in the process of charge and discharge. Interestingly, the newly prepared electrode delivered a high energy density (32.5 Wh kg⁻¹), good power density (900 W kg⁻¹) and extended operating potential window (1.8 V).

Other bimetallic sulfides have also been widely used in solar cells because of their direct bandgap and high absorption coefficient in the visible region, but their unique storage capacity is rarely studied in energy storage applications.^[208] In 2015, Ramasamy et al. reported the energy storage properties of CuSbS₂ materials, where they demonstrated the use of CuSbS₂ nanoplates of 55 ± 6.5 nm in thickness as potential electrodes with excellent capacitance,^[209] and studied the specific capacitance and long-term cycling behaviors in different electrolytes, namely LiOH, NaOH and KOH. Mariappan et al. reported the synthesis of Cu₃SbS₄ nanoplates and used the layered Cu₃SbS₄ as an electrode with a specific capacitance of 60 F g⁻¹.^[210] In order to optimize the intrinsic conductivity,^[211] Chen et al. showed for the first time that partially hydrogenated-Cu₂WS₄ nanosheets exhibited a series of transitions from semiconductors to semimetals and then to metals in the electronic structure (Figure 14f), accompanied by a high improvement in conductivity,^[212] with a superb capacitance of 583.3 F cm⁻³ at 1 A g⁻¹ (Figure 14g) and a capacitance retention of about 95% over 3000 cycles. Pazhamalai's group reported the synthesis of binder-free copper tungsten sulfide anchored on Ni foam by employing a hydrothermal route,^[213] which showed a high specific capacitance of 10793 F g⁻¹, a high energy density of 48.57 Wh kg⁻¹, about 92.1% retention of the initial capacity after 10 000 charge–discharge cycles.

5.2.3. Cu–Se

As new battery electrode materials, the Cu–Se compounds have attracted interest in recent years.^[214] Compared with metal oxides and metal sulfides, metal selenides have a lower energy band and higher conductivity, which makes them better candidates as SC electrodes.^[215] However, the aggregation of individual CuSe nanosheets lowers the energy density and reduces the mechanical strength of the CuSe-based electrode.^[216,217] At present, hydrothermal and electrodeposition methods have become the most effective methods for the preparation of 2D CuSe nanomaterials. Using simple electrodeposition (Figure 14h), Gong et al. fabricated CuSe@Ni(OH)₂ hybrid nanosheet films and directly used them to construct flexible in-plane microsupercapacitors (MSCs) by choosing a polyvinyl alcohol-LiCl gel as both the separator and the solid electrolyte (Figure 14i).^[218] As presented in Figure 14j, the high capacitive contribution was attributed to the unique hierarchical open

channels of the hybrid films, the increased and easily accessible electroactive sites, the reduced restacking of electrode materials, and the enhanced electron transfer during charge–discharge process. It displayed a volumetric specific capacitance as high as 38.9 F cm⁻³ at 0.05 mA cm⁻², with an energy density and maximum power density of 5.4 mW h cm⁻³ and 833.2 mW cm⁻³, respectively. Similarly, Li et al. constructed 2D self-supported CuSe@PANI, CuSe@Ni(OH)₂, and CuSe@FeOOH core/shell nanosheet frameworks, which possessed a better electrochemical performance than the corresponding individual component.^[219,220] Due to the good conductivity, multiple oxidation states and high stability of NiSe, Wang et al. prepared a unique heterostructure composed of CuSe and NiSe by one-step hydrothermal method, which showed 2D vertically aligned nanosheets with the average thickness of 27 nm. When an all-solid-state flexible SC was constructed by choosing PVA/KOH as both the separator and the solid-state electrolyte, a large capacitance of 333 F g⁻¹ was achieved at a current density of 1 A g⁻¹, and excellent energy density of 18.65 Wh Kg⁻¹ at power density of 285 W kg⁻¹.^[221]

5.2.4. Cu-MOF

In recent years, with the advantages of hierarchic constructions of redox-active metal centers, large specific surface areas, flexible channels, and various adjustable morphologies, MOFs and related materials have become viable electrode materials for SCs.^[222–224] MOFs are infinite networks composed of metal centers or inorganic clusters crosslinked by appropriate organic ligands through coordination bonds. Organic linkers usually consist of functional groups, such as pyridyl and cyano, crown ether, polyamine, phosphonate and carboxylate, and the metal centers are usually transition metal ions and lanthanide ions.^[225] However, limited by the low conductivity, 2D Cu-MOFs are often designed as composites of MOF and other conductive materials, or transformed into their derivatives. For instance, Xu and co-workers successfully prepared an ultrathin Cu-MOF in combination with δ-MnO₂ nanosheets.^[226] The composite showed a high specific capacitance of 340 g⁻¹ at 1 A g⁻¹ and retained 95% of the original capacitance after 6000 cycles. In addition, Bai's group synthesized 1D-2D Cu-TCPP nanofilm/CNT and 2D-2D Cu-TCPP nanosheet/GO composites (TCPP = Tetrakis (4-carboxyphenyl) porphyrin) in the presence of PVP (Figure 15a).^[227] The morphology and size of the Cu-TCPP nanofilm/CNT nanocomposites wrapped with CNTs were similar to that of Cu-TCPP nanofilms (Figure 15b,c). It is evident that the electrochemical activity of the composite was much better than that of the original Cu-TCPP nanofilms and CNT. In addition, 2D-2D Cu-TCPP nanosheet/GO composite delivered a specific capacitance of 831.7 and 350 F g⁻¹ at 1 and 20 A g⁻¹, respectively. Similarly, Deng's group synthesized a new 2D-2D MOFs nanocomposite Ni//Cu-MOF by integrating Cu₃(HITP)₂ and Ni-MOF-24 with specific functions into a homogeneous layered MOF array (Figure 15d).^[228] SEM studies (Figure 15e) confirmed that the Ni//Cu MOF array was successfully synthesized on carbon fiber paper with Co(OH)₂ as the template and precursor, which was further confirmed in transmission electron microscopy (TEM) and EDS measurements

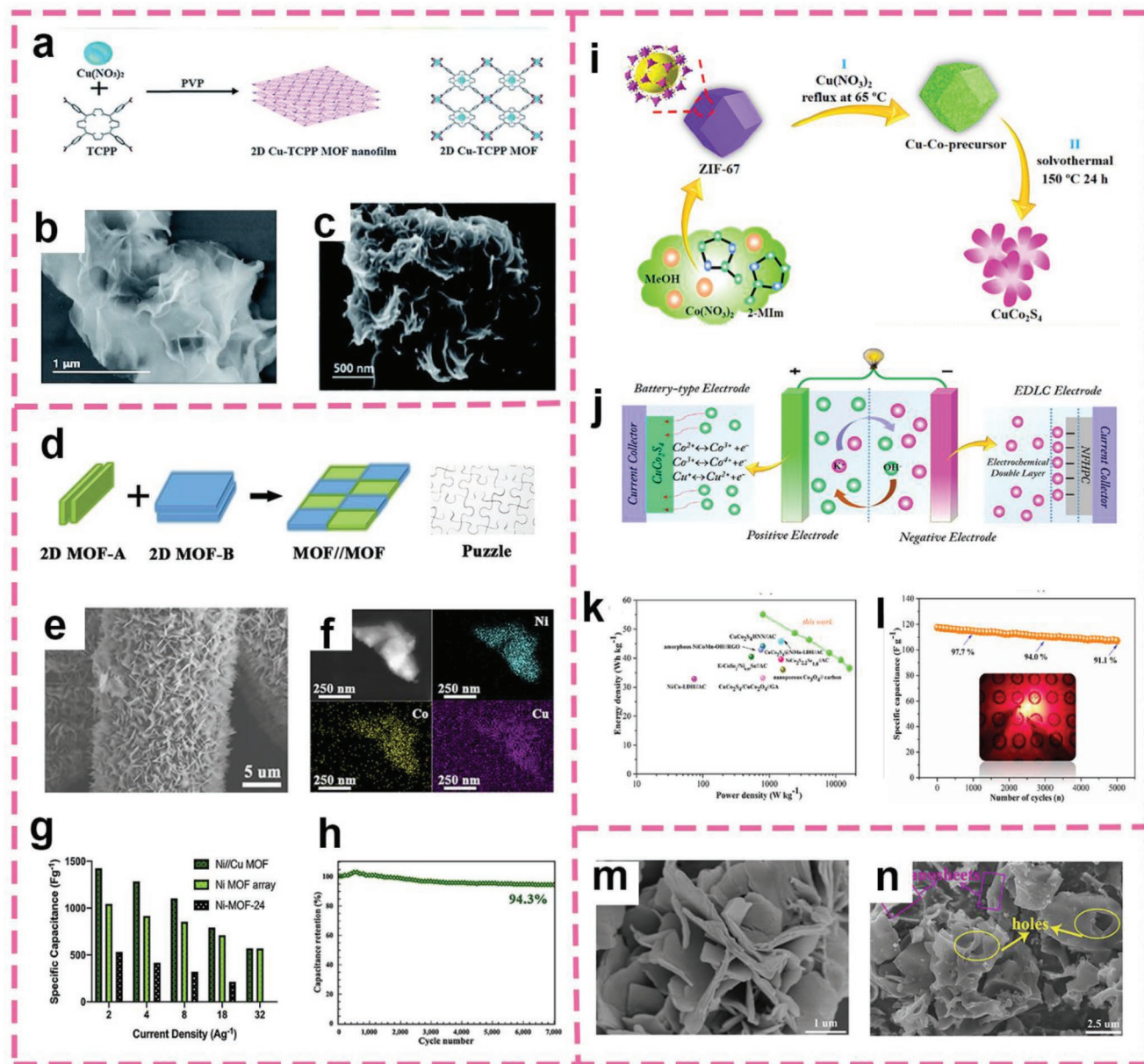


Figure 15. a) Crystal structure of Cu-TCPP nanofilm and schematic illustration of the synthesis of the 2D Cu-TCPP nanofilm. b) SEM images of 2D Cu-TCPP nanofilm. c) Cu-TCPP nanofilm/CNT. d) MOF//MOF synthesis illustration. e) SEM image of Ni//Cu MOF array on CF. f) STEM image and EDS elemental mapping of Ni//Cu MOF. g) The capacitance comparison of Ni//Cu MOF, Ni MOF array, and powder Ni-MOF-24 at all current densities. h) The stability test of the capacitor. i) Synthetic diagram of CuCo_2S_4 . j) Schematic illustration of CuCo_2S_4 //NFHPC asymmetric supercapacitor device. k) Ragone plot of CuCo_2S_4 //NFHPC. l) Cycling performance of CuCo_2S_4 //NFHPC at a current density of 10 A g^{-1} . The inset of (l) is a photograph of a red LED lighting up by two series devices. m) FESEM images of Cu-MOF. n) Activated porous carbon. a–c) Reproduced with permission.^[227] Copyright 2019, The Royal Society of Chemistry. d–h) Reproduced with permission.^[228] Copyright 2020, Elsevier. i–l) Reproduced with permission.^[232] Copyright 2020, Elsevier. m,n) Reproduced with permission.^[234] Copyright 2018, Elsevier.

(Figure 15f). With the presence of $\text{Cu}_3(\text{HITP})_2$, the new 2D MOF possessed an increased specific surface area, enhanced conductivity, a high capacitance three times that of the single Ni-MOF (Figure 15g), and long-term cycling performance behavior (Figure 15h). Additionally, conducting polymers with excellent conductivity and great electrochemical properties can be used as electron transport circuits for MOF crystals and offer extra capacitance. Zheng's group prepared novel conductive $\text{Cu}_3(2, 3, 6, 7, 10, 11\text{-hexahydroxytriphenylene})_2$ catechol

MOF crystals called p-PPy/Cu-CAT by using porous conducting polymer polypyrrole as the scaffold, which served as the electrode material with an improved EDLC performance.^[229] It was attributed to the uniform dispersion of Cu-CAT crystals on/in the 3D pores of p-PPy, which provided sufficient loading areas and facilitated the diffusion of ion.

2D MOFs can also be used as the precursor of metal oxides/sulfides and their carbonaceous materials, or the target MOF-derived carbons with controllable pores and unique

morphology, by heat or chemical treatment. For instance, highly porous networks of hierarchical CuCo_2S_4 nanosheet arrays were obtained hydrothermally from a MOF precursor, followed by an ion-exchange process,^[230] which exhibited a remarkable volumetric capacitance of more than 2.1 mAh cm^{-3} at 3 mA cm^{-2} , enhanced energy density as well power density for the as-prepared solid-state asymmetric SCs. It is believed that the excellent electrochemical property was due to the unique porous structure of CuCo_2S_4 , which reduced the ion/electron transport pathways, and produced a large number of electroactive sites and volume change buffer.

Zeolite imidazolate frameworks (ZIFs), a subclass of MOFs, inherit the excellent quality of MOFs and zeolites.^[231] Zhao et al. used the ZIF-67 as a sacrificial template and synthesized CuCo_2S_4 nanomaterials with a hierarchical crumpled nanoflower morphology via reflux and solvothermal reactions (Figure 15i).^[232] The optimized CuCo_2S_4 electrode displayed a high specific capacitance of 1344 F g^{-1} at a current density of 1 A g^{-1} and a capacity retention rate of 71.3% at 30 A g^{-1} . As shown in Figure 15j, an asymmetric SC was assembled using the CuCo_2S_4 as the positive electrode and N, F-codoped hierarchical nanoporous carbon polyhedra as the negative electrode, which exhibited an energy density of 55.1 Wh kg^{-1} with a relative power density of 799.8 W kg^{-1} and long cycling with 91.1% retention after 5000 cycles (Figure 15k,l). Furthermore, the preparation of MOF-derived 2D compounds composed of stable metal oxides using carbon-containing nanomaterials is of great significance for SCs.

Hybrid nanomaterials of $\text{Cu}_2\text{O}/\text{Cu}@\text{C}$ nanosheets were prepared from a Cu-MOF precursor that was assembled by Cu(II), 4-(pyridine-4-yl) phthalic acid and 1,4-bis (benzimidazo-1-ly) benzene via a traditional solvent thermal means, and showed a remarkable capacity along with outstanding cycling stability when used as electrode-active materials.^[233] Li et al. prepared novel 2D Cu-MOF nanosheets with a spatial hierarchical stacking (Figure 15m).^[234] Calcination-thermolysis of the 2D Cu-MOF under a N_2 atmosphere produced carbon matrix-supported Cu particles, which were then etched with HCl and activated with KOH to obtain activated porous carbon with abundant holes and irregular gullies (Figure 15n). It displayed an outstanding performance with a specific capacitance of 260.5 F g^{-1} at 0.5 A g^{-1} , and an energy density up to 18.38 Wh kg^{-1} with a power density of 350 W Kg^{-1} . A red LED could be lit up for over 12 min.

5.3. Summary

This section summarizes the mechanisms and applications of various 2D copper-based electrodes in SCs. Although the conductivity is poor as compared with common pseudocapacitive transition metal oxides (such as RuO_2), copper-based materials still play an indispensable role, due to their excellent quality, abundant resources, low manufacturing cost, and easily adjustable synthetic program.

The specific capacitances are compared with results reported in the literature (Table 2). One can see that well-designed Cu–O, Cu–S and Cu–Se systems represent effective electrodes. For copper-based composites with transition metal oxide,

transition metal sulfide, carbon-based materials, and polymers, they mostly show synergistic effects with significant properties.

Compared with the single-phase systems, these advanced composite nanomaterials usually show a high specific surface area and high conductivity, which can increase the accessibility of electroactive sites of electrolyte ions and facilitate fast Faraday reaction kinetics. It is noted that Cu–N and Cu–P systems have inherent good conductivity, corrosion resistance, and significant structural stability, which are promising for practical applications.^[235,236] Studies of their applications as SC electrodes, especially on the 2D level, have remained scarce.^[237]

6. 2D Copper-Based Materials for Rechargeable Ion Batteries

Since Gilbert started battery research in the 1600s, battery has become an indispensable energy storage device in people's daily life.^[238] To meet the growing energy demand, there is an urgent need to explore and develop rechargeable batteries that possess a high energy density, and are safe and environmentally friendly.^[239] Various metal-ions batteries have been the focus of recent research (Figure 16a), such as lithium-ion batteries (LIBs), and sodium-ion batteries (SIBs). Other rechargeable ion batteries, such as potassium-ion batteries (PIBs), and multivalent-ion batteries, such as magnesium-ion batteries (MIBs), aluminum-ion batteries (AIBs), and $\text{Mg}^{2+}/\text{Li}^+$ ion batteries (MLIBs), rarely use 2D copper-based materials as electrode materials. Their key performance parameters are listed and compared in Figure 16b.

6.1. Lithium-Ion Batteries

LIBs have been widely utilized in portable electronics and electric vehicles due to their outstanding theoretical specific capacity (3860 mAh g^{-1}), high power density, low electrode potential along with density ($0.534 \text{ g}^{-1} \text{ cm}^3$).^[240,241] At present, it is considered to be the “heart” of modern electronic products. In this section, the reaction mechanism and the effects of some key parameters on the electrochemical properties of 2D copper-based nanomaterials are analyzed in detail according to the types of materials.^[242]

6.1.1. Mechanistic Insights

An in-depth understanding of the storage mechanism of the anode material is a prerequisite for the rational design of advanced electrode materials. LIBs based on 2D copper-based nanomaterials and their composites as electrodes have been extensively studied. The transition metal compound-based conversion electrodes, either as cathode or anode, can transfer multiple electrons in each molecular formula unit, resulting in a high capacity and high energy density.^[243]

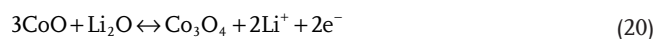
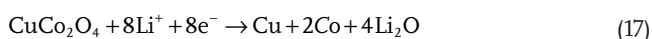
The storage mechanism of Li^+ in CuO is based on a typical conversion reaction, where CuO is converted to a mixture of Li_2O and Cu during charging:^[244]

Table 2. Properties, characteristics and supercapacitive performance of 2D copper-based materials and hybrids for SCs.

Material	Structure/morphology	Synthetic method	Electrolyte	Capacitance	Cycling stability (cycle, current density)	Rate capability	Refs.
CuO	Nanosheet	Template-free	6 M KOH	569 F g ⁻¹ (5 mA cm ⁻²)	82.5% (500 cycles, 5 mA cm ⁻²)	39% from 5 to 30 mA cm ⁻²	[159]
CuO	Film	SILAR	1 M KOH	511 F g ⁻¹ (5 mV s ⁻¹)	–	–	[160]
Ag-CuO	Nanosheet	Silver mirror reaction	6 M KOH	689 F g ⁻¹ (1 A g ⁻¹)	61% (2000 cycles, 1 A g ⁻¹)	44% from 1 to 10 A g ⁻¹	[170]
CuO/Zn-Ni-Co oxide	Nanosheet	Hydrothermal	3 M KOH	1261 C g ⁻¹ (1 A g ⁻¹)	92.2% (20 000 cycles, 20 A g ⁻¹)	74% from 1 to 8 A g ⁻¹	[167]
Cu ₂ O/CuMoO ₄	Nanosheet	Hydrothermal	2 M KOH	4264 F g ⁻¹ (1 A g ⁻¹)	86.6% (3000 cycles, 5 A g ⁻¹)	73% from 1 to 10 A g ⁻¹	[176]
Cu ₂ O/CuO	Nanosheet	Chemical etching	6 M KOH	834.2 F g ⁻¹ (3.57 A g ⁻¹)	85.6% (5000 cycles, 5 mA cm ⁻²)	68.5% from 5 to 30 mA cm ⁻²	[178]
Ni(OH) ₂ /Cu ₂ O/NiCu	Nanosheet	Hydrothermal	6 M KOH	823.4 C cm ⁻³ (20 mA cm ⁻²)	113% (10 000 cycles, 20 mA cm ⁻²)	40% from 20 to 2 00 mA cm ⁻²	[175]
CuCo ₂ O ₄	Nanosheet	Hydrothermal	6 M KOH	1131 F g ⁻¹ (1 A g ⁻¹)	79.7% (5000 cycles, 10 A g ⁻¹)	36% from 1 to 50 A g ⁻¹	[157]
CuCo ₂ O ₄ @MnMoO ₄	Nanosheet	Hydrothermal	6 M KOH	1327.5 F g ⁻¹ (1 A g ⁻¹)	92.8% (6000 cycles, 5 A g ⁻¹)	79.4% from 1 to 20 A g ⁻¹	[119]
CuCo ₂ O ₄ -MnO ₂	Nanoflake	Hydrothermal	1 M KOH	1458 F g ⁻¹ (0.5 A g ⁻¹)	93% (5000 cycles, 20 A g ⁻¹)	62% from 0.5 to 2.5 A g ⁻¹	[192]
CuCo ₂ O ₄ /MnCo ₂ O ₄	Bilayer	Hydrothermal	2 M KOH	1434 F g ⁻¹ (0.5 A g ⁻¹)	96.9% (5000 cycles, 20 A g ⁻¹)	56.5% from 0.5 to 15 A g ⁻¹	[191]
NiCo ₂ S ₄ @NiCu-LDH	Nanosheet	Solvothermal	2 M KOH	632.0 μAh cm ⁻² (2 mA cm ⁻²)	74% (3000 cycles, 10 mA cm ⁻²)	84.5% from 2 to 20 mA cm ⁻²	[184]
CuS	Nanosheet	Microwave assisted	2 M KOH	2535 F g ⁻¹ (1 A g ⁻¹)	92% (3000 cycles, 20 A g ⁻¹)	86.7% from 1 to 20 A g ⁻¹	[197]
Graphene/CuS	Nanoplatelet	Solvothermal	6 M KOH	497.8 F g ⁻¹ (0.2 A g ⁻¹)	91.2% (2000 cycles, 10 A g ⁻¹)	66.8% from 0.2 to 1 A g ⁻¹	[132]
CuS/Cc	Nanosheet	Electrodeposition	2 M KOH	4676 mF cm ⁻² (2 mA cm ⁻²)	82.8% (10000 cycles, 15 mA cm ⁻²)	50% from 2 to 10 mA cm ⁻²	[81]
CuS/MnS	Cluster	Hydrothermal	3 M KOH	1144 F g ⁻¹ (1 A g ⁻¹)	85.9% (10000 cycles)	40.8% from 1 to 100 A g ⁻¹	[198]
CuCo ₂ S ₄	Nanosheet	Hydrothermal	3 M KOH	3321.6 F g ⁻¹ (5 A g ⁻¹)	87.1% (3000 cycles)	88.3% from 5 to 30 A g ⁻¹	[203]
CuCo ₂ S ₄	Nanosheet	Ion exchange	2 M KOH	409.2 mAh g ⁻¹ (3 mA cm ⁻²)	94.2% (10000 cycles)	77.9% from 3 to 50 mA cm ⁻²	[230]
F-CuCo ₂ S _{4-x}	Nanoflake	Hydrothermal	1 M KOH	2202.7 C g ⁻¹ (1 A g ⁻¹)	96.7% (5000 cycles, 20 A g ⁻¹)	53.7% from 1 to 20 A g ⁻¹	[107]
Cu ₂ Se@CuS	Nanosheet	Electrodeposition	6 M KOH	2727 F g ⁻¹ (2.5 mA cm ⁻²)	70.2% (8000 cycles, 5 mA cm ⁻²)	94% from 2.5 to 8.3 mA cm ⁻²	[82]
Cu ₂ Se@Co ₃ Se ₄	Nanosheet	Hydrothermal	2 M KOH	1005 F g ⁻¹ (1 A g ⁻¹)	94.2% (10000 cycles, 20 A g ⁻¹)	56% from 1 to 10 A g ⁻¹	[217]
Cu ₂ WS ₄	Nanosheet	Exfoliation	PVA-LiCl	583.3 F cm ⁻³ (0.31 A cm ⁻³)	95% (3000 cycles, 1.25 A cm ⁻³)	53.8% from 0.3 to 1.25 A cm ⁻³	[212]
CuSe@Ni(OH) ₂	Film	Electrodeposition	PVA-LiCl	38.9 F cm ⁻³ (0.05 mA cm ⁻²)	100% (10000 cycles, 0.3 mA cm ⁻²)	50% from 0.05 to 0.25 mA cm ⁻²	[218]
CuSe@PANI	Nanosheet	Electrodeposition	1 M H ₂ SO ₄	308.9 mF cm ⁻² (1 mA cm ⁻²)	89.8% (30000 cycles, 10 mA cm ⁻²)	32.3% from 1 to 15 mA cm ⁻²	[219]
CuSe@FeOOH	Nanosheet	Electrodeposition	1 M LiCl	282 mF cm ⁻² (3 mA cm ⁻²)	95% (32000 cycles, 0.65 mA cm ⁻²)	32% from 3 to 12 mA cm ⁻²	[220]
Cu-MOF@δMnO ₂	Nanosheet	Ultrasonic treatment	1 M Na ₂ SO ₄	667 F g ⁻¹ (1 A g ⁻¹)	95% (6000 cycles, 4 A g ⁻¹)	53.6% from 1 to 10 A g ⁻¹	[226]
Ni//Cu MOF	Nanosheet	In-plane assembly	1 M KOH	1424 F g ⁻¹ (2 A g ⁻¹)	94.3% (7000 cycles, 1 A g ⁻¹)	40.4% from 2 to 32 A g ⁻¹	[228]



Another metal element is usually introduced to enhance the conductivity of the electrode and inhibit agglomeration. Numerous kinds of metals can deliver rich electrochemical redox reactions and achieve synergistic effects through mutual reinforcement or modification. Taking CuCo₂O₄ as an example, its electrochemical behavior in LIB can be expressed as:^[245]



The reaction between Cu-S and Li⁺ is a replacement reaction rather than a typical transition metal oxide insertion reaction. Based on the redox conversion reaction, the final products in LIBs are Cu (Cu_xS) and Li₂S. The electrochemical process can be described as:^[22]



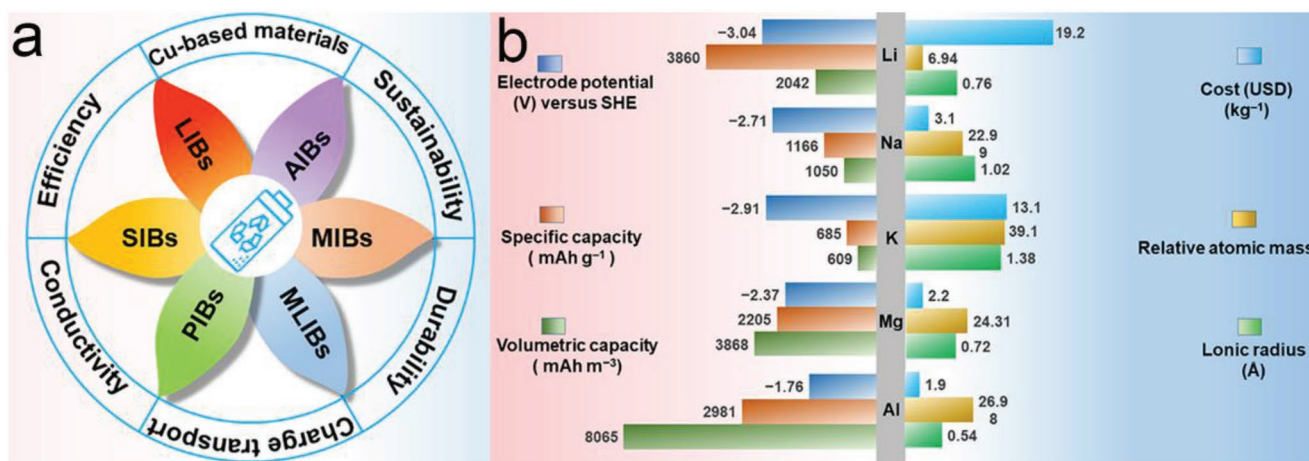
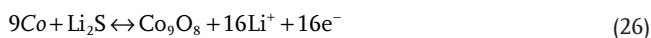
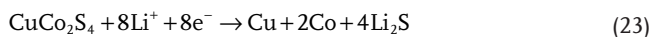


Figure 16. a) Schematic diagram of 2D Copper-based materials used in rechargeable ion batteries. b) Comparison of characteristics of representative metals for rechargeable ion batteries.



Similarly, the conversion mechanism of CuCo_2S_4 during discharge and charging can be expressed as follows:^[246]

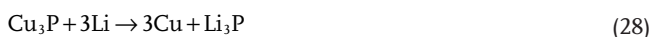


Cu_3N plays an important role in accelerating the uniform nucleation of Li and constructing Li_3N inorganic phase with high electron/Li ion conductivity.^[247] The conversion reaction requires heterogeneous charge transfer at the interface, Cu–N bond fracture and Li^+ diffusion in solid state. The reaction in which the maximum lithium uptake of the elements is admitted can be expressed as follows:^[248]



Li_3N displays a high conductivity and high thermal mechanical stability, as compared to Li metal, and can enhance the reversible Li plating/stripping by inhibiting the formation of Li dendrites.^[249]

Likewise, for Cu_3P , the reaction is^[250]



6.1.2. Applications

Graphite is the most commonly used anode of LIBs, but it is inherently limited by the maximum theoretical capacity of 372 mAh g⁻¹. Further improvements require major changes of the anode materials when LiC_6 is formed. Until now, a series of CuO nanomaterials have been developed as electrode

materials for LIBs with the theoretical specific capacity up to 674 mAh g⁻¹.^[251,252] Yet, there are three main issues of CuO, namely, low electrical conductivity, slow diffusion, and large volume expansion during discharge–charge processes, which hinder their wide applications.^[253–255] Effective preparation techniques help to obtain materials with unique microstructure and morphology and improve the electrochemical performance.^[256] A facile frequency reactive magnetron sputtering method has been applied to synthesize CuO thin films with a high reversible capacity by Pecquenard et al.^[257] Similar work was carried out by Chen et al. who synthesized CuO thin films as the anode materials.^[258] At 100 mA g⁻¹, the capacity reached up to 703 mAh g⁻¹ in the potential range of 0.01 to 3.0 V, and after 100 cycles at 1000 mA g⁻¹, the capacity was retained at 465 mAh g⁻¹. In addition, Mohapatra et al. used nanoplate and mulberry-like porous CuO as anode materials. Compared with mulberry-like porous CuO, the capacity of the nanoplate electrode was 279.3 mAh g⁻¹ at 1 C and 150.2 mAh g⁻¹ at 4 C.^[259] Liu and co-workers observed that ionic liquid 1-butyl-3-methylimidazolium chloride played the roles of both effective templates and structure-directing agents in accurately tuning the crystallographic facets and morphologies of CuO architectures (Figure 17a,b).^[260] The nanosheet component was bonded by (001) faces of the bottom and top surfaces. The synergistic effect of the exposed (001) surface and the layered microstructure of the nanosheet module greatly promoted the diffusion and electron transport. Another example of the facile fabrication of 2D CuO nanoflake arrays was reported by Liu et al.^[261] From the SEM image in Figure 17c, nanoplates could be clearly seen with a highly open nanostructure. It was found that the CuO electrode showed a high discharge capacity of 1343.5 mAh g⁻¹ at the current density of 0.3 C and a good capacity retention after 120 cycles. Despite the capacity loss of the electrode, the coulomb efficiency of the electrode remained high, and the original 2D nanoflake structure was maintained after the cycle test, without powder and aggregation phenomenon (Figure 17d). Pu et al. prepared porous CuO nanosheets/RGO by in situ oxidation and annealing, and the resulting nanocomposites possessed a high specific capacity (Figure 17e), rate capacity and columbic efficiency (Figure 17f).^[262] This was due

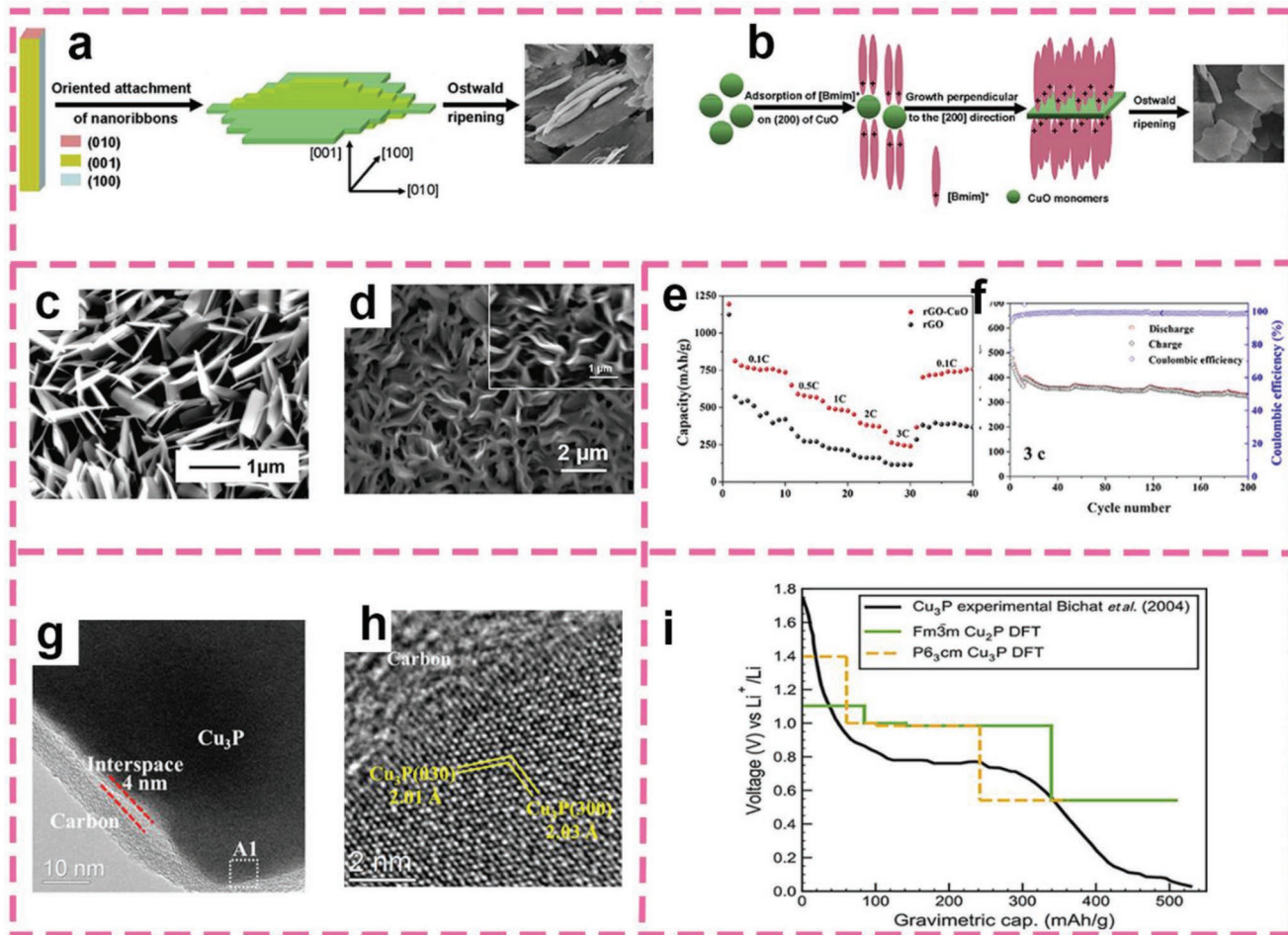


Figure 17. a) Schematic illustration of the possible formation process of CuO architectures. b) Schematic illustration of the possible formation process of CuO nanoplates. c) SEM images of CuO after dehydration of $\text{Cu}(\text{OH})_2$. d) The CuO electrode after cycling test. The inset of d) presents a magnified area of (d). e) Rate performance of CuO/RGO nanocomposite and RGO electrodes, up to 200 cycles, at a current rate of 3C. f) Charge/discharge capacities and coulombic efficiency of the CuO/RGO nanocomposite and RGO electrodes, up to 200 cycles, at a current rate of 3C. g) HRTEM images of $\text{Cu}_3\text{P}@C-900$. h) SAED images of $\text{Cu}_3\text{P}@C-900$. i) Ground-state voltage profile for $Fm\bar{3}m\text{-Cu}_3\text{P}$ and $P6_3cm\text{-Cu}_3\text{P}$ generated from the DFT ground-state structures of Cu-Li-P . a,b) Reproduced with permission.^[260] Copyright 2016, Elsevier. c,d) Reproduced with permission.^[261] Copyright 2019, Elsevier. e,f) Reproduced with permission.^[262] Copyright 2019, Elsevier. g,h) Reproduced with permission.^[289] Copyright 2018, Elsevier. i) Reproduced with permission.^[284] Copyright 2020, American Chemical Society.

to the uniform dispersion and firm combination between CuO nanosheets and RGO flakes, which could effectively prevent the agglomeration of active materials and reduce the volume change in the process of repeated charge and discharge.

Although 2D CuO could provide a large number of active sites on the surface and a smaller volume expansion than their bulk counterpart, they still suffer from poor reaction kinetics and delayed storage of potential.^[263] Unfortunately, the Li storage performance of single metal oxide is poor, and the preparation of bimetallic oxide can improve the performance. In 2014, Liu and co-workers reported the synthesis of $\text{Cu}_x\text{Co}_{3-x}\text{O}_4$ nanosheets and observed a high capacity and high rate for Li storage.^[264] The reversible capacity capacities were found to be 1135 mAh g^{-1} at 0.1 C, with only a 2.5% decay of the capacity at 400 mA g^{-1} after 50 cycles. In 2018, Pawar et al. fabricated high-density CuCo_2O_4 nanosheets with a thickness of 10–15 nm by depositing copper-cobalt hydroxide precursor film on Ni foam

at 1.0 V for 300 s, followed by annealing.^[265] The nanosheets possessed a high initial discharge capacity of 1244 mAh g^{-1} at 0.1 A g^{-1} , and stable cyclability of 1100 mAh g^{-1} at 1 A g^{-1} over 200 cycles. Highly porous CuCo_2O_4 nanosheets with an average thickness of about 36 nm were synthesized by Li et al.,^[266] and displayed an excellent rate, retaining over 1104 mAh g^{-1} at a current density of 2 A g^{-1} , and 656 mAh g^{-1} at 5 A g^{-1} .

Other materials, such as Cu-S, Cu-N and Cu-P, have nanostructures of various dimensions, but the 2D forms are rarely used for LIBs. CuS and Cu_2S possess a theoretical decent discharge capacity of 561 mAh g^{-1} and 337 mAh g^{-1} , respectively.^[267] Despite these huge advantages, copper sulfide anode materials typically suffer from severe capacity fading and poor cycling, mainly due to the large volume change and formation of polysulfide $\text{Li}_2\text{S}_x (2 < x < 8)$. Li_2S_x is the intermediate product of electrochemical reactions during Li^+ insertion/extraction and can be easily dissolved into the electrolyte or transferred to the

electrode surface, resulting in the shuttle behavior and a rapid reduction in capacity.^[268] In 2012, Du et al. prepared hexagonal CuS nanosheets, with a thickness of 3.2 nm and plane size up to ≈ 453 nm, which exhibited a capacity as high as 285 mAh g^{-1} at 2 A g^{-1} and good cycling stability.^[269] Wang et al. fabricated copper sulfide with different stoichiometry and found that copper sulfide with “excess copper” maintained a good capacity and could be charged and discharged at high rates as an electrode. It should be noted that the key factor for obtaining a high performance of Cu_xS electrode is that the ratio of Cu to S is not less than 2.^[270]

Constructing isocomponent hybrids and cocomponent hybrids is a practical and effective approach. Due to the synergistic effect of CuS nanosheets and graphene, it can buffer volume expansion, prevent cracking, and promote the insertion and deinsertion of Li^+ . Iqbal et al. synthesized 2D polyaniline anchored CuS/graphene nanoactive composites, which delivered an ultrahigh reversible capacity of 1255 mAh g^{-1} and a capacity decay rate of merely 0.75% per cycle up to 250 cycles.^[271] With one-pot sulfurization, 2D $\text{Co-Cu}_2\text{S@C}$ nanostructures were developed by Qing et al.^[272] Compared with most reported copper sulfide-based anodes, the as-prepared samples demonstrated a high specific capacity of 780 mAh g^{-1} after 300 cycles. Remarkably, Li et al. impregnated sulfur in situ in a multifunctional metal sulfide matrix with electroactivity and conductivity and constructed CuS@S hybrid nanosheets, which exhibited a specific capacity of 514.4 mAh g^{-1} at 0.1 A g^{-1} after 200 cycles.^[273] However, as the anode material of LIBs, CuS has a large voltage lag (about 0.8 V) and a high lithium delithiation potential. Liu's group reported a heterostructure concept, by taking advantage of both MnS and CuS.^[274] The as-formed CuS/MnS-C heterostructure nanofibers were beneficial to charge separation and transfer, and further promoted the structural stability and conductivity of the kinetic hybrid electrode. As a consequence, the voltage-hysteresis values of the CuS anode were lowered to 0.30 and 0.35 V. Moreover, the electrode demonstrated the best electrochemical performance in terms of both rate capability and coulombic efficiency among relevant electrodes. Besides the abovementioned typical Cu_2S and CuS, bimetallic 2D Cu-S systems have also been widely used for sustainable energy-storage devices.^[275]

Cu_3N plays a unique role in inhibiting lithium metal dendrites at interface and collector engineering because of its stable chemical structure, high ionic conductivity, and good affinity for lithium.^[276] Cu_3N with a cubic crystal structure and large voids can accommodate Li atoms.^[277,278] In addition, based on the reversible $\text{Li}/\text{Cu}_3\text{N}$ conversion process, Cu_3N as cathode material has been studied experimentally, which confirmed that Li was inserted into Cu_3N . Wang et al. inspected the diffusion and storage capacity of Li in Cu_3N bulk crystal and nanosheets by first-principles calculations.^[279] Due to the low energy barrier (0.09 eV) and the absence of agglomeration, Li atoms are attached to Cu_3N nanosheets, reaching a maximum Li capacity of about 1008 mAh g^{-1} .

Copper phosphide has long been considered as a perfect material to replace graphite (especially Cu_3P), because not only the theoretical gravimetric energy densities of Cu_3P is close to that of graphite (377 vs 372 mAh g^{-1}), but also its volumetric capacity is more than three times that of graphite (2778 vs

830 mAh L^{-1}).^[280] Additionally, it has a compatible voltage platform and superior cycle performance compared to other transition metal binary phosphates.^[281] Cu_3P films prepared on copper plates through hybrid electrochemical deposition and low-temperature solid-state synthesis have been found to remarkably improve capacity retention and rate capability characteristics.^[282] Unfortunately, due to common problems, such as volume expansion/contraction, structural transformation, and irreversible formation of some certain species, Cu_3P displays only a low conductivity, and its capacity rapidly decreases to 200 mAh g^{-1} after several cycles.^[283,284] Useful strategies to deal with these issues include designing nanosized morphologies with improved electron and ion diffusion kinetics, and constructing hybrid materials by coupling Cu_3P with carbonaceous materials.^[285] 2D nanostructures with abundant surface states and large surface areas are conducive to side reactions between electrodes and electrolytes, resulting in a large number of irreversibly captured Li^+ .^[286,287] As far as we know, 2D plate-like Cu_3P was previously synthesized by solvothermal synthesis.^[288] Unfortunately, this method requires strict and complex reaction conditions with toxic phosphorus precursors, which is dangerous and time-consuming. 3D superstructure of carbon-wrapped, single-crystalline Cu_3P porous nanosheets were successfully synthesized by a simple and environmentally friendly epitaxial growth technique.^[289] From the image (Figure 17g), the $\text{Cu}_3\text{P@C}$ sample can be seen to exhibit tight contact between the Cu_3P nanosheets and carbon shell, along with other noncontact areas with 4 nm void space. The former facilitated the contact between the electrode and electrolyte (Figure 17h), while the latter was conducive to reducing the destructive effect of Cu_3P volume change during Li^+ insertion and extraction. Naturally, the growth of these nanobelts and nanosheets was accompanied by the diffusion of P atoms from the outer to the inner surface. Compared with bulk Cu_3P powder, the as-prepared $\text{Cu}_3\text{P@C}$ retained a specific capacity of 540 mAh g^{-1} after 50 cycles at 37 mA g^{-1} . More importantly, Harper et al. carried out DFT calculations and found that Cu_2P possessed a higher capacity than the previously studied graphite anode and Cu_3P , and its capacity was about 508 mAh g^{-1} .^[284] As shown in Figure 17i, it can be used as a conversion anode for LIBs.

Cu-MOFs materials have high potential in the field of LIBs because of their high specific surface area and tunable porosity.^[290,291] Most common MOFs are insulators, which, as the electrode materials for LIBs, are prone to volume expansion during cycling, leading to a limited electrochemical performance.^[292] Graphene has been used as a structural scaffold as it stabilizes the physical structure during charge-induced volume expansion, thereby improving the conductivity of metal oxides.^[293] Guo and co-workers prepared CuO-graphene (CuO-G) composites by pyrolyzing graphene and Cu-MOF,^[294] which possessed better Li-cycling and capacity than individual CuO and Cu-MOF. Furthermore, MOFs usually need subsequent complicated heat treatments to boost the conductivity.^[295] Therefore, Nazir et al. prepared a composite $\text{Si@Cu}_3(\text{HITP})_2$ by using 2D conductive MOF with Cu and Si nanoparticles by a simple in situ growth method, without the need of heat treatment.^[296] Sealing the Si nanoparticles within the Cu-MOF was found to produce an ideal buffer against the volume expansion,

which led to a reversible Li^+ storage capacity of 2551 mAh g^{-1} in the first cycle, approximately 78.5% of the coulombic efficiency.

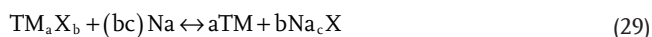
Since copper-based MOFs contain elements such as Cu, C, O and others, the final MOF-derived carbons can be obtained by pyrolysis at 500°C to prepare 2D layered Cu-BDC MOF, and then further etching.^[297] This preparation process is relatively simple and has considerable commercial potential.^[298] The electrode with abundant mesopores maintained a reversible capacity of 690.4 mAh g^{-1} after 500 cycles at a current density of 5.0 A g^{-1} . Given all of that, 2D copper-based materials are indeed suitable energy storage materials for LIBs.

6.2. Sodium-Ion Batteries

Similar to LIBs, SIBs are considered as a promising energy storage device because of the large amount of sodium ($\approx 2.5\%$) in the earth's crust, and its almost unlimited availability in seawater has greatly reduced its cost. In addition, the safety and appropriate redox potential ($E_{\text{Na}^+/\text{Na}} = -2.71 \text{ V}$ vs the standard hydrogen electrode (SHE), which is only slightly lower than the lithium electrode) suggest that there is only a small amount of energy loss in the utilization of SIBs.^[299,300]

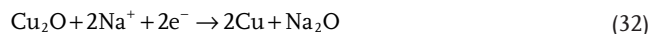
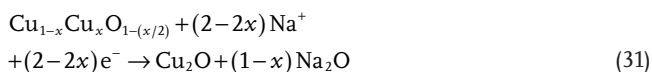
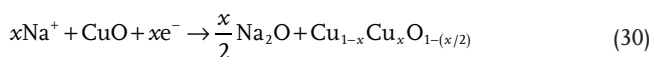
6.2.1. Mechanistic Insights

Na is located below Li in the periodic table, and the composition and working principle of SIBs are very similar to those of LIBs. Figure 18a shows a schematic diagram of a SIB, which consists of two Na^+ storage electrodes, a Na^+ conductive electrolyte and a separator.^[301] In the electrical storage mechanism, ions migrate between the cathode and anode through the intermediate electrolyte.^[302] The two electrodes have different compositions, allowing the reversible insertion and extraction of Na^+ . During normal charge and discharge process, the Na^+ intercalation proceeds smoothly without damaging the chemical structure of the electrode.^[303] At present, the electrochemical process of SIB anode includes insertion/extraction reaction, conversion reaction and alloy dealloying reaction, among which the conversion reaction is significant for transition metal oxides and sulfides. Generally speaking, the conversion reaction mechanism can be described as follows:

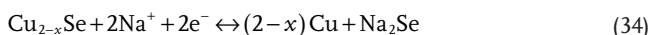


where TM represents the transition metal, X is anion, and c the formal oxidation state of X.

Take CuO as an example. Previous studies have shown that Na^+ ions are first inserted into CuO to form $\text{Cu}_{1-x}\text{Cu}_x\text{O}_{1-(x/2)}$. The Cu_2O phase is formed. Finally, the Cu_2O phase is further reduced to Cu and Na_2O .^[304] The following equations describe the three-step reaction mechanism of CuO electrode in SIBs:



Employing ex situ XRD, XPS, and Raman analysis, as well as electrochemical methods, Xiao et al. showed that a Cu_{2-x}Se phase was formed in the first sodiation process, and then Cu and Na_2Se were formed by transforming Cu_{2-x}Se in the next charge-discharge process.^[305] Therefore, the total electrochemical process can be expressed as:



For Cu_3P , the electrochemical reactions involved can be described as follows:^[306]



6.2.2. Applications

However, due to the larger ionic radius and heavier atomic mass of Na^+ in the host material, its reaction kinetics in the electrode materials is slower, resulting in continuous reversible capacity attenuation and poor cycle stability.^[307] To address these issues, Fan et al. mixed CuO nanosheets with different binders, and the addition of carboxymethyl cellulose led to a capacity of 307.1 mAh g^{-1} at 2000 mA g^{-1} , much higher than with poly(vinylidene) fluoride.^[308] Similarly, Rath and co-workers studied and compared the morphology-related performance of different CuO nanostructures as negative electrode materials for SIBs.^[309] Considering that the theoretical capacity of 560 mAh g^{-1} ,^[310] Li et al. synthesized CuS-RGO composites as anode for the first time and optimized the cutoff voltage.^[311] Kim's group hybridized CuS nanodisks with acid-treated single-walled carbon nanotubes,^[312] and the resulting nanohybrids were found to increase the storage of Na^+ through step-wise activation with increasing current density and cycles. The reversible capacity reached the maximum of 610 mAh g^{-1} and maintained over the 500 cycles without obvious capacity attenuation. To further improve the cycle stability and specific capacity, Gong et al. prepared $\text{CuCo}_2\text{S}_4/\text{rGO}$ nanocomposites, which delivered a stable reversible capacity of 433 mAh g^{-1} at 0.1 A g^{-1} , and 336 mAh g^{-1} at 1 A g^{-1} .^[313]

Metal selenides have weaker electronegativity, larger ionic radius, higher conductivity, and lattice volume than metal sulfides, so they have better potential application in SIBs.^[314] Early in 2013, Cu_{2-x}Se was used as the anode with a specific capacity of 120 mAh g^{-1} after 100 cycles.^[315] Recently, Lin et al. improved the storage capacity to 295 mAh g^{-1} at 10 A g^{-1} by designing a cubic phase CuSe with crystal-pillar-like morphology self-assembled by the nanosheets.^[316] Yu et al. prepared CuSe nanosheets of 5 nm in thickness by hydrothermal synthesis and observed an outstanding electrochemical performance, with a capacity of 404 mAh g^{-1} after 100 cycles at 0.1 A g^{-1} .^[317] Unexpectedly, Xiao's group found a high ratio of pseudocapacitive contribution in Cu_2Se -CTAB nanocomposites by a green synthesis method, as shown in Figure 18b.^[305] The nanocomposites delivered a large average reversible capacity

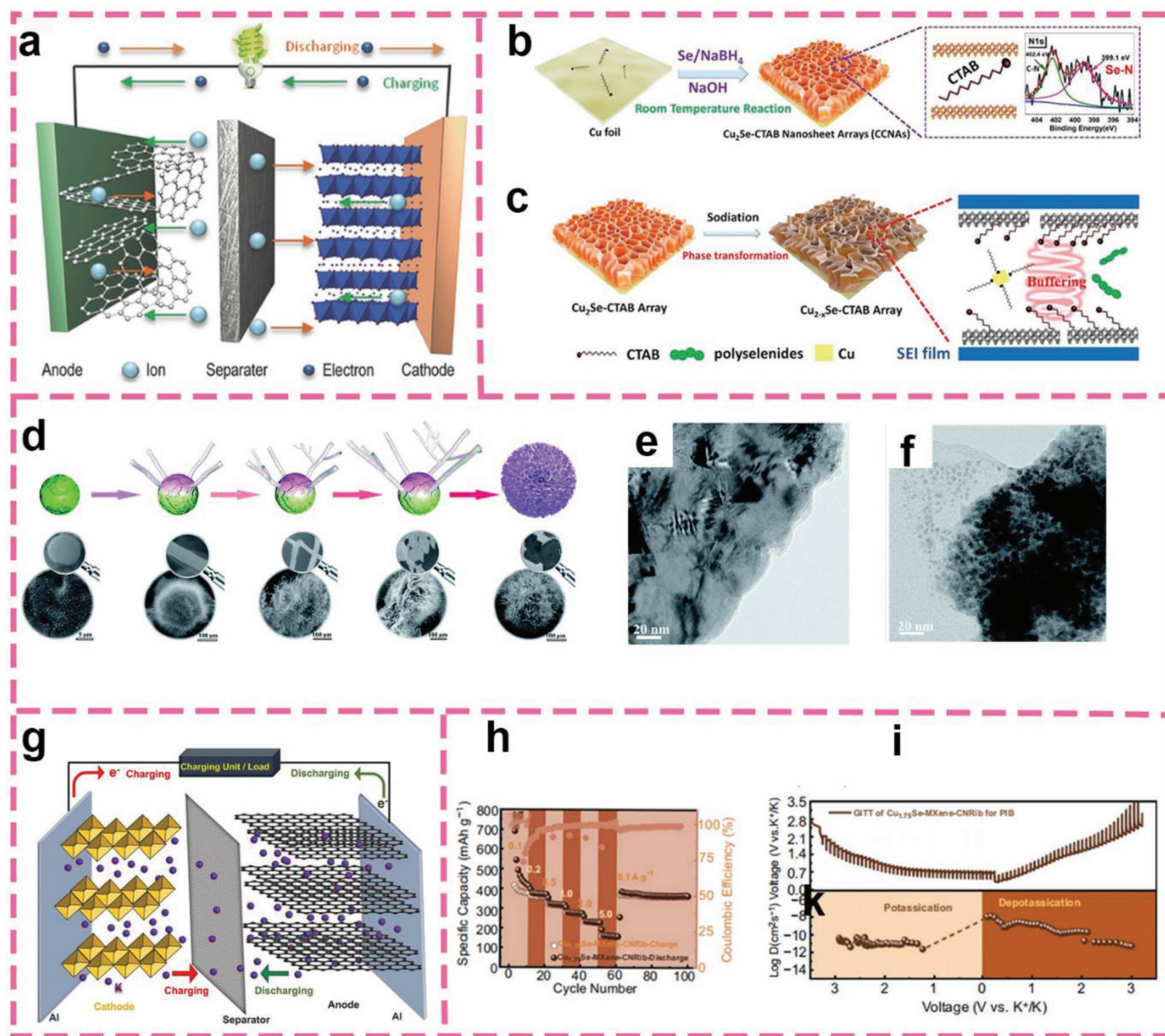


Figure 18. a) Schematic illustration of SIBs. b) Schematic of the fabrication process of the Cu_2Se -CTAB nanosheet arrays and the N1s spectrum of Cu_2Se -CTAB. c) Schematic showing the mechanism involved the phase transformation and enhanced performance of Cu_2Se -CTAB nanosheet arrays in sodium ion storage. d) Schematic representation of growth mechanism of the $\text{Cu}_3\text{P}@C_5$ and corresponding SEM images from samples removed when the temperature reached $800\text{ }^\circ\text{C}$ and then for $900\text{ }^\circ\text{C}$ after 1, 5, 30, and 60 min. e) TEM images of $\text{Cu}_3\text{P}@C_5$ after 300 cycles at 0.1 A g^{-1} . f) Cu_3P after 300 cycles at 0.1 A g^{-1} . g) Schematic representation of working principle of KIBs. h) Rate capabilities. i) GITT profiles and corresponding D_K values. a) Reproduced with permission.^[301] Copyright 2016, Wiley-VCH. b, c) Reproduced with permission.^[305] Copyright 2020, Wiley-VCH. d–f) Reproduced with permission.^[321] Copyright 2019, The Royal Society of Chemistry. g) Reproduced with permission.^[326] Copyright 2020, Wiley-VCH. h–k) Reproduced with permission.^[334] Copyright 2020, Springer Nature.

of 426 mAh g^{-1} at 0.1 A g^{-1} , excellent rate capability exceeding 238.1 mAh g^{-1} at 30 A g^{-1} , and ultra-long cycle lifetime over 6500 cycles at 20 A g^{-1} . The intercalation of CTAB in the inter-layer space of the crystal was of great significance for improving the electrochemical performance of Cu_2Se -CTAB nanosheet arrays (Figure 18c) by widening the void space, alleviating the volume expansion of materials, inhibiting the fast growth of Cu particle and hindering the shuttling of negative polyselenides.

Studies of the use of Cu_3P as a qualified anode in SIBs so far show that the synergistic effect of the high conductivity of copper frames and excellent sodium storage capacity of

phosphorus (2596 mAh g^{-1} , based on formation of Na_3P) is expected to improve the sodium storage performance.^[318,319] However, like other conversion anode materials, the synthesized metal phosphides are usually composed of irregular large-size particles, which are not conducive to the diffusion of solid ions.^[320] Fan et al. synthesized additive-free Cu_3P based on a Cu current collector that exhibited an excellent reversible capacity of 349.7 mAh g^{-1} at 50 mA g^{-1} .^[306] By varying the calcination time (Figure 18d), carbon shells of 5 nm and 15 nm in thickness were obtained producing the samples of $\text{Cu}_3\text{P}@C_5$ and $\text{Cu}_3\text{P}@C_{15}$.^[321] From Figure 18e, it can be found that $\text{Cu}_3\text{P}@C_5$

retained the original 2D nanoflake structure after cycling tests without obvious crushing or aggregation, further illustrating the apparent structural stability of the Cu₃P@C5 electrodes. In stark contrast (Figure 18f), the circulation of Cu₃P powders caused considerable damage, and a large number of small Cu metal particles can be observed. Therefore, the Cu₃P@C5 displayed a high capacity of 286 mAh g⁻¹ at 0.1 A g⁻¹ with a long cycling life that exceeded 300 cycles, a reversible capability of 156 mAh g⁻¹ at a considerably high current rate of 1 A g⁻¹ after 1000 cycles. A similar strategy was universally used in several studies.^[322] The heterostructure could offer an adequate internal space to release mechanical strain, avoid the aggregation of nanosheets induced by huge volume expansion during repeated Na⁺ insertion/extraction, greatly shorten electron/ion diffusion pathways, as well as create more active sites.

6.3. Potassium Ion Batteries

PIBs have quickly attracted widespread attention because of rich potassium resources, high theoretical capacity (685 mAh g⁻¹) and low cost. Potassium is another alkaline element after sodium, and may have more advantages than lithium and sodium.^[323] Meanwhile, compared to Na⁺/Na, the lower electrochemical potential of K⁺/K (-2.93 V vs SHE) results in a higher working voltage for PIBs than for SIBs.^[324] Another significant advantage of PIBs over LIBs and SIBs is that the Lewis acidity of K ions is much weaker, resulting in smaller solvated ions than Li⁺ and Na⁺. Another profitable point is the “internal fuse function” brought by the low melting point (63.4 °C) of potassium metal. Therefore, the conductivity and amount of solvated and transported K⁺ will exceed that of Li⁺ and Na⁺.^[325]

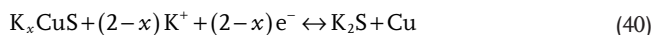
6.3.1. Mechanistic Insights

Similar to SIBs, ions are shuttled between the cathode and anode in PIBs in a rocking chair fashion through a nonaqueous or aqueous electrolyte. Yet, unlike SIBs and LIBs, potassium does not form an alloy when contacting aluminum at a low voltage. Figure 18g depicts the different components of the PIB responsible for the charge/discharge mechanism and storage.^[326] Therefore, the cost can be reduced by replacing the copper substrate with aluminum on the anode side. When the battery is discharged through the external load, ions are deinserted from the anode side and moved to the cathode through the separator and electrolyte.^[327,328] During this process, electrons migrate from the anode to the external load. Most 2D copper-based anodes used for PIBs are of the conversion-type materials.

For instance, Gao et al. prepared nitrogen-doped carbon microfiber networks decorated with CuO/Cu clusters and studied their storage behaviors. The anode was found to offer a large number of active reaction sites and reduce the K⁺ diffusion distance.^[329] There are three biphasic reactions, as described below:^[330]



Similarly, for CuS, the electrochemical process can be expressed as:^[331]



6.3.2. Applications

In the past few years, the search for new electrode materials has been intensified; yet, studies on the application of 2D CuO in PIBs have remained scarce. In a recent study, a CuO nanoplate electrode exhibited a capacity in PIBs of 342.5 and 163 mAh g⁻¹ at 0.2 and 2.0 A g⁻¹, respectively, and an excellent cycle life of 78.4% at 1 A g⁻¹ over 100 cycles.^[330] Lin et al. achieved an outstanding anode performance of a PIB based on Se-substituted CuS nanoflakes, and found that the batteries retained a capacity rate of 100% after 600 cycles under 2 A g⁻¹.^[332]

Since the stability of a solid-electrolyte interphase (SEI) layer is a significant factor in determining the performance, designing ideal anode materials with a shell layer structure through the confinement effect may be an effective strategy to further enhance cycling stability and coulombic efficiency. Cao et al. constructed a core-shell CuS-C@Nb₂O₅-C nanofiber anode, in which the CuS nanoplates were confined in the Nb₂O₅-C layers to prevent direct contact with the electrolyte during the charge/discharge process and to mitigate volume expansion, thereby rapidly forming a successive SEI layer.^[333] Compared with Nb₂O₅-C and CuS-C, the core-shell nanofibers exhibited a much enhanced electrochemical performance, displaying a stable coulombic efficiency, which increased rapidly from 62.5% to 99.0% after 5 cycles and stabilized at more than 99.5% after 10 cycles. The stable K⁺ capacity reached 95.1 mAh g⁻¹ at 2 A g⁻¹ after 2000 cycles, with a coulombic efficiency of about 100%. In another study, Cu_{1.75}Se-MXene-CN Rib (fungal-derived N-rich carbonaceous nanoribbons), a novel 2D strongly coupled ternary heterostructure, has also been used as a PIB anode.^[334] Figure 18h,i depicted the electrochemical performance, where the highest reversible K⁺ storage capacity was about 435.3 mAh g⁻¹ at 0.1 A g⁻¹ with the K⁺ diffusion coefficients (*D_K*) of 10⁻⁸–10⁻¹⁰ cm² s⁻¹. Even after 400 cycles, a reversible capacity of 305.6 mAh g⁻¹ was delivered by the CuS-C@Nb₂O₅-C NFs electrode, and 93.1% of the capacity was retained with the capacity loss for each cycle at only 0.405 mAh g⁻¹.

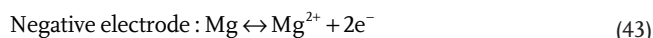
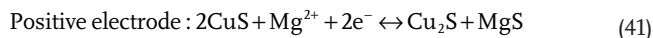
6.4. Multivalent-Ion Batteries

6.4.1. Mechanistic Insights

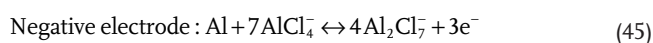
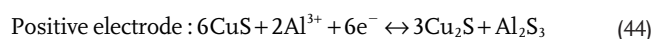
CuS is considered as a promising cathode material for MVIBs due to the high theoretical capacity. Ren's group used a one-step liquid phase method to prepare graded CuS porous nanocages

assembled by nanosheets.^[335] The electrochemical energy storage mechanism of conversion materials is based on general chemical bond breaking, and a certain element or component combines with metal ions to form compounds. According to the analysis of ex situ XRD and CV measurements, the electrochemical process of CuS can be expressed as:

For MIBs,



For AIBs,



6.4.2. Applications

Magnesium is the fifth abundant element in the earth's crust and the electrochemically deposited Mg^{2+} does not form a dendritic structure, with an almost 100% Coulombic efficiency.^[336] The divalent nature of Mg^{2+} has always been an obstacle to rapid insertion kinetics, but this can be an opportunity to achieve a maximum capacity. The ionic radius of Mg^{2+} is similar to that of Li^{+} , which makes it likely that the electrode materials that have been successfully used for LIBs will also be applicable to MIBs. CuS not only has good conductivity and a sufficient Mg^{2+} intercalation gap, but also has weak Mg-S bond interactions, which can improve the electrochemical reaction kinetics. In addition, the high mobility of Cu^{2+} can enhance the conversion reaction with Mg^{2+} and improve the reaction reversibility. Wang et al. developed a new 2D $\text{CuS}_{1-x}\text{Se}_x$ nanosheet cathode and observed an improved electrochemical performance by adjusting the chemical composition of anions, with an outstanding reversible capacity and cycling stability. Phase control in transition metal dihalides is considered to be an effective way to tune their chemical and electronic properties.^[337] Wang et al. synthesized Cu_xS nanosheets with tunable phases by a microwave-assisted strategy, in which $\text{Cu}_{1.7}\text{S}$ exhibited a large reversible capacity of 150.3 mAh g^{-1} at 50 mA g^{-1} , as well as an excellent rate capacity and long-term cyclability.^[338] At high temperatures (over $100 \text{ }^{\circ}\text{C}$), CuS was found to reach a high storage capacity, but the low-temperature electrochemical performance still needs to be greatly improved.^[339] Huang et al. developed CuS microspheres self-assembled from nanosheets at room temperature.^[340] Benefiting from the unique structural configuration and uniform size of CuS, the electrode delivered a high reversible capacity of 252 mAh g^{-1} at 100 mA g^{-1} and good rate capability with 91.7 mAh g^{-1} specific capacity at 1000 mA g^{-1} . Furthermore, 65.4% of the capacity was retained at 1 A g^{-1} after 500 cycles. In addition, the high charge-to-radius ratio of Mg^{2+} leads to strong interactions between the

ions and the host, which puts forward higher requirements for cathode materials. In 2018, Xiong and co-workers reported the high magnesium storage capacity (over 300 mAh g^{-1}) of CuS with $\text{Mg}(\text{ClO}_4)_2$ in an acetonitrile electrolyte at room temperature.^[341] Recently, Wang et al. combined the advantages of CuS nanosheets and 2D rGO matrices to construct a CuS@rGO cathode material, which exhibited a capacity of 421 mAh g^{-1} at a current density of 50 mA g^{-1} , significantly higher than those of the CuS and 2D rGO counterparts.^[342] To improve the reaction kinetics, Shen et al. prepared CuS microflowers composed of 2D nanosheets as the cathode material and used a fluorinated borate-based magnesium salt as the noncorrosive electrolyte.^[343] As displayed in **Figure 19a**, the addition of CTAB increased the interlayer spacing of CuS from 0.82 to 1.3 nm. Due to the advantages mentioned above and improved conductivity, the cathode showed a better electrochemical performance than bared CuS, exhibiting a high capacity up to 477 mAh g^{-1} at current density of 50 mA g^{-1} and an impressive gravimetric energy density of 415 Wh kg^{-1} , and retaining 99.96% of the discharge capacity after 1000 cycles.

As transition metal selenides possess "softer" anion lattices than oxides and sulfides, Se^{2-} seems to be favorable for the construction of the cathode mainframe.^[23] Cu_{2-x}Se and CuSe exhibit high ionic conductivity, abundant vacancies for Mg^{2+} insertion, and strong coordination between the Se^{2-} anions and Mg^{2+} cations. Therefore, Cu_{2-x}Se and CuSe are regarded as promising cathode materials with a high reversible specific capacity. For instance, Chen and co-workers confirmed that starfish-like Cu_{2-x}Se with a hierarchical structure assembled by nanosheets held a huge potential to enhance the solid-state Mg^{2+} diffusion kinetics, with a reversible capacity of 210 mAh g^{-1} at 100 mA g^{-1} with outstanding rate capability.^[344] To further explore the magnesium storage behavior of Cu_{2-x}Se , Xue et al. carried out various ex situ characterizations,^[345] and concluded that the reversible magnesium storage behavior of Cu_{2-x}Se was based on the ion replacement mechanism, that is, the copper ions in the Se^{2-} sublattice were replaced and squeezed by Mg^{2+} without causing the collapse of Se^{2-} sublattice structure. The Cu_{2-x}Se cathode delivered a high reversible capacity of 222 mAh g^{-1} at 100 mA g^{-1} , and an excellent rate capability of 155 mAh g^{-1} at 1000 mA g^{-1} . However, the pulverization of active materials triggered by crystallographic transformations may lead to a poor cyclic performance. To address this issue, Zhang et al. used microwave irradiation to prepare CuSe nanosheets with preferential orientation (110) active planes through a temperature-controlled crystal growth path.^[346] Because the CuSe phase of hexagonal klockmann rock exhibited a layered crystal structure along the *c*-axis, it provided an internal driving force for nucleation and 2D anisotropic growth. It is worth noting that the preferred direction of crystal plane growth was related to the selenium source temperature, and at increasing temperature, the preferred orientation of CuSe nanosheets was along the (110) planes. From **Figure 19b**, at $120 \text{ }^{\circ}\text{C}$, the synthesized sample exhibited the highest (110) plane fraction at 67.4%. Additionally, the preferentially oriented CuSe (110) nanoflakes displayed a high specific capacity of 204 mAh g^{-1} at 200 mA g^{-1} (**Figure 19c**), an excellent rate capability and a long-term cycling stability over 700 cycles. This finding demonstrates that crystal engineering of electrode materials is an

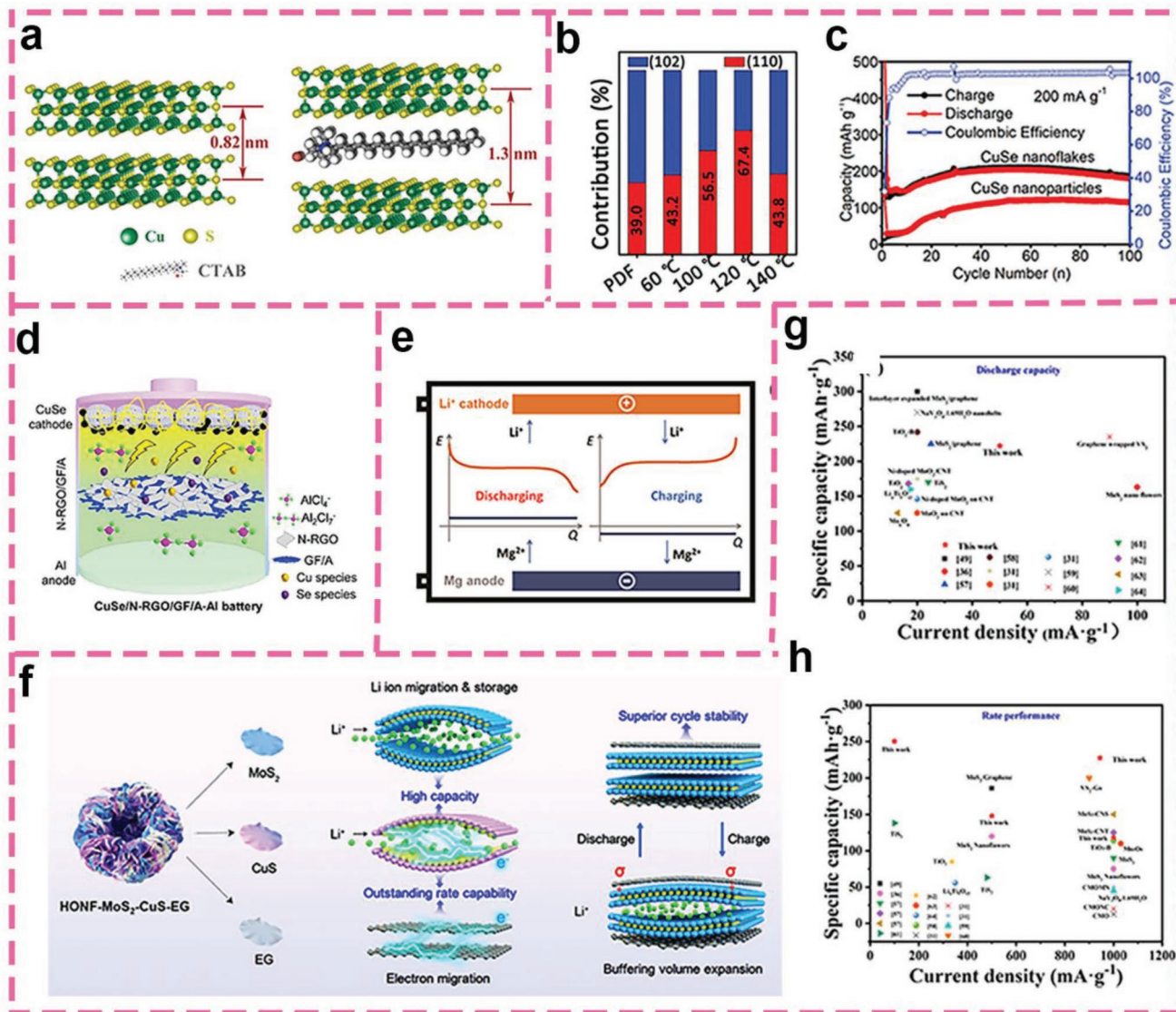


Figure 19. a) Structural schematic of the as-prepared CuS and CuS-CTAB-2 materials. b) Diffraction peak intensity of (102) and (110) planes under different temperatures. c) Short-term cycling properties of (110) preferentially oriented CuSe nanoflakes and CuSe nanoparticles. d) Schematic and electrochemical performance of the proposed CuSe/N-RGO/GF/A-Al battery. e) Schematic illustration of the working mechanism of a hybrid MLIB. f) Schematic illustration showing electrochemical mechanism of HONF-MoS₂-CuS-EG electrode in MLIBs. g) Comparison of Discharge capacities. h) Rate performance. a) Reproduced with permission.^[343] Copyright 2020, Wiley-VCH. b,c) Reproduced with permission.^[346] Copyright 2020, Wiley-VCH. d) Reproduced with permission.^[351] Copyright 2020, Elsevier. e) Reproduced with permission.^[353] Copyright 2015, American Chemical Society. f-h) Reproduced with permission.^[357] Copyright 2020, Elsevier.

effective technical strategy for improving the inherent activity of batteries.

The amphoteric aluminum anode relies on three-electron transfer in a single redox reaction, which provides the opportunity to store and increase charge compared to LIBs or SIBs, and thus has a higher theoretical specific capacities (gravimetric density 2981 mAh g⁻¹, volumetric density 8065 mAh cm⁻³) and comparatively low redox potential at 1.76 V (vs SHE).^[347] The feasibility of copper-based as electrode materials has been testified in AIBs.^[348] Despite these advantages, the large size of solvated Al³⁺ in electrolyte and its strong adhesion to the host material seriously hinder the development of AIBs.

In a previous study, 3D hierarchical nanostructured CuS microspheres composed of 2D nanoflakes were produced solvothermally and used as an AIB cathode in the voltage range of 0.1–2.0 V.^[349] In this composite structure, the acetylene black nanoparticles were uniformly dispersed on the surface of CuS@C microspheres, which dramatically boosted the charge transfer, leading to an initial discharge capacity of 240 mAh g⁻¹ with 90 mAh g⁻¹ at 20 mA g⁻¹ after 100 cycles. In another study, Cu₃P/C composites were produced by a high-energy ball milling method, and applied as an AIB cathode for the first time, which displayed a significantly enhanced cyclic stability.^[350] A new coordination adsorption strategy was proposed to capture dissolved active substances by N-doped RGO functional battery

separator. Li et al. prepared a CuSe-positive electrode material for AIBs (Figure 19d).^[351] where the coordination interaction between N-RGO and soluble species inhibited the diffusion of active species into the electrolyte, restored the vitality of active species adsorbed in N-RGO and reduced polarization, and hence promoted the kinetics of electron transfer and electrolyte ion diffusion. As a result, a high initial discharge capacity of 4577 mAh g⁻¹ was achieved at 500 mA g⁻¹ and a discharge capacity of 216 mAh g⁻¹ after 500 cycles.

6.5. Hybrid Mg/Li-Ion Batteries

MLIBs possess the merits of rapid alkali metal ion insertion cathode, dendritic-free Mg anode, fast diffusion kinetics, excellent safety, and high electrochemical performance.^[352] It has been proved to be a promising safe energy storage system at room temperature. Li⁺ replaces Mg²⁺ to dominate the cathode reaction, because the diffusion rate of Li⁺ in the same matrix material is several orders of magnitude faster than that of Mg²⁺. As the redox potential of Mg²⁺/Mg is 0.67 V higher than that of Li⁺/Li, reversible Mg deposition/dissolution occurs on the anode side, before Li deposition/dissolution.^[353]

The Mg²⁺/Li⁺ mixed electrolyte provides sufficient Li⁺ for cathodic electrochemical reaction and kinetics, especially when there is no Li⁺ in the cathode materials. At present, the Mg²⁺/Li⁺ mixed electrolyte is composed of LiCl and AlCl₃-C₆H₅ClMg (APC). The LiCl additive not only improves the electrochemical performance, but also prevents the formation of passive films on the magnesium anode.^[354] The working mechanism of MLIBs is shown in Figure 19e.^[353] Yuan reported the outstanding electrochemical performance of Mg²⁺/Li⁺ hybrid batteries consisting of a Cu₂Se non-insertion-based cathode of different morphologies, a magnesium anode, and an electrolyte consisting of 0.4 mol dm⁻³ APC and 1.0 mol L⁻¹ LiCl in tetrahydrofuran.^[355] A highly synergetic interaction between Li⁺ and Mg²⁺ ions toward the displacement reaction was proposed. The hybrid batteries showed a superior rate performance with 239.7 mAh g⁻¹ at 0.1 C but poor cycling performance. Zhang et al. explored the electrochemical performance and reaction mechanism of copper sulfide/multiwalled carbon nanotube films as a cathode in a hybrid Mg²⁺/Li⁺ battery with a APC-LiCl hybrid electrolyte.^[356] In general, due to the strong polarization effect of Mg²⁺ and diffusion dynamics of Li⁺, use of a single copper-based material as the electrode cannot inhibit the electrode volume expansion, leading to a disappointing charge–discharge cycle performance. Hou et al. used MoS₂-CuS-EG nanoflowers composed of impressively anisotropic thin nanosheets as an cathode material for MILBs for the first time.^[357] The advantages of this material were (Figure 19f): 1) MoS₂ and CuS facilitated the storage of Li⁺, accelerated electron transfer and realized high capacity, and 2) EG not only improved the conductivity and the rate performance, but also effectively buffered the volume expansion/contraction and prolonged the cycle life. Consequently, the rationally designed MILBs could deliver a high reversible discharge capacity of 222 mAh g⁻¹ at 50 mA g⁻¹ and excellent rate performance with a discharge capacity of 201.4 and 117.5 mAh g⁻¹ at 200 and 1000 mA g⁻¹ with a capacity of 172.4 mAh g⁻¹ after 100 cycles (Figure 19g,h).

6.6. Summary

In this section, the recent progress of the use of 2D copper-based nanostructures as electrode materials in rechargeable batteries is critically summarized. It should be noted that, compared with the bulk materials, the 2D copper-based nanostructures usually exhibit enhanced interactions at the interfaces with electrolytes and dynamics of in-plane ion transport and carrier transport. In addition, the special 2D characteristics can inhibit or slow down the volume expansion generated in the charge–discharge cycle to a certain extent. The large specific surface area of the 2D nanostructures is also conducive to access to the active sites, facilitates charge distribution, and accelerates insertion extraction and redox reaction rates. Detailed electrochemical data for current reported anodes for rechargeable batteries are provided in Table 3.

Despite the substantial progress, a number of challenges remain. Compared with common transition metal materials, for example, in battery applications, 2D copper-based materials have significant volume expansion, weak electronic conductivity, and relatively low ion diffusion dynamics, which will lead to serious mechanical strain and insufficient cycling performance. In addition, the mechanism of ion transfer dynamics and charge storage of copper-based materials in various devices (especially MVIBs) are not fully understood. Furthermore, the high charge density of Mg²⁺, Al³⁺ and Mg²⁺/Li⁺ makes it difficult to reversibly insert/extract into the host materials. Except for CuS and a few Cu₃P, the study of other copper-based materials in rechargeable batteries has been limited, and most of them exist only in theory. Therefore, a better understanding of the reaction mechanism plays a vital role in optimizing the performance of the materials. With the continuous in depth exploration, 2D copper-based materials are expected to find wider applications in advanced rechargeable energy storage devices because of their unique structural characteristics, inherent environmental friendliness, and low price.

7. 2D Copper-Based Materials for Electrocatalysis

Electrocatalysis is a special form of catalysis to accelerate the charge transfer between the electrode and electrolyte interface.^[359] 2D nanosheets with a low coordination number and high fraction of surface atoms have been found to exhibit enhanced electrocatalytic activity, as compared to the bulk form, due to an increasing number of catalytic active centers for the adsorption of key reaction intermediates.^[360–362] The nanosheet morphology can shorten the charge transfer distance from the interior to the crystal surface, thus promoting charge separation, as well as facilitating mass transport of reaction species and electrolyte ions. Among these, copper-based materials have been attracting particular interest, as they have found diverse applications in, for instance, metal–air batteries, water splitting, and CO₂RR (Figure 20).^[363–365] Carrier separation and transfer kinetics are generally considered to be the most important issues for improving catalytic performance,^[366] which may be closely related to the structure activity of the catalyst. For all catalytic reaction systems, the electronic state determines the separation and transport of electric carriers, which will have a

Table 3. Properties, characteristics, and performance of 2D copper-based materials and hybrids for rechargeable batteries.

Electrode	Structure/ morphology	Method	Battery type	Specific capacity (current density)	Cyclic stability (cycles, current density)	Rate capability	Refs.
CuO	Nanosheet	Wet-chemical	LIB	500 mAh g ⁻¹ (0.2 C)	58% (500, 0.5 C)	35% from 0.2 to 2 C	[113]
CuO	Nanoflake	Electrochemical oxidation	LIB	529.3 mAh g ⁻¹ (0.5 A g ⁻¹)	60% (400, 2 A g ⁻¹)	61.6% from 0.5 to 2 A g ⁻¹	[256]
CuO	Nanoplate	Hydrothermal	LIB	354.4 mAh g ⁻¹ (1 C)	78.8% (70, 1 C)	53.8% from 1 to 4 C	[259]
CuO	Nanoplate	Hydrothermal	LIB	878.4 mAh g ⁻¹ (0.5 C)	70.2% (50, 0.5 C)	38.9% from 0.5 to 4 C	[260]
CuO	Nanoflake	Dealloying	LIB	1343.5 mAh g ⁻¹ (0.3 C)	100% (120, 0.3 C)	11.7% from 0.3 to 10 C	[261]
CuO	Leaf-like	Anneal	LIB	948 mAh g ⁻¹ (0.5 A g ⁻¹)	95.5% (200, 0.5 A g ⁻¹)	–	[263]
Cu _x Co _{3-x} O ₄	Nanosheet	Hydrothermal	LIB	1300 mAh g ⁻¹ (0.3 A g ⁻¹)	85% (50, 0.4 A g ⁻¹)	29.5% from 0.1 to 50 C	[264]
CuCo ₂ O ₄	Nanosheet	Solvothermal	LIB	1236 mAh g ⁻¹ (0.5 A g ⁻¹)	121.6% (600, 2 A g ⁻¹)	64.4% from 0.1 to 5 A g ⁻¹	[266]
CuS	Nanosheet	Wet chemical	LIB	396 mAh g ⁻¹ (0.2 A g ⁻¹)	162% (360, 0.2 A g ⁻¹)	50% from 0.2 to 3 A g ⁻¹	[269]
CuS/graphene	Nanoplate	Hydrothermal	LIB	1255 mAh g ⁻¹ (0.1 A g ⁻¹)	–	29.8% from 0.1 to 5 A g ⁻¹	[271]
CuS@S	Nanosheet	Lime-sulfur synthetic	LIB	862.5 mAh g ⁻¹ (0.1 A g ⁻¹)	78.0% (1000, 1 A g ⁻¹)	40.0% from 0.1 to 2 A g ⁻¹	[273]
Cu ₃ P	Membrane	Chemical vapor deposition	LIB	419 mAh g ⁻¹ (0.2 C)	59.7% (20, 0.2 C)	–	[283]
Cu ₃ P@C	Nanosheet	Heat treatment	LIB	540 mAh g ⁻¹ (37 mA g ⁻¹)	70.6% (150, 37 mA g ⁻¹)	18.7% from 37 to 5920 mA g ⁻¹	[289]
Si@Cu ₃ (HITP) ₂	Nanosheet	Heat treatment	LIB	2511 mAh g ⁻¹ (0.1 C)	98.9% (100, 0.1 C)	31% from 5 to 20 C	[296]
CuO	Nanoflake	Hydrothermal	SIB	600 mAh g ⁻¹ (0.025 A g ⁻¹)	73% (150, 1 A g ⁻¹)	32.7% from 0.025 to 2 A g ⁻¹	[309]
CuS	Nanodisk	Vacuum filtration	SIB	610 mAh g ⁻¹ (0.1 A g ⁻¹)	75% (500, 1 A g ⁻¹)	51.6% from 0.1 to 3 A g ⁻¹	[312]
CuSe	Nanosheet	Chemical precipitation	SIB	295 mAh g ⁻¹ (10 A g ⁻¹)	95.6% (1200, 5 A g ⁻¹)	74.7% from 0.1 to 5 A g ⁻¹	[316]
CuSe	Nanosheet	Hydrothermal	SIB	404 mAh g ⁻¹ (0.1 A g ⁻¹)	100% (500, 0.5 A g ⁻¹)	78.6% from 0.05 to 20 A g ⁻¹	[317]
CuS@CuSe	Core-shell	Sulfidation/ selenization	SIB	450 mAh g ⁻¹ (2 A g ⁻¹)	86.2% (1400, 20 A g ⁻¹)	68% from 0.2 to 20 A g ⁻¹	[358]
MoS ₂ /Cu ₂ Se	Nanosheet	Hydrothermal	SIB	139 mAh g ⁻¹ (100 A g ⁻¹)	100% (1,4000, 0.5 A g ⁻¹)	34.8% from 0.1 to 100 A g ⁻¹	[314]
Cu ₂ Se-CTAB	Nanosheet	Room temperature reaction	SIB	432.8 mAh g ⁻¹ (0.1 A g ⁻¹)	90% (6500, 20 A g ⁻¹)	55.9% from 0.1 to 30 A g ⁻¹	[305]
Cu ₃ P@C	Nanosheet	Epitaxial phosphidation	SIB	340.7 mAh g ⁻¹ (0.1 A g ⁻¹)	68.0% (1000, 1 A g ⁻¹)	33.0% from 0.1 to 10 A g ⁻¹	[321]
CuO	Nanoplate	Hydrothermal	PIB	342.5 mAh g ⁻¹ (0.2 A g ⁻¹)	78.4% (100, 1 A g ⁻¹)	46.3% from 0.2 to 2 A g ⁻¹	[330]
CuS-C@Nb ₂ O ₅	Core-shell	Electrospinning	PIB	259.2 mAh g ⁻¹ (0.1 A g ⁻¹)	93.7% (2000, 2 A g ⁻¹)	33.4% from 0.1 to 2 A g ⁻¹	[333]
CuSe	Nanosheet	Chemical precipitation	PIB	280 mAh g ⁻¹ (5 A g ⁻¹)	92.6% (100, 2 A g ⁻¹)	80.0% from 0.2 to 5 A g ⁻¹	[316]
CuS _{0.8} Se _{0.2}	Nanoplate	Hydrothermal	PIB	401 mAh g ⁻¹ (0.2 A g ⁻¹)	96.0% (600, 2 A g ⁻¹)	82.2% from 0.1 to 1 A g ⁻¹	[332]
CuS _{1-x} Se _x	Nanosheet	Microwave	MIB	268.5 mAh g ⁻¹ (0.02 A g ⁻¹)	100% (100, 0.3 A g ⁻¹)	44% from 0.02 to 0.5 A g ⁻¹	[337]
Cu _{1.7} S	Nanosheet	Microwave	MIB	153 mAh g ⁻¹ (0.3 A g ⁻¹)	103.4% (50, 0.1 A g ⁻¹)	71.8% from 0.3 to 0.5 A g ⁻¹	[338]
CuS	Nanosheet	Microwave	MIB	300 mAh g ⁻¹ (0.02 A g ⁻¹)	120% (200, 0.2 A g ⁻¹)	92.6% from 0.05 to 0.1 A g ⁻¹	[339]
CuS@rGO	Nanosheet	Chemical synthesis	MIB	421 mAh g ⁻¹ (0.05 A g ⁻¹)	39.6% (500, 1 A g ⁻¹)	73.9% from 0.05 to 0.5 A g ⁻¹	[342]
Cu _{2-x} Se	Nanosheet	Hydrothermal	MIB	210 mAh g ⁻¹ (0.1 A g ⁻¹)	65% (300, 0.2 A g ⁻¹)	47.6% from 0.1 to 1 A g ⁻¹	[344]
Cu _{2-x} Se	Nanoplate	Solvothermal	MIB	222 mAh g ⁻¹ (0.1 A g ⁻¹)	84.3% (500, 1 A g ⁻¹)	72.4% from 0.1 to 1 A g ⁻¹	[345]
CuSe	Nanoflake	Microwave	MIB	204 mAh g ⁻¹ (0.2 A g ⁻¹)	99.9% (900, 1 A g ⁻¹)	21.6% from 0.05 to 2 A g ⁻¹	[346]
CuS@C	Microsphere	Solvothermal	AIB	90 mAh g ⁻¹ (0.02 A g ⁻¹)	37.5% (100, 0.02 A g ⁻¹)	–	[349]
Cu ₂ Se	Nanoplate	Solvothermal	MLIB	120 mAh g ⁻¹ (0.2 C)	64.2% (20, 0.1 C)	57.1% from 0.02 to 0.2 C	[355]
CuS-CNT	Film	Vacuum filtration	MLIB	525 mAh g ⁻¹ (0.01 A g ⁻¹)	50.0% (100, 0.03 A g ⁻¹)	55.0% from 0.01 to 0.1 A g ⁻¹	[356]
MoS ₂ -CuS	Nanoflower	Hydrothermal	MLIB	240.6 mAh g ⁻¹ (0.05 A g ⁻¹)	91.6% (150, 0.5 A g ⁻¹)	83.6% from 0.1 to 1 A g ⁻¹	[357]

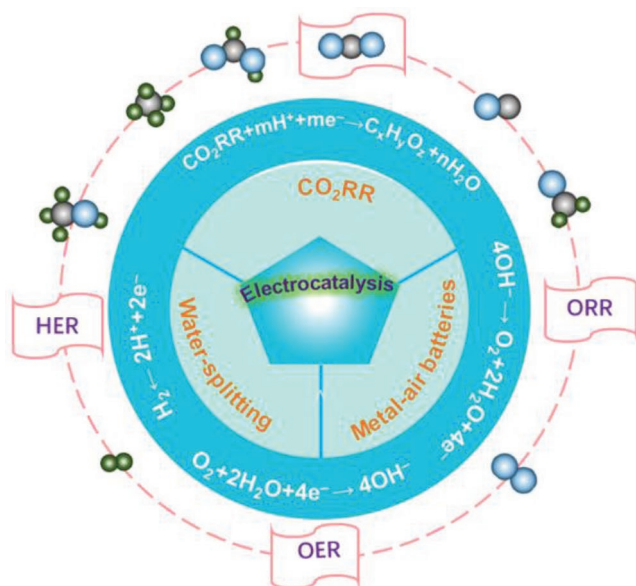
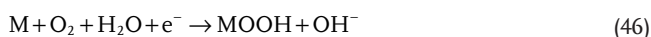


Figure 20. Schematic illustration of 2D Copper-based materials for electrocatalysis application.

great impact on the actual catalytic performance.^[367] In brief, the catalytic performance of 2D layered nanocatalyst is related to the number of reaction sites, surface/interface characteristics, electronic properties and energy band structure of the catalyst, where they are correlative instead of independent of each other; as a result, they are always conditioned together.^[368] The crucial structural and electronic parameters as well as the crystallographic details of the copper-based materials are summarized in **Table 4**.

7.1. Mechanistic Insights

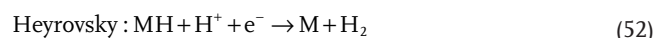
The process of electrocatalytic reaction is usually the diffusion and adsorption of reactants on the catalyst surface, and the transmission of electrons to the catalyst surface. Then the adsorbed reactants capture electrons to form some intermediates, and then further convert them into the required products. The final products desorb from the catalyst surface and diffuse into the electrolyte.^[377] The heart of water splitting, and metal–air batteries depends on a series of electrochemical processes, namely, ORR, OER, and HER.^[377] The reaction pathway of ORR is shown in **Figure 21a**.^[117] ORR is a complex reaction, where O₂ can be reduced to hydrogen peroxide or water by the 2e⁻ or 4e⁻ route,^[378,379] and the latter is preferred for high-efficiency fuel cell. In alkaline media, ORR usually involves the following steps:



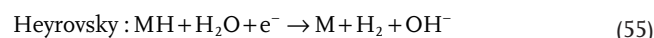
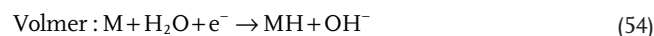
Among them, the active sites on the catalyst surface are represented by M. The adsorption of intermediates, such as MOOH, M–O, M–OH, has an important impact on the ORR kinetics. The whole process of adsorption and dissociation of water to protons involves four processes. As shown in **Figure 21b**, the steps of OER are just opposite to those of ORR.

HER is a two-electron transfer process, involving multistep reactions including adsorption, reduction, and desorption (**Figure 21c,d**). In both acidic and alkaline media, reactants (e.g., H⁺ or H₂O) are adsorbed onto the electrode surface by proton and electron transfer (Volmer reaction).^[380] Unlike in acidic electrolyte, there is one more step of water dissociation in alkaline electrolytes. Then, the adsorbed hydrogen may be combined to produce molecular hydrogen through the electrochemical Heyrovsky reaction or chemical Tafel reaction. The key reaction steps are outlined in the following reaction pathways:^[381]

In acidic media,



In neutral and alkaline media,



CO₂RR entails several key steps. First, CO₂ molecules are chemically adsorbed onto the catalytic active center, then electron/proton transfer occurs to crack the C–O bond and form C–H bond, and finally the product is desorbed from the catalyst surface, as described in **Figure 21e**.^[382,383]

7.2. Applications

7.2.1. Metal–Air Batteries

The theoretical energy density of Li–air and Zn–air batteries are up to 3500 and 1370 Wh kg⁻¹, respectively, which are higher than those of the most advanced LIBs (<200 Wh kg⁻¹).^[384,385] Li–air batteries work similarly to Zn–air batteries. They are based on a metal redox reaction between a metal electrode and oxygen at an air electrode. In addition to the metal redox reactions, electrocatalyst-assisted oxygen reactions consisting of ORR in discharge process and OER in charge process are

Table 4. Structural and electronic parameters as well as the crystallography of copper-based materials.

Material	Crystal system	Bandgap	Semiconductor characteristic	Lattice constant	Refs.
Cu ₂ O	Cubic	2.1 eV	p-type	<i>a</i> = 4.27 Å	[369]
CuO	Monoclinic	1.4 eV	p-type	<i>a</i> = 4.68 Å	[370]
Cu ₂ S	Cubic	1.2 eV	p-type	<i>a</i> = 12.04 Å	[27,371]
CuS	Hexagonal	2.1 eV	p-type	<i>a</i> = 3.82 Å	[372]
Cu ₂ Se	Monoclinic	2.2 eV	p-type	<i>a</i> = 7.14 Å	[373]
CuSe	Hexagonal	1.57 eV	p-type	<i>a</i> = 3.94 Å	[374]
CuCo ₂ O ₄	Cubic	1.5 eV	p-type	<i>a</i> = 8.105 Å	[375]
Cu ₃ N	Cubic	2.0 eV	p-type	<i>a</i> = 3.82 Å	[48]
Cu ₃ P	Hexagonal	1.55 eV	p-type	<i>a</i> = 6.959 Å	[376]

critical to the overall efficiency.^[386] 2D copper-based materials have been found to exhibit apparent activity towards ORR and OER.^[387–389] For instance, CuCo₂O₄ in a spinel-like structure is a candidate catalyst with great promise due to the synergy between Cu and Co.^[390,391] Introduction of porous structures into the catalyst is an effective strategy to further enhance their performance.^[392] Niu et al. improved the bifunctional activity of hierarchical CuCo₂O₄ microflowers constructed by porous 2D nanosheets.^[393] A series of characterizations showed that the average thickness of the nanosheet was about 20 nm with the pore sizes between 20 and 50 nm and the surface area 94.1 m² g⁻¹, which allowed rapid diffusion of electrolyte/oxygen into the interior and effectively accessed the active sites. A Li–air battery based on this electrocatalyst revealed a much higher stability of 120 cycles as compared to highly aggregated CuCo₂O₄. In situ growth of catalysts on a carbon substrate has shown similar positive effects. The specific capacity of a Li–air battery assembled by ultrathin mesoporous CuCo₂O₄ nanosheets was 11793 mAh g⁻¹ at 200 mA g⁻¹ and discharging/charging voltage gap of 0.95 V.^[394] This was because the CuCo₂O₄ grown in this way significantly reduced the interfacial impedance, prevented the oxidation of the catalyst, made uniform adhesion of the catalyst, and possessed good electrical conductivity and a large specific surface area. Compared with CuCo₂O₄, CuCo₂S₄ possesses an even higher conductivity and multiple valences, leading to a superior electrocatalytic activity. Zhao et al. showed that 2D CuCo₂S₄ nanosheets exhibited a good performance towards ORR, with a half-wave potential (*E*_{1/2}) of +0.74 V,^[395] and for OER, the overpotential ($\eta_{\text{OER},10}$) was just +0.337 V to reach the current density of 10 mA cm⁻² and the onset potential was +1.5 V. The outstanding bifunctional catalysis arose from the exposure of two peculiar planes (022) and (004), which were distinctly preferred in ORR and OER. The improvement of its performance can be attributed to the excellent spinel structure of CuCo₂S₄, in which both Cu and Co showed rich redox properties, creating an enough space to accommodate discharge products, ulteriorly facilitating the ORR and OER kinetics. Hou et al. concluded that bifunctional catalytic activity of the electrocatalyst was ascribed to the exposure of the (113) and (004) planes affording enough active sites and facilitating catalytic reactions.^[396] Recently, Long and co-workers synthesized a novel freestanding CuCo₂S₄@Ni nanosheet array by a hydrothermal method and investigated their catalytic activities as an oxygen electrode (Figure 22a).^[397] As shown in Figure 22b, these

nanosheet arrays were approximately 50 nm thick and evenly interconnected with each other, forming numerous cavities with diameters ranging from 200 to 400 nm. When assembled into an aprotic Li–O₂ battery, it displayed a low overpotential of 0.82 V and high capacity of 9673 mAh g⁻¹ at 100 mA g⁻¹, with a high cyclability (Figure 22c).

2D CuCo₂S₄ nanomaterials have also been explored for Zn–air batteries. Li et al. utilized S vacancies to improve the catalytic performance of atomic-thick metal CuCo₂S₄ nanosheets with good conductivity. This increased the active site as well as specific surface area and improved the kinetic process.^[398] The catalyst exhibited a low $\eta_{\text{OER},10}$ of +287 mV and a very less onset potential of just 0.9 V for ORR. Meanwhile, with the nanosheets as the air cathode catalysts, the Zn–air battery delivered an energy density of 313 and 424 Wh kg⁻¹ at 0.5 and 1 mA cm⁻², respectively.

In practice, doping can further enhance the activity of the air electrode catalysts by the synergistic effect of enhanced electrical conductivity and increased nucleation sites.^[399] For instance, Pan et al. reported an improved performance of the oxygen electrode using nitrogen-doped carbon nanofibers modified with CuCo₂S₄ nanosheets (CuCo₂S₄ NSs@N-CNFs) (Figure 22d–f).^[400] Figure 22g summarizes the advantages of CuCo₂S₄ and N-CNFs as catalysts in the catalytic process. The CuCo₂S₄ NSs@N-CNFs showed a very good OER activity with $\eta_{\text{OER},10} = +315$ mV and a Tafel slope of 48 mV dec⁻¹ (Figure 22h); and the ORR activity was comparable to that of commercial Pt/C catalysts (Figure 22i,j). With CuCo₂S₄ NSs@N-CNFs as the air cathode catalyst in a Zn–air battery, the battery delivered a specific capacity as high as 896 mAh g⁻¹ at 25 mA cm⁻², a high open-circuit potential of 1.46 V, and ultralong cycling, a performance much better than the Zn–air battery based on commercial Pt/C and Ir/C catalysts. Zhang et al. prepared bimetallic CuCo₂S₄ nanosheets and observed an $\eta_{\text{OER},10}$ of 290 mV, due to the formation of S-doped CoOOH/CuO species on the catalyst surface during OER that was argued to be the actual catalytic active sites for OER.^[401]

7.2.2. Water Splitting

Water splitting is a unique technology to produce high-purity hydrogen, which consists of two half-reactions, HER and OER, at the cathode and anode, respectively.^[402] Notably, hydrogen

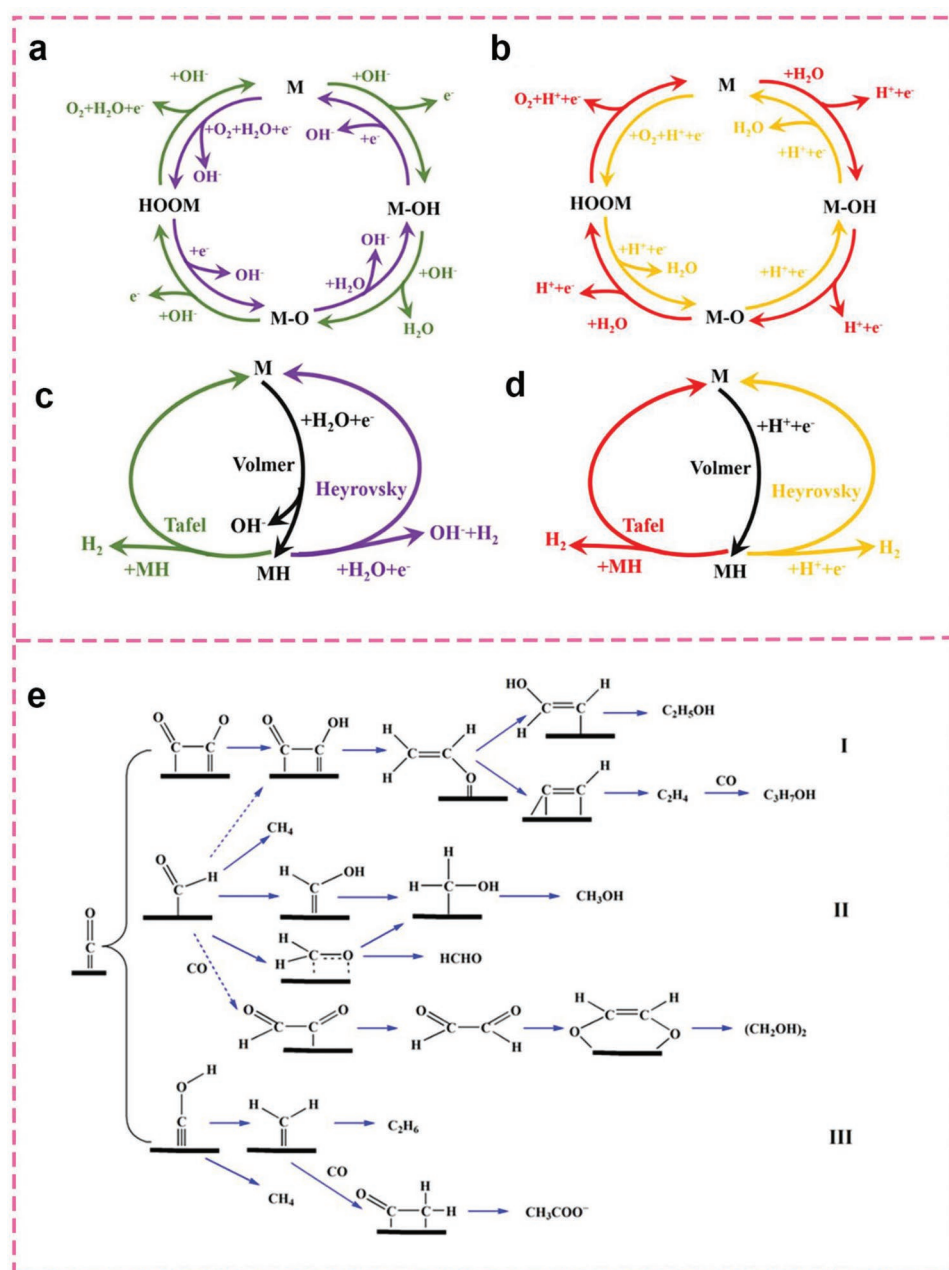


Figure 21. a) ORR (purple line) and OER (green line) mechanisms for alkaline condition. b) The ORR (orange line) and OER (red line) mechanisms for acidic condition. c) The HER mechanism for alkaline solution. d) The HER mechanism for acidic solution. e) Most likely reaction pathways from adsorbed *CO on Cu surface for C₁ and C₂ products. Plain red, plain blue, and dashed blue routes are for major, minor, and trace C₂ products. a–d) Reproduced with permission.^[17] Copyright 2020, Elsevier. e) Reproduced with permission.^[383] Copyright 2020, The Royal Society of Chemistry.

production from electrocatalytic water splitting is severely limited by the sluggish electron-transfer kinetics of OER at the anode, which demands a potential higher than 1.23 V.^[403] Therefore, efficient, stable, and environmentally friendly electrocatalysts are especially needed to reduce the energy barrier of water splitting. Previous studies have shown that Pt and its alloys are the most efficient HER catalysts because of their low overpotential requirements and high catalytic rate, but the applications are impeded by their high cost and low abundance.^[404] 2D copper-based materials with favorable

electronic properties and good durability are promising alternatives.^[405–408]

Although CuO has a lower activity for water splitting than other transition metals, it can be further improved by the formation of nanostructures, growth onto conductive scaffolds, and the synergistic effect of hybrid materials. Deng et al. argued that the metastable Cu^{II} oxides on the catalyst surface were the actual catalytic active sites for OER.^[409] Pawar et al. fabricated 2D CuO nanosheets onto a stainless steel substrate by CBD. The unique 2D morphology coupled with the optimized

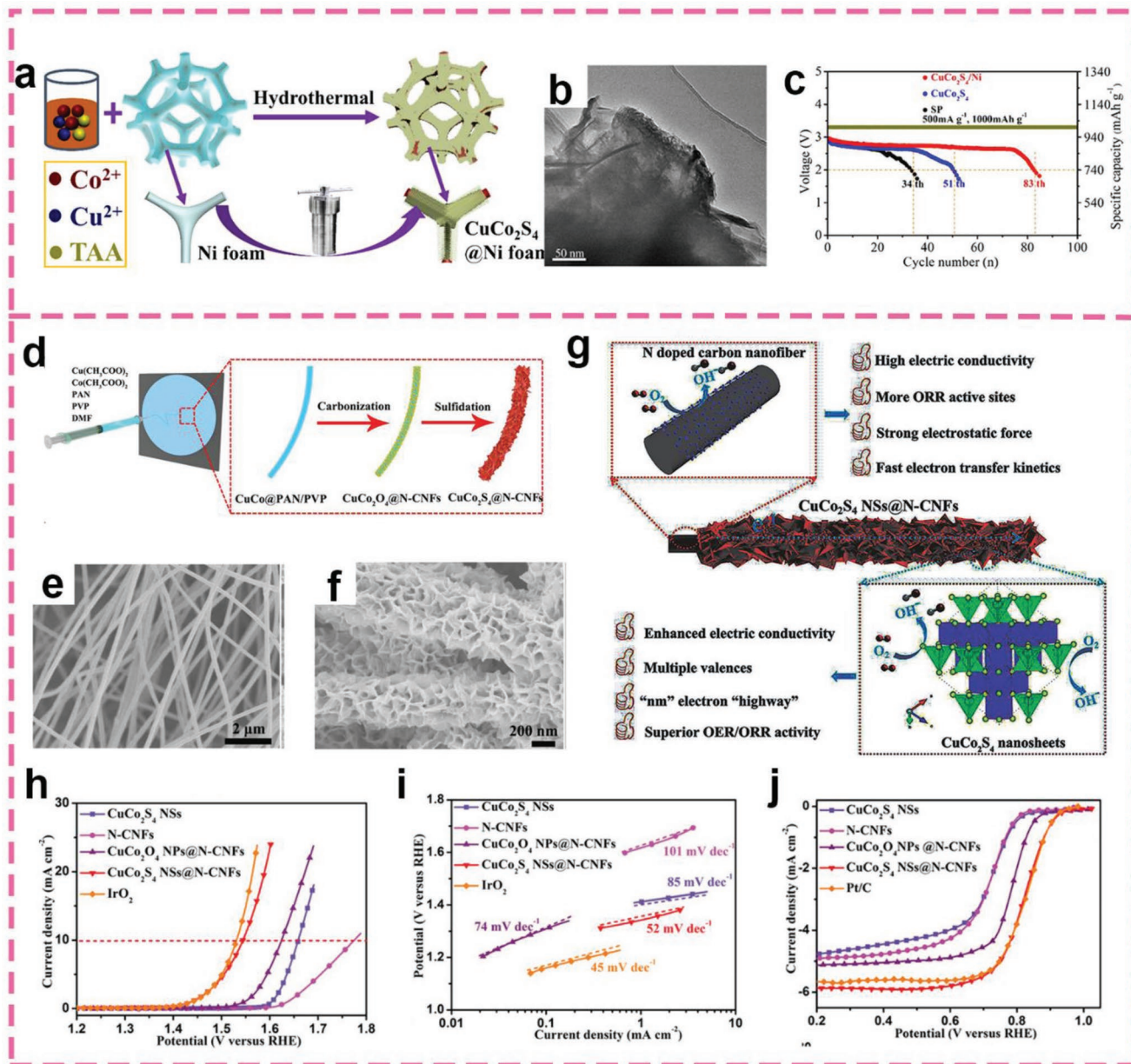


Figure 22. a) Schematic diagram of the fabrication of freestanding $\text{CuCo}_2\text{S}_4@Ni$ electrode. b) SEM images of $\text{CuCo}_2\text{S}_4@Ni$. c) Cyclability of $\text{Li}-\text{O}_2$ batteries at 500 mA g^{-1} with a cutoff capacity of 1000 mAh g^{-1} . d) Schematic diagram illustration of the preparation processes for the CuCo_2S_4 NSs@N-CNFs film. e) SEM images of the $\text{CuCo}@PAN/PVP$ nanofibers. f) CuCo_2S_4 NSs@N-CNFs. g) Illustration of the catalytic process of CuCo_2S_4 NSs@N-CNFs. h) OER polarization curves of the as-prepared five samples. i) The corresponding Tafel plots. j) ORR polarization curves of the as-prepared five samples. **a-c**) Reproduced with permission.^[397] Copyright 2019, American Chemical Society. **d-j**) Reproduced with permission.^[400] Copyright 2019, Wiley-VCH.

electronic properties after heat treatment played a key role in the OER activity, with an onset potential as low as 1.48 V and a Tafel slope of 59 mV dec^{-1} in 1 M KOH .^[410] With the trend of synthesizing cost-effective copper-based electrode to displace noble metal catalyst, how to do it at room temperature has become a great challenge. Recently, Liu et al. prepared Ni-modulated CuO nanosheet arrays by a room-temperature precipitation method, followed by in situ electro-oxidation (Figure 23a).^[411] It was noted that HCl played an indispensable role in the preparation process, which was conducive to the precipitation of Cu ions to

form the $\text{Ni}-\text{CuCl}$ precatalyst, and corrosion of NF surface to initiate the supply of Ni . As a result, the $\text{Ni}-\text{CuO}$ sample exhibited a low $\eta_{\text{OER},200}$ of $+367 \text{ mV}$ (Figure 23b). More significantly, when $\text{Ni}-\text{CuO}$ was assembled with $\text{Ni}-\text{CuO}-\text{S}$ into a two-electrode system, a low voltage of 1.55 V was needed to produce 10 mA cm^{-2} in water splitting, which the operation maintained continuous stability for over 30 h at 100% Faraday efficiency (FE). In conjunction with DFT calculations (Figure 23c–i), it was argued that Cu was the OER active site on $\text{Ni}-\text{CuO}$, and Ni doping increased the d-band center, leading to more delocalized

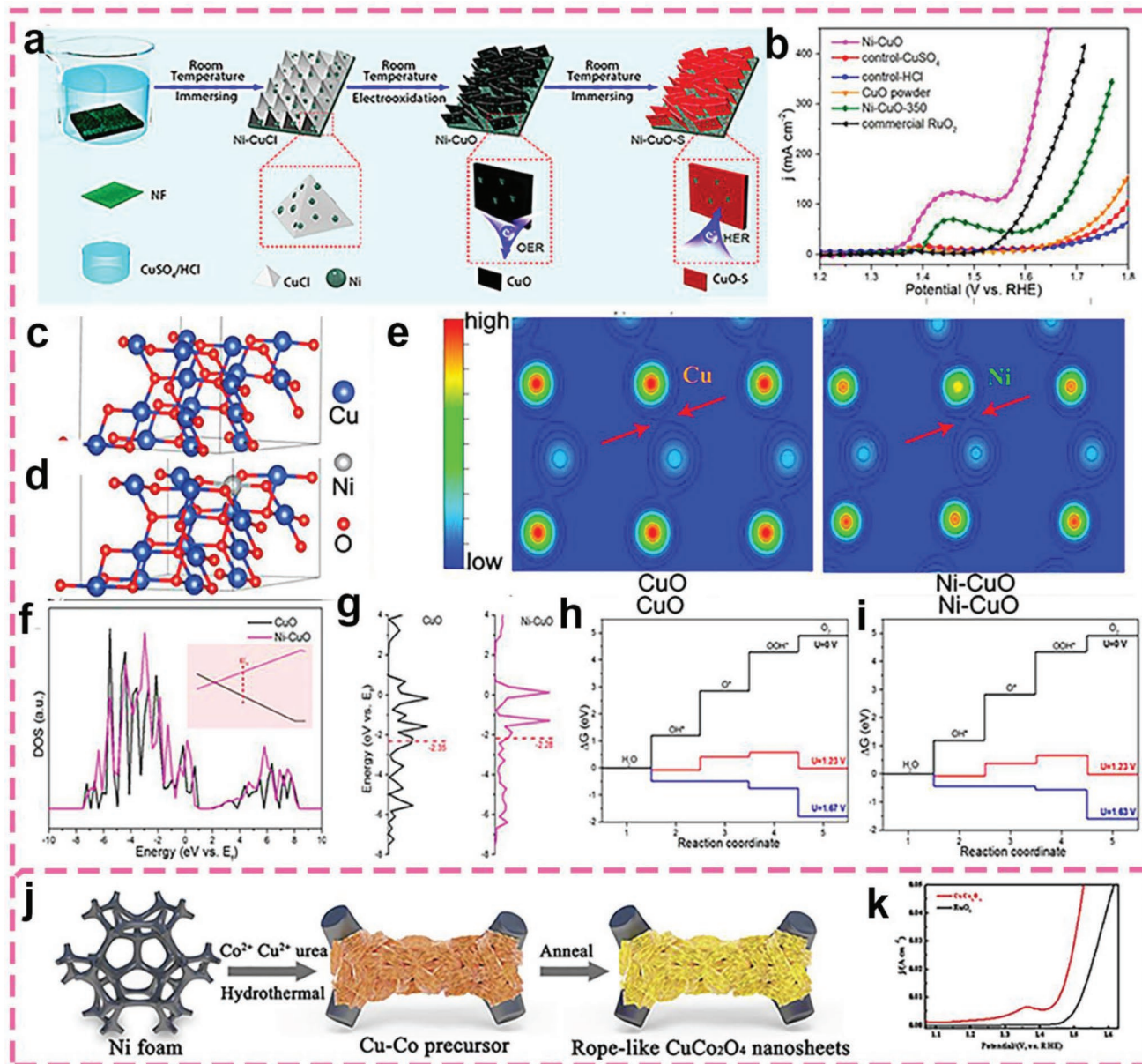


Figure 23. a) Schematic of experiment for synthesis of Ni-CuO and Ni-CuO-S. b) LSV curves for alkaline OER. c) DFT calculation results on (111) surface models: the optimized structures for CuO. d) Ni-CuO. e) Charge density distribution with black lines depicting the contour lines of the charge density. f) DOS, with the Fermi level set to 0 eV, with the magnification of states around the Fermi level inset in. g) Calculated projected DOS with d-band center highlighted for the active sites. h) Free energy change diagrams for OER over CuO. i) Ni-CuO. j) The schematic illustration of fabricating rope-like CuCo_2O_4 nanosheets directly on Ni foam. k) The iR-corrected polarization curves of the CuCo_2O_4 and RuO_2 electrodes. a–i) Reproduced with permission.^[411] Copyright 2019, American Chemical Society. j,k) Reproduced with permission.^[413] Copyright 2020, Elsevier.

electrons in CuO, higher carrier concentration, and O-bonding strength. CuCo_2O_4 is another important OER catalyst, and strategies are needed to improve the electrochemical performance. Ahmed et al. used various solvents to adjust the morphology of CuCo_2O_4 electrocatalysts for OER in KOH.^[62] With the increase of the viscosity of deionized water, ethanol, ethylene glycol, and glycerol, the growth rate limitation of the corresponding active substances increased. Therefore, a special morphological modification improved the effective surface area, which was instrumental in the electron transfer. The results showed that nanosheets prepared in deionized water showed excellent OER

properties, a low $\eta_{\text{OER},20}$ of 294 mV and a small Tafel slope of 117 mV dec^{-1} . The nanosheets were then used as the anode and cathode bifunctional catalyst for overall water splitting in alkaline media,^[412] displaying a full-cell voltage of 1.64 V to achieve a current density of 10 mA cm^{-2} . In 2020, Zhang and He engineered rope-like CuCo_2O_4 nanosheets (Figure 23j), which exhibited an excellent OER performance with a low $\eta_{\text{OER},10}$ of 220 mV and outstanding durability (Figure 23k).^[413] Kim's group prepared CuCo_2O_4 nanomaterials by controlling the annealing temperature, and at 250°C , the optimized sample attained a current density of 20 mA cm^{-2} at a low cell voltage

of only 1.6 V and exhibited prominent stability for 100 h at high pH. In general, 2D nanosheets can provide simple diffusion paths for ions and electrons, ready access to electrochemically active sites at the electrode–electrolyte interface, high electrical conductivity, and structural stability, leading to improved catalytic activity and durability in water splitting.^[83]

CuS is a p-type semiconductor material with significant anisotropic characteristics, which can effectively supply a permeable channel for the absorption and transport of ions.^[44] Meanwhile, it possesses an intense tendency to capture electrons and accelerate electron transfer reactions due to the empty 3p-orbitals in the sulfur atoms and a large number of cavities in the structure.^[45] Therefore, copper sulfide nanostructures may exhibit a fascinating electrochemical performance by controlling the morphology and electronic configuration, and formation of heterostructures with other materials. For instance, He's group prepared Cu₂S nanosheet via room-temperature and atmospheric pressure-active iodine dielectric barrier discharge plasma and anion exchange reaction, and observed an excellent OER performance, $\eta_{\text{OER},20}$ of 336 mV.^[46] Shi's group showed that graphdiyne/CuS heterostructures delivered a superior activity by requiring an $\eta_{\text{HER},10}$ of just 106 mV for HER because of the effective coating of graphdiyne with satisfactory electronic conductivity and unique layered structure.^[47]

2D MOFs can be another group of high-efficiency electrocatalysts due to its large specific surface area, fully exposed active centers, and facile interactions with reaction substrates.^[48] Rong's group prepared layered CuS@C electrocatalysts derived from sulfidation of 2D Cu-MOF.^[49] The hybrids possessed an excellent HER performance in 0.5 M H₂SO₄, with $\eta_{\text{HER},10} = 128$ mV and the Tafel slope 44 mV dec⁻¹. Owing to the protection of the carbon matrix, further optimization was possible and the catalyst exhibited excellent stability in acidic, alkaline, and neutral media. CoS₂ is a sulfide with high conductivity and excellent chemical properties.^[20] Li's group synthesized CoS₂/CuS heterostructures via integrating CuS nanosheets and CoS₂ nanoparticles for all-pH HER.^[21] The unique composite showed a large specific surface area, and the synergistic effects of 3%CoS₂/7%CuS led to more efficient catalysis and higher electrical conductivity than other catalysts (Figure 24a–c). Swathi and co-workers constructed CuS@b-SnS heterogeneous nanocrystalline materials, which showed good stability without degradation for over 16 h after continuous electrolysis operation for OER.^[22]

Another way to improve the catalytic activity is to modulate the atomic environment and electronic structure.^[23] Kundu et al. synthesized Ni-doped CuS nanocrystals and achieved an $\eta_{\text{OER},10}$ of 0.39 V. It was found that doping Ni atoms into CuS produced defects and cooperation with adjacent Cu atoms improved the activity, due to a change of the surface electronic environment.^[24] In fact, controlling defects, nanointerface and valence together is an effective route for the preparation of efficient OER catalysts. For instance, Fe_{sub}-CuS nanosheets were synthesized by a solvothermal method, which involved the redox process of Fe(III) and Cu(I).^[25] For OER, the catalyst delivered a relatively low overpotential and Tafel slope, in great contrast with bare CuS. As shown in Figure 24d,e, Fe_{sub}-CuS exhibited lower energy levels relative to pristine CuS and Fe–CuS, and the oxygen-binding energy of CuS on the Fe-doped surface was

higher than that of pure CuS. Moderate oxygen-binding energy on Fe_{sub}-CuS led to a high OER activity near the top of the volcano curve. The excellent properties were attributed to the following reasons. First, Fe_{sub}-CuS nanomaterials had strong atomic-level nanointerface and S-vacancy defects. Second, the local atomic structure of obtained samples was regulated by the valence regulation between Fe²⁺ and Fe³⁺. Finally, the introduction of partially oxidized Fe²⁺ on the surface of CuS was conducive to the catalytic performance. The electrocatalysts based on CuCo₂S₄ ternary sheet arrays for OER and HER produced a low Tafel slope of 43.8 and 55.4 mV dec⁻¹ with $\eta_{\text{OER},10}$ of 210 mV and $\eta_{\text{HER},10}$ of 60 mV, with a Tafel slope of 84 and 83 mV dec⁻¹, respectively, surpassing FeS₂/CoFe₂O₄, CuS/CuFeS₂.^[26] Liu et al. claimed that the [111] plane of spinel was more active in OER than other crystal planes because only octahedral coordinated cations were exposed.^[27] Deka et al. constructed 2D CuCo₂S₄ that were exposed primarily with the (111) facets by a hydrothermal method, demonstrating a low $\eta_{\text{OER},10}$ of 310 mV and small Tafel slope of 86 mV dec⁻¹ in 0.1 M KOH.^[28] Using a similar method, Hao et al. synthesized self-assembled CuCo₂S₄ nanomaterials for OER electrocatalysis in alkaline media.^[29] The CuCo₂S₄ nanosheets containing CTAB surfactant afforded an excellent activity with a small $\eta_{\text{OER},10}$ of 269 mV, a low Tafel slope of 41 mV dec⁻¹ and prominent stability. Tran et al. synthesized well-crystalline Cu₂MoS₄ nanosheets, which exhibited a structure similar to Cu₂WS₄.^[30] A moderate overpotential of 135 mV was needed to deliver an exchange current density of 0.040 mA cm⁻².

Because S and Se have similar electronegativity and the interaction between S and Se is strong enough, a simple new concept can be carefully designed to replace S with Se to produce defects or micro strains in the catalyst lattice. Motivated by this fact, Tiwari et al. synthesized a highly active and stable layered Cu₂MoS₄ electrocatalyst via a facile solution process to prepare Cu₂Mo(S_ySe_{1-y})₄, and the obtained sample was exfoliated to produce monolayers by ultrasonication treatment (Figure 24f).^[31] DFT studies of the optimized molecular structures and corresponding vibrational modes of pristine Cu₂MoS₄ and anion-substituted Cu₂Mo(S_ySe_{1-y})₄ (Figure 24g). It exhibited the highest electrocatalytic activity because more Mo and Cu metal centers became available, as compared to the multilayer and bulk forms, with a low $\eta_{\text{HER},10}$ of 170 mV and Tafel slope of 52 mV dec⁻¹ (Figure 24h). Similarly, single-layer Cu₂WS₄ played a key role in HER electrocatalysis,^[32] which was composed of covalently bonded transition metal atoms bridged by sulfur atoms, with van der Waals interaction between its layered structures (Figure 24i). To comprehend the effect of Se substitution on the electrocatalytic activity, the Gibbs free energy of adsorbed atomic hydrogen was calculated and the optimized molecular structure was shown in Figure 24j. Only Cu₂WS_{2.6}Se_{1.4} showed high activity, the low onset potential required at 10 mA cm⁻² was nearly -320 mV, which was twice lower than that of the previously pristine Cu₂WS₄, and the Tafel slope value was small and observed to be about 46 mV dec⁻¹ (Figure 24k,l). Wu et al. prepared 2D single-layer Cu₂WS₄ and observed an excellent electrocatalytic activity.^[33] In addition, the introduction of in-gap states and the movement of d-band center could further reduce its Gibbs free energy. Formation of a core@shell Cu₂MoS₄ nanostructure was found to lead to

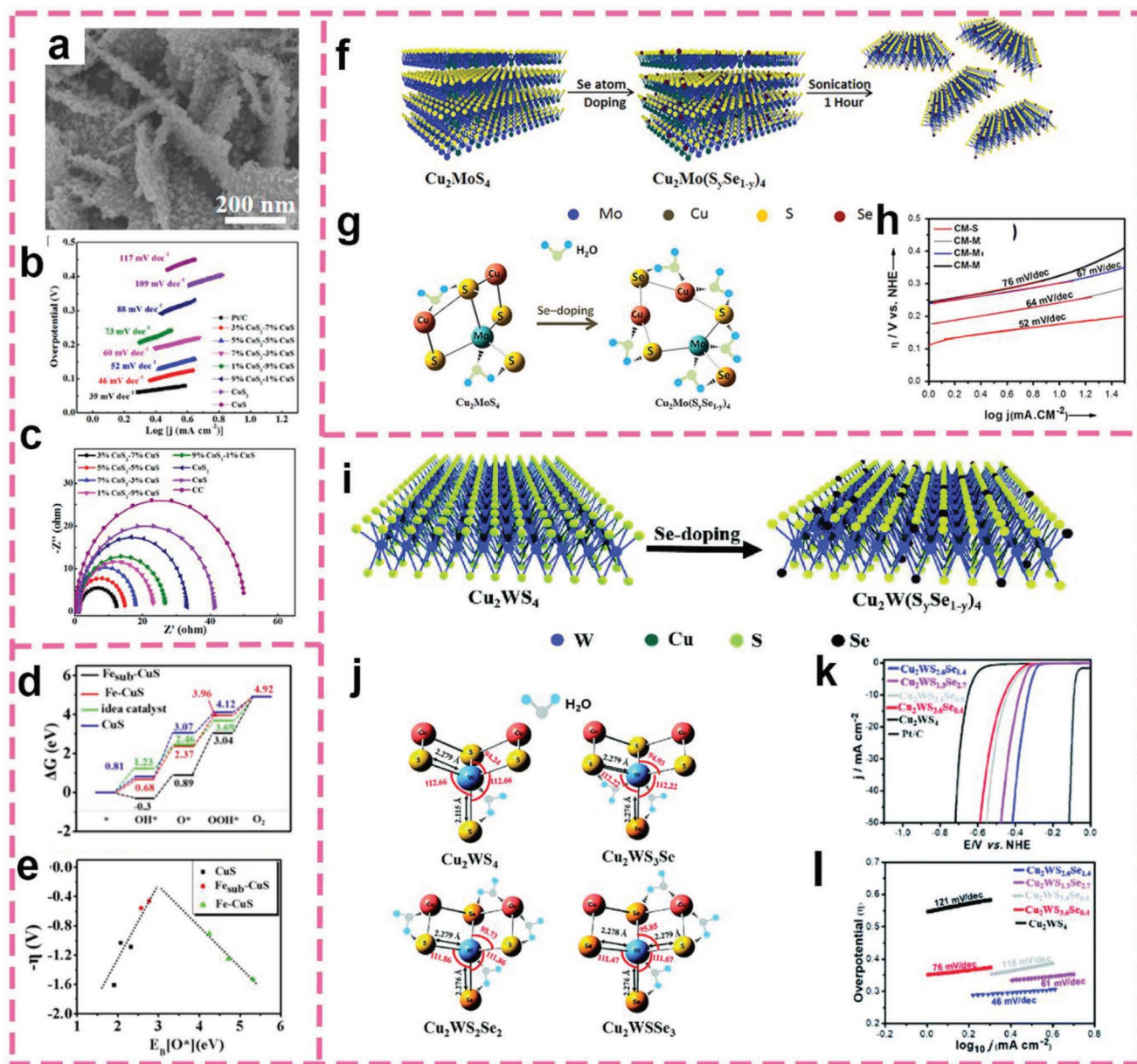


Figure 24. a) High-resolution SEM images of the 3% CoS₂-7% CuS catalyst. b) Tafel slopes for the as-prepared catalysts. c) Nyquist plots of the as-prepared catalysts. d) Free energy profiles for OER on CuS (100), Fe-doped surface CuS (100), and Fe-doped subsurface CuS(100) with lowest overpotentials. The ideal catalyst with zero overpotential is also illustrated. e) The volcano curve in oxygen evolution overpotential ($-\eta$) plotted as a function of the oxygen-binding energy ($E_{\text{B}}[\text{O}^*]$). f) Schematic Illustration of the making of single-layered Se doped Cu₂MoS₄. g) Optimized molecular structure of pristine and Se doped Cu₂MoS₄ and schematic illustration of hydrogen adsorption on the molecule. h) Tafel plots of different samples. i) Schematic illustration of anion substitution in TMC Cu₂WS₄. j) Optimized molecular structure of pristine Cu₂WS₄ and anion substituted Cu₂W(S_ySe_{1-y})₄ samples and schematic illustration of hydrogen adsorption on the molecule (red and black lines illustrate the bond angles (in degree) and bond lengths (in Å) respectively). k) Linear sweep voltammetry of the as-synthesized samples. l) Corresponding Tafel plots of the samples. a–c) Reproduced with permission.^[421] Copyright 2019, American Chemical Society. d,e) Reproduced with permission.^[425] Copyright 2021, American Chemical Society. f–h) Reproduced with permission.^[431] Copyright 2016, Elsevier. i–l) Reproduced with permission.^[432] Copyright 2018, The Royal Society of Chemistry.

further improvement of the electrocatalytic performance, due to multi-integrated active centers and cooperative effect.^[434]

Although there are few studies on copper-based phosphides compared with oxides and sulfides, recent studies on copper-based phosphides have shown impressive electrocatalytic activities. Hao and co-workers fabricated Cu₃P microsheets by high-temperature phosphating of copper chips on nickel

foam (Figure 25a).^[435] When used as a bifunctional catalyst, the sample prepared at 450 °C offered a small $\eta_{\text{OER},10}$ of 290 mV and $\eta_{\text{HER},10}$ of 130 mV, with a Tafel slope of 84 and 83 mV dec⁻¹, respectively. As shown in Figure 25b,c, it also demonstrated good stability for HER. The increased activities were ascribed to the superhydrophilicity and superaerophobicity of the Cu₃P microsheets, which enhanced the contact between the

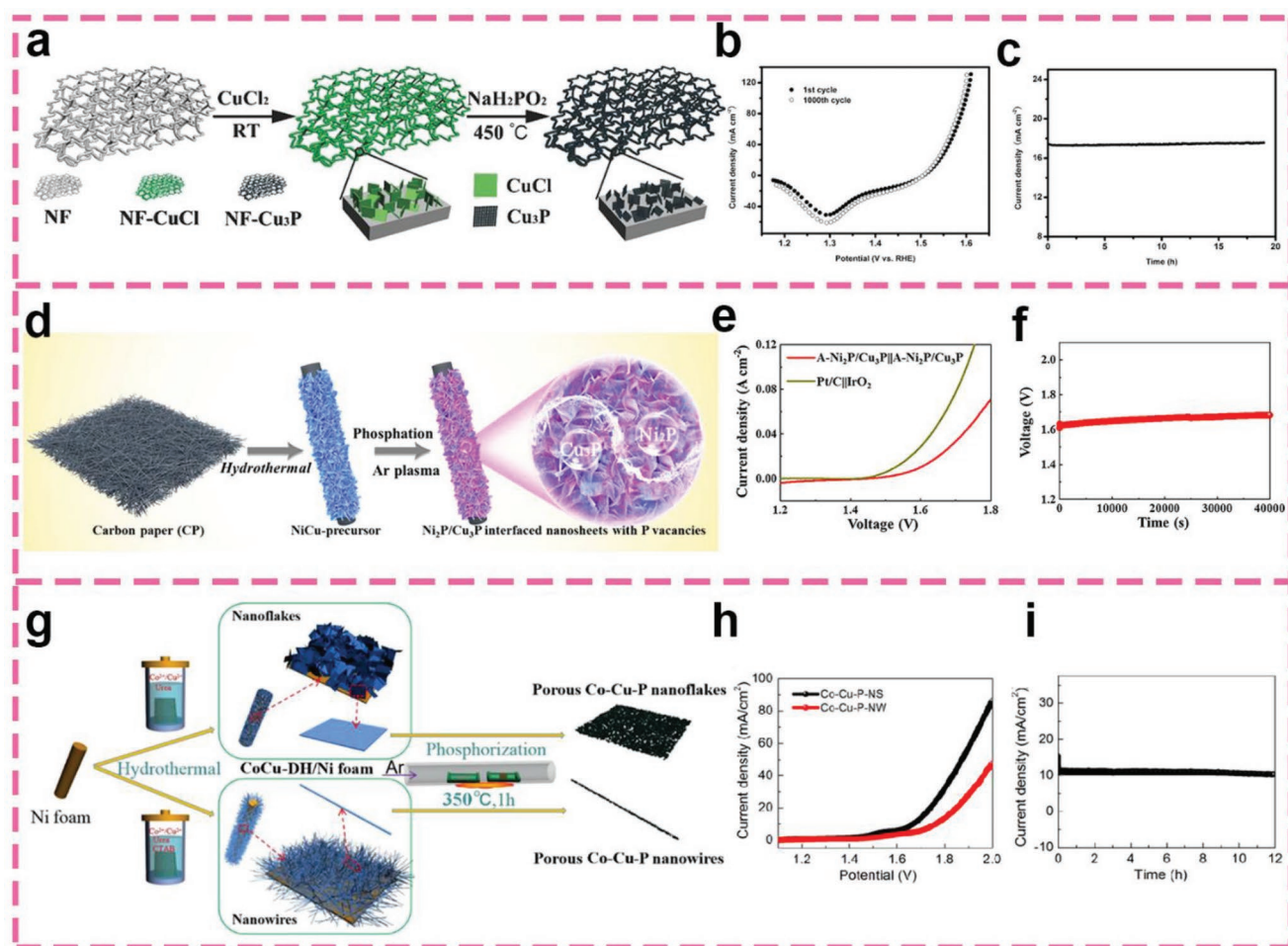


Figure 25. a) Illustration of the preparation of Cu_3P microsheets. b) Polarization curves of Cu_3P -450 microsheets in 1.0 M KOH at a scan rate of 2 mV s^{-1} before and after 1000 cycles. c) Long-term stability measurements for Cu_3P -450 microsheets in 1.0 M KOH for OER. d) Schematic illustration for synthesizing $\text{Ni}_2\text{P}/\text{Cu}_3\text{P}$ interface nanosheets with rich P vacancies. e) LSV curves of $\text{A-Ni}_2\text{P}/\text{Cu}_3\text{P}||\text{A-Ni}_2\text{P}/\text{Cu}_3\text{P}$ and commercial $\text{RuO}_2||\text{Pt}/\text{C}$. f) Multicurrent process over $\text{A-Ni}_2\text{P}/\text{Cu}_3\text{P}||\text{A-Ni}_2\text{P}/\text{Cu}_3\text{P}$ at 10 mA cm^{-2} . g) Schematic illustration of the growth process of Co-Cu-P-NS and Co-Cu-P-NW. h) Water electrolysis polarization curves of a symmetric electrolyzer using Co-Cu-P-NS. i) Time-dependent current density curve for 12 h. a–c) Reproduced with permission.^[435] Copyright 2016, Wiley-VCH. d–f) Reproduced with permission.^[438] Copyright 2019, Elsevier. g–i) Reproduced with permission.^[439] Copyright 2021, American Chemical Society.

electrolyte and electrode, and promoted bubbles extraction as well as effectively reduced the dead area of the electrode. Han et al. demonstrated for the first time that $\text{Cu}_3\text{P}@NF$ could be used as an Janus catalyst for OER, HER as well as overall water splitting.^[436]

However, in general, the electrocatalytic activity and stability of the Cu_3P -based nanomaterials are still lower than other transition metal phosphides, and further improvement is needed. Modifying the interface with bimetallic phosphate is an effective strategy to change the valence electron state and improve the inherent activity of the active center.^[437] Recently, Lin et al. increased the OER activity of $\text{Ni}_2\text{P}/\text{Cu}_3\text{P}$ in alkaline media by modulating the P-rich vacancies (Figure 25d).^[438] As bimetal phosphides improved the electronic conductivity and their defects accelerated the surface reaction, the $\text{Ni}_2\text{P}/\text{Cu}_3\text{P}$ nanosheets exhibited an outstanding water-splitting performance with a current density of 10 mA cm^{-2} under an

applied voltage of 1.60 V and maintained excellent stability (Figure 25e,f). More recently, Liu et al. prepared uniform cobalt-hybridized 2D Cu_3P nanosheets (Co-Cu-P-NS) that were nearly vertically arranged on nickel foam.^[439] As shown in Figure 25g, starting from a hydrothermally treated Co-Cu dihydroxide array, highly mesoporous 2D nanosheets and sugar gourd-like 1D nanowires were obtained by the phosphation process under the Ar plasma condition. The Co-Cu-P-NS exhibited an excellent electrocatalytic performance towards OER and HER, with an $\eta_{\text{OER},10}$ of 272 and $\eta_{\text{HER},10}$ of 72 mV in 1.0 M KOH, and a small Tafel slope of 83.2 and 70.4 mV dec^{-1} , respectively. Additionally, the Cu_3P -based electrolyzer required a cell voltage of only 1.66 V to achieve a current density of 10 mA cm^{-2} for overall water splitting, along with wonderful stability (Figure 25h,i). Tong et al. fabricated $\text{FeO}_x\text{-Cu}_3\text{P}@Cu$ catalysts and accomplished a very good HER electrocatalytic activity with an $\eta_{\text{HER},10}$ of 337 mV and a small Tafel slope of 48 mV dec^{-1} .^[440]

7.2.3. CO₂RR

Accelerated consumption of fossil fuels leads to the excessive emission and accumulation of carbon dioxide, and hence environmental consequences.^[441] CO₂RR is a promising technology to mitigate CO₂ emission.^[442] Yet, due to the high stability of CO₂, significant challenges remain in the design and optimization of CO₂RR catalysts.^[443–446] In general, CO is the most common and readily available product because it does not involve a proton transfer process. To attain high-value hydrocarbons, it is important to reduce the reaction overpotential, control the reaction pathway, and develop electrocatalysts with enhanced substrate selectivity. Up to date, copper-based materials have been unique in the electrocatalytic conversion of CO₂ to high value-added multicarbon products, as compared with other metals,^[447,448] because they can inhibit the competitive HER process and possess a moderate binding energy for key intermediates.^[449] For CO₂RR, its electrochemical performance is usually evaluated by the starting potential, current density, FE, Tafel slope, and electrochemical surface area. It should be noted that these indicators are related not only to the catalyst on the working electrode, but also to the electrolyte pH and the reaction temperature. For example, Wang et al. showed that the morphology of the catalyst and the type of electrolyte affected the performance of CO₂RR.^[450] The authors synthesized self-supporting Cu nanostructured electrodes consisting of nanowires, nanosheets, and nanoflowers by regulating the oxidation time of a Cu foam in strong alkaline oxidants. In the electrochemical tests, 1.0 mol L⁻¹ KHCO₃, KCl, and KH₂PO₄ solutions were selected as the electrolyte. They found that the nanostructured Cu electrode stabilized the transition states of CO₂ (ad) and CO*, which was beneficial to the further hydrogenation and isomerization process. The CO₂RR FE varied in the following order, KH₂PO₄ (1.0%, at 0.9 V vs RHE) < KCl (54.7%, at 0.5 V) < KHCO₃ (86.9%, at 0.4 V). It is argued that the anion species and pH might have a great influence on the selectivity of the products.^[451–453] The best performance toward multiple products was obtained with the catalyst prepared from the nanosheets in 1.0 mol L⁻¹ KHCO₃. This catalyst reduced CO₂ into methanol (CH₃OH), ethanol (EtOH), etc. with a total FE as high as 86.9%, at a low applied potential of -0.4 V versus RHE. Nevertheless, all examined electrodes revealed an unsatisfactory selectivity. The most commonly used improvement method is to introduce heteroatom dopants because of their strain and ligand effects in metal catalysts.^[454,455] Wang et al. prepared SnO₂-CuO nanosheets with the (-400) facet that enhanced the formation of ethylene (C₂H₄) (Figure 26a), where the current density for CO₂RR became higher at more negative potentials.^[456] The catalyst showed a much higher FE of C₂H₄ production compared to other samples, when the potential was gradually increased from -0.2 to -1.0 V, and achieved the highest FE (22%) at around -1.0 V (Figure 26b). The origin of the excellent activity of SnO₂-CuO nanosheets was revealed by DFT calculations, in which the doping of Sn led to the redistribution of charge in CuO (Figure 26b–f). The connection of two carbon atoms led to the intermediate CO-CHO, which might be further converted to C-C.^[457] The formation of these two intermediates was the key step in the formation of C₂H₄. The binding energy of C₂H₄ was about -0.37 eV, while the binding

energy of C-C and CO was -1.28 eV and -0.62 eV, respectively, indicating that C₂H₄ was easier to form. Wang and co-workers observed the concomitant morphological evolution of CuO nanosheets during operation and refined the mechanistic relationship between CH₄ and EtOH.^[458] In situ TEM measurements (Figure 26g), especially in 10–20 min, facet-orientated CuO nanosheets were aggregated into tree-like Cu dendrites, which represented the final stable morphology of the catalyst under flow conditions. Using millisecond-resolved differential electrochemical mass spectrometry, the authors elucidated that adsorbed *CH₃ was a common precursor of CH₄ and EtOH (Figure 26h), confirming a greater overpotential at the (110) steps adjacent to (100) terraces through a previously neglected pathway. As described in Figure 26i, the stable structure promoted the selectivity of C₂H₄, which showed an FE of 33% at 229 mA cm⁻² and remained constant without any obvious loss during 20 h (Figure 26j,k).

Recently CuS have been recognized as efficient CO₂RR electrocatalysts with a hydrocarbon selectivity. Zhao et al. reported cost-effective and facile methods to fabricate CuS nanosheet arrays on nickel foam (CuS@NF) by adopting a hydrothermal and polymerization process (Figure 27a).^[459] CO₂ was converted into CH₄ with a high FE (73±5% at -1.1 V) and a low Tafel slope (Figure 27b). CuS@NF possessed a highly open and porous structure, which enabled the electrode to have efficient mass transport in a large range and greatly reduced the dead volume of the electrode electroactive region (Figure 27c). Dou et al. carried out both experimental and computational studies to elaborate on the mechanism of selective production of formate (HCOO⁻).^[460] The CuS nanosheet arrays on brass were obtained by a one-step chemical bath procedure (Figure 27d). In this study, DFT calculations revealed that, on Cu(111)/CuS(102) surface, the S beneath the Cu⁰ layer reduced the binding energy of *COOH, which was beneficial to the desorption of HCOO* and *COOH intermediates, clarifying the high selectivity. Thus, as compared with the copper mesh sample, CuS/brass delivered a higher activity and selectivity for CO₂RR to HCOO⁻ at -0.7 V with an FE of 70.2 ± 1% (Figure 27c,f).

In addition to CuO and CuS, Cu-MOF can also be used as a catalyst for CO₂RR. Majidi and co-workers prepared 2D copper tetrahydroxyquinone (Cu-THQ) nanoflakes, and CO₂RR occurred at low overpotentials in a hybrid electrolyte, producing CO as the main product,^[461] with a current density of roughly 173 mA cm⁻² at -0.45 V and an excellent turnover frequency up to 20.82 s⁻¹ (Figure 27g,h). The origin of the excellent CO₂-to-CO activity of Cu-THQ nanoflakes was revealed by DFT calculations (Figure 27i,j), in which the rate-determining step of *COOH formation required a ΔG of 0.74 eV, lower than for CO desorption (0.90 eV), but the CO adsorption free energy decreased with increasing adsorption coverage. They found that the reduced Cu (Cu⁺) during CO₂RR was reversibly oxidized to Cu²⁺ after reaction. In addition, Laursen et al. reported the catalytic activity and mechanism of Cu₃P for CO₂RR to HCOO⁻.^[25] After a series of experiments and characterization, they concluded that Cu₃P [001] had good catalytic activity within 16 h, and the formation of surface hydride at the isolated *H-CuP₃ site was the catalytic site for the formation of H₂ and HCOO⁻, and the long-time Cu-Cu separation hindered the formation of C-C coupling products.

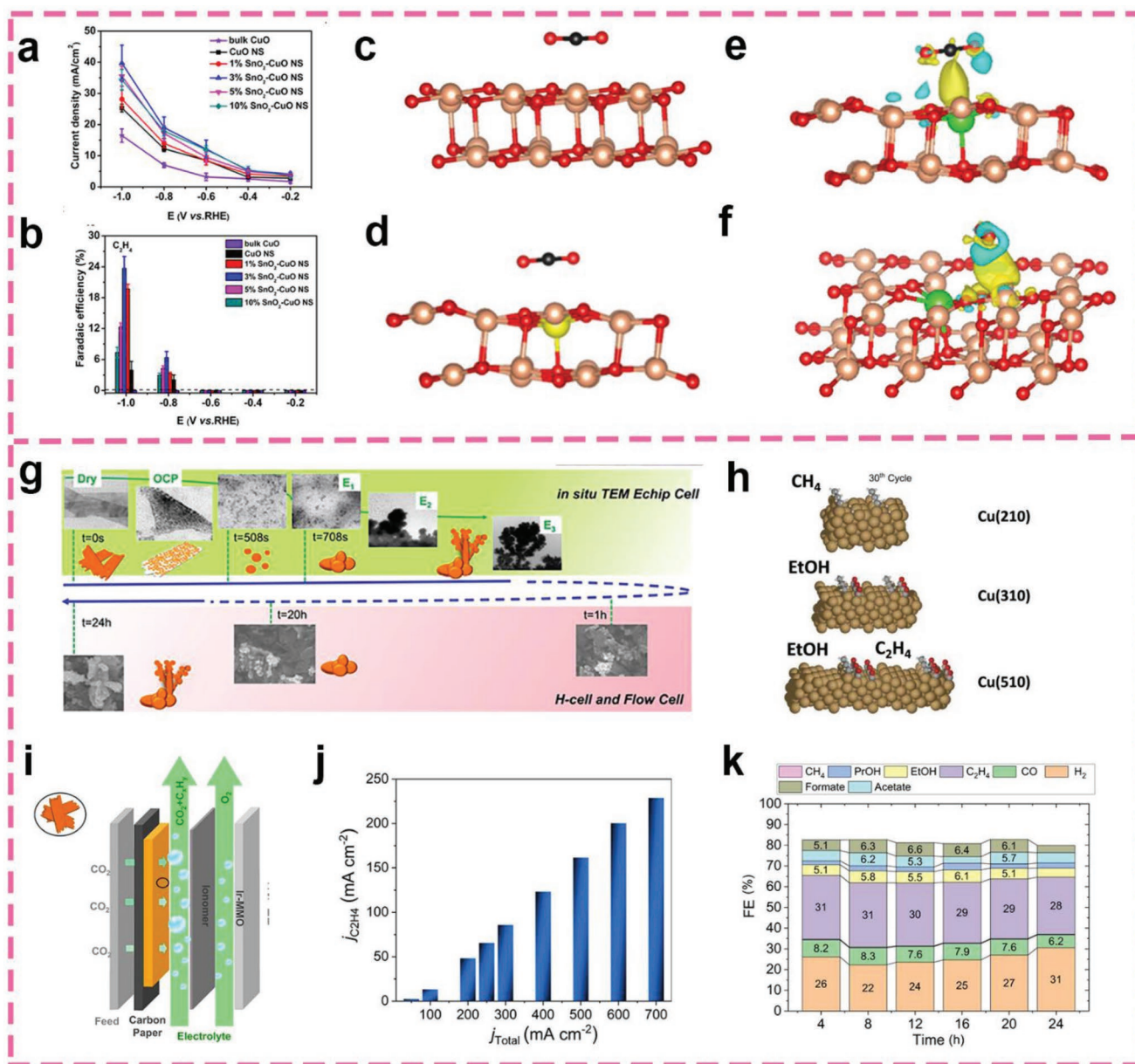


Figure 26. a) Current density of electroreduction of CO₂ using different catalysts. b) Total Faradaic efficiency of electroreduction of CO₂ using the as-prepared catalysts. c) Structure of CO₂ on the CuO substrate. d) SnO₂-modified CuO substrate. e, f) Charge difference map of a CO₂-SnO₂-modified CuO system. Carbon atoms are black, oxygen atoms are red, copper atoms are orange, and the tin atom is green. g) Schematic overview (time line) of the experimentally observed evolution of the CuO NS morphology probed by the in situ TEM E-chip flow cell, H-cell, and flow cell electrolyzer. h) Illustration of *CH₃ as common intermediate of CH₄ and EtOH. i) Schematic representation of the flow cell electrolyzer. j) The partial current density of C₂H₄. k) Stability test at a geometric current density of 300 mA cm⁻², displaying the Faradaic efficiencies as a function of time. a–f) Reproduced with permission.^[456] Copyright 2020, American Chemical Society. g–k) Reproduced with permission.^[458] Copyright 2021, Springer Nature.

7.3. Summary

In summary, most Cu–O, Cu–S, and Cu–P nanosheets have been found to manifest excellent catalytic performance in metal–air batteries (Table 5), water splitting (Table 6), and CO₂RR (Table 7). However, the conductivity, activity, and stability remain unsatisfactory and further research of the structural engineering of 2D nanomaterials is strongly desired. Strategically, more in-depth research on their complexes, other nonprecious metals,

and even binary or ternary compounds are needed for hybridization with copper-based materials, thereby improving their conversion rate and stability of the catalytic reaction.

8. Advanced Characterization Techniques

The growth laws and characteristics of nanomaterials are different from those of traditional materials. It usually occurs

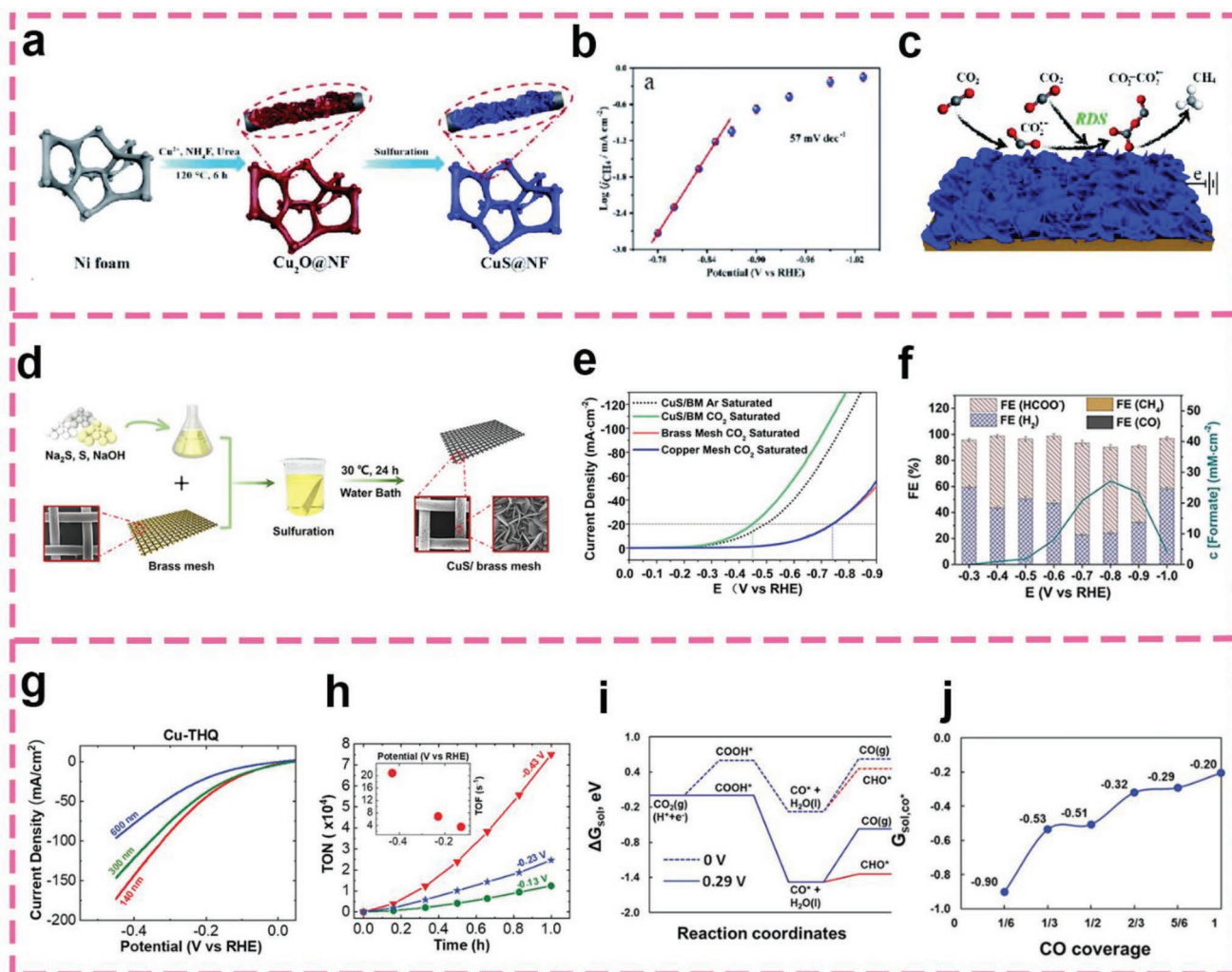


Figure 27. a) Illustration of the fabrication process. b) Tafel plot. c) Scheme showing the electroreduction of CO_2 into CH_4 on the CuS@NF . d) Fabrication process for CuS nanosheet arrays/brass mesh. e) LSV curves of CuS/BM in Ar and CO_2 -saturated 0.5 M KHCO_3 electrolyte at a sweep rate of 10 mV s^{-1} , and the comparison with brass mesh and copper mesh in CO_2 -saturated electrolyte. f) FEs of products CO , CH_4 , H_2 , and HCOO^- and the concentrations of HCOO^- at different potentials over CuS/BM with PTFE. g) LSV results (scan rate of 50 mV s^{-1}) for electrochemical reduction of CO_2 in 1 M choline chloride and 1 M KOH using Cu-THQ NFs for different particle sizes. h) TONs for CO production during 1 h chronoamperometry experiments at controlled potentials. The inset shows TOFs at these potentials after 1 h . i) The free energies including solvation corrections for CO production on Cu-THQ at 0 V versus RHE in dotted blue lines and at overpotential η of 0.29 V in solid blue lines. The pathways for CHO^* are shown with red lines. j) The adsorption-free energies of CO at different coverages on Cu-THQ . a–c) Reproduced with permission.^[459] Copyright 2017, The Royal Society of Chemistry. d–f) Reproduced with permission.^[460] Copyright 2021, American Chemical Society. g–j) Reproduced with permission.^[461] Copyright 2016, Wiley-VCH.

in the nonequilibrium state of small nano-space, and there are many possibilities of directional, polar and preferential growth in the growth environment of temperature, pressure, and liquid concentration. The change of any factor in the system will lead to a huge difference in results.^[28] Therefore, in order to understand the dynamic instantaneous and accurate information of the growth process of 2D copper-based materials, master the growth parameters and characteristics of materials in the synthesis process, realize controllable synthesis, and prepare materials with excellent performance, it is necessary to select appropriate cutting-edge characterization techniques. In this section, we will give a brief overview about the leading techniques for materials structural characterization.^[462]

8.1. In Situ Microscopy

The size, morphology, exposed surface, and uniformity of copper-based materials are several important parameters that affect their electrochemical properties. Currently, SEM, TEM, and atomic force microscopy (AFM) are the three typical imaging techniques that can directly observe the growth and microstructural features of these materials.

8.1.1. Scanning Electron Microscopy

Generally, SEM is mainly used to observe the surface morphology of materials. In some cases, it can also measure the

Table 5. Summary of 2D copper-based materials for energy-related in metal–air batteries.

Catalyst	Method	ORR activity	OER activity	Battery performance	Refs.
Ce-doped CuO	Anion exchange	onset potential: -0.23 V Tafel slope: 146 mV dec $^{-1}$ $n = 3.45$	–	Cycling ability: 2000 cycles (20 h)	[387]
Cu-N/C	Thermal treatment	Half-wave potential: 0.9 V Tafel slope: 55.1 mV dec $^{-1}$	–	Open-circuit voltage: 1.41 V Power density: 134.7 mW cm $^{-2}$ at 231.9 mA cm $^{-2}$	[388]
Co-Cu LDH	Coprecipitation	–	–	Voltage gap: 1.41 V Capacity: 4870 mAh g $^{-1}$ at 200 mA g $^{-1}$	[389]
CuCo $_2$ O $_4$	Hydrothermal	–	–	Capacity: $1,1793$ mAh g $^{-1}$ at 200 mA g $^{-1}$ Potential gap: 0.95 V	[394]
CuCo $_2$ S $_4$	Exfoliation	Onset potential: 0.9 V Half-wave potential: 0.7 V	Overpotential: 287 mV at 10 mA cm $^{-2}$ Tafel slope: 46 mV dec $^{-1}$	Open circuit potential: 1.2 V Cycling ability: 66 cycles (22 h)	[398]
CuCo $_2$ S $_4$	Sulfurization	Half-wave potential: 0.9 V	Overpotential: 337 mV at 10 mA cm $^{-2}$	80.4% of initial current density (10 h)	[395]
CuCo $_2$ S $_4$	Hydrothermal	Improved reaction dynamics	Improved reaction dynamics	Discharge capacity: 9089 mAh g $^{-1}$ at 100 mA g $^{-1}$ Cycling ability: 176 cycles @ 500 mAh g $^{-1}$	[396]
CuCo $_2$ S $_4$	Solvothermal	–	Overpotential: 290 mV at 10 mA cm $^{-2}$ Tafel slope: 81.3 mV dec $^{-1}$	Open-circuit voltage: 1.38 V Power density: 123.9 mW cm $^{-2}$	[401]
CuCo $_2$ S $_4$ @Ni	Hydrothermal	–	–	Overpotential: 0.82 V Capacity: 9673 mAh g $^{-1}$ at 100 mA g $^{-1}$ Cycling ability: > 164 cycles	[397]
CuCo $_2$ S $_4$ @N-CNFs	Electrospinning	Onset potential: 0.957 V Tafel slope: 51 mV dec $^{-1}$	Overpotential: 315 mV at 10 mA cm $^{-2}$ Tafel slope: 45 mV dec $^{-1}$	Open circuit potential: 1.46 V Capacity: 896 mAh g $^{-1}$ at 200 mA g $^{-1}$	[400]

size, element distribution, and even porosity of materials.^[463] The resolution of the microscope used is about 10 nm. In this technology, samples are scanned one by one with electron beam to generate secondary electrons and other signals, which are then picked up and imprinted by the detection equipment. In Lv's work, the morphology of Cu $_2$ O was measured by SEM and the influence of synthesis parameters on its growth process was studied.^[464] SEM can also be used to detect the changes of electrode material structure in electrochemical process. Fang et al. used SEM to examine the Li plating/stripping behavior on the vertically aligned CuO nanosheets, where the results showed the importance of CuO growth on the surface of Cu foil and the thin lipophilic layer to achieve uniform lithium deposition.^[465] From the side-view SEM images of the pristine planar Cu substrate, after a number of cycles, there were obvious dendrites, resulting in uneven distribution of the electric field, and the growth of dendrites and tip effect were strengthened. With the increase of cycle times, the thickness of the Li plating layer increased. After 100 cycles, the thickness of the Li plating layer was about 41.07 μ m. In contrast, although the Li plating thickness of CuO nanosheets was only a little smaller, the Li metal on the substrate had a uniform morphology and flat surface. Nevertheless, the operation of SEM requires a high vacuum working condition and conductive samples.

8.1.2. Transmission Electron Microscopy

TEM detects electrons transmitted by thin samples or nanocells to acquire the information of element/component and

electronic structure, resulting in high-resolution images of electrode materials during electrochemical processes.^[466] The microstructure of the electrode materials can be observed in detail by adjusting the magnification, where high-resolution structural images, atomic images, lattice fringes, crystal defects, etc. can be produced.^[467] It can be used to observe the morphology and phase transitions of copper-based materials in electrochemical reactions. An interesting and important study on the electrochemical reaction pathways of CuO was investigated by TEM characterization.^[468] Park et al. employed in/ex situ HRTEM to directly observe the morphological evolution of CuS nanoplates and the formation of the SEI layer during the sodiation/desodiation processes, which further proved the mechanism of pulverization-tolerance and capacity recovery.^[469] The disintegrated nanoplates well maintained their original shape with stable SEI layers after 20, 50, and 240 cycles, revealing that the exposure of CuS for facile sodium insertion/extraction increased the active surface area and well reflected the reduction of charge transfer resistance. In general, single-crystal CuS contains grain boundaries and semicoherent phase interfaces between intercalation and conversion phases, as described in the schematic model in **Figure 28e**. From the TEM images of the unique crystal structural evolution of CuS sodiation (Figure 28f–i), the results demonstrated that because the semicoherent phase interface caused stress relaxation by forming grains and grain boundaries rather than random crushing, the CuS nanoplates still retained the ability of recovery and the original shape even after complete disintegration. This phenomenon is beneficial to provide additional channels for the diffusion connection of Na $^+$, resulting in

Table 6. Summary of 2D copper-based materials for energy-related in water splitting.

Catalyst	Method	Electrolyte	Stability [h]	Tafel slope η [mV dec ⁻¹]		Overpotential [mV] @10 [mA cm ⁻²]		Refs.
				HER	OER	HER	OER	
Ni/Cu	Galvanostatic electrodeposition	1 M KOH	50	42.7	–	38	–	[405]
NiCu mixed oxide	Chemical reduction	1 M KOH	30	120	–	200	–	[406]
CuO	CBD	1 M KOH	10	–	59	–	350	[410]
Cu _x Co _{2-x} O ₄	Electrodeposition	1 M KOH	–	–	77	–	276@20	[83]
CuCo ₂ O ₄	Electrodeposition	1 M KOH	25	–	64	–	252@20	[194]
CuCo ₂ O ₄	Hydrothermal	1 M KOH	12	–	92.5	–	220	[413]
Cu ₂ S/CF	Anion exchange	1 M KOH	10	–	101	–	252@20	[416]
Graphdiyne/CuS	In situ polymerization	1 M KOH	35	63.8	–	106	–	[417]
CuS@C	Hydrothermal	0.5 M H ₂ SO ₄	20	44	–	128	–	[419]
CoS ₂ /CuS	Hydrothermal	0.5 M H ₂ SO ₄	–	46	–	62	–	[421]
Fe-CuS	Redox process	1 M KOH	10	–	41	–	252@20	[425]
CuCo ₂ S ₄	Hydrothermal	1 M KOH	25	–	117	–	290@20	[62]
CuCo ₂ S ₄	Hydrothermal	1 M KOH	12	–	86	–	310	[428]
CuCo ₂ S ₄	Solvothermal	1 M KOH	40	–	81.3	–	290	[401]
CuCo ₂ S ₄	Solvothermal	1 M KOH	10	55.4	43.8	69	210	[426]
CuNiS	CBD	1 M KOH	50	63	43	99	337	[364]
Cu ₂ Se/Cu	Hydrothermal	0.5 M H ₂ SO ₄	–	35	–	212	–	[363]
Cu ₂ Mo(S _y Se _{1-y}) ₄	Solution processed	0.5 M PhOH ₂ SO ₄	15	52	–	96	–	[431]
Cu ₂ W(S _y Se _{1-y}) ₄	Anion substitution	0.5 M H ₂ SO ₄	12	46	–	320	–	[432]
Cu ₃ P	Phosphidation	1 M KOH	24	83	84	130	290	[435]
Cu ₃ P	Hydrothermal	1 M KOH	24	42	54	105	320	[436]
Cu ₃ P/CFC	Hydrothermal	1 M KOH	–	147.1	–	–	–	[437]
Ni ₂ P/Cu ₃ P	Hydrothermal	1 M KOH	–	89.0	78.1	88	262	[438]
Co-Cu ₃ P	Hydrothermal	1 M KOH	20	70.4	83.2	99	272	[439]
FeO _x -Cu ₃ P@Cu	Hydrothermal	1 M KOH	24	58.8	–	48	–	[440]

robust cycle stability of CuS. Lei et al. studied S vacancies in CuS_{1-x}@PAN by high-angle annular dark-field scanning transmission electron microscopy (HAADF-STEM). Figure 28j,k

clearly displayed the atomic arrangement of S and Cu atoms and some missing atoms from the lattice, proving the existence of S-vacancies.^[470]

Table 7. Summary of 2D copper-based materials for energy-related in CO₂RR.

Catalyst	Method	Electrolyte	Potential	Major product	Faradaic efficiency [%]	Current density [mA cm ⁻²]	Refs.
Cu	Electrochemical reduction	0.1 M K ₂ SO ₄	–1.18 V vs RHE	C ₂ H ₄	83.2	60	[447]
Cu	Electrochemical reduction	0.1 M KHCO ₃	–1.03 V vs RHE	HCOOH	40.1 ± 1.7	40	[448]
Cu-oxide	Wet oxidation and electrodeposition	0.2 M KHCO ₃	–1.1 V vs RHE	C ₂ H ₄	29.7	35.6	[452]
CuO	Reduction– oxidation reconstruction	0.1 M KHCO ₃	–1.3 V vs RHE	C ₂ H ₄	30	–	[365]
CuO	Wet-chemistry and sulfurization	0.1 M KHCO ₃	–1.0 V vs RHE	C ₂ +	–	>400	[458]
Br _{1.95%} -CuO	Liquid phase	0.1 M KHCO ₃	–0.6 V vs RHE	C ₂ H ₅ OH	53.3	7.1	[97]
SnO ₂ /CuS	One-pot scalable synthesis	0.1 M KHCO ₃	–0.8 V vs RHE	CO	85	12	[123]
SnO-CuO	Hydrothermal	0.5 M KHCO ₃	–1.0 V vs RHE	C ₂ H ₄	22	–	[456]
CuS	Hydrothermal and sulfurization	0.1 M KHCO ₃	–1.1 V vs RHE	CH ₄	73 ± 5	–	[459]
CuS	Chemical bath deposition	0.5 M KHCO ₃	–0.7 V vs RHE	Formate	70	50	[460]
Cu ₃ P/Cu	Electrochemical reduction	0.1 M KHCO ₃	–0.1 V vs RHE	Formate	0.9	–	[25]

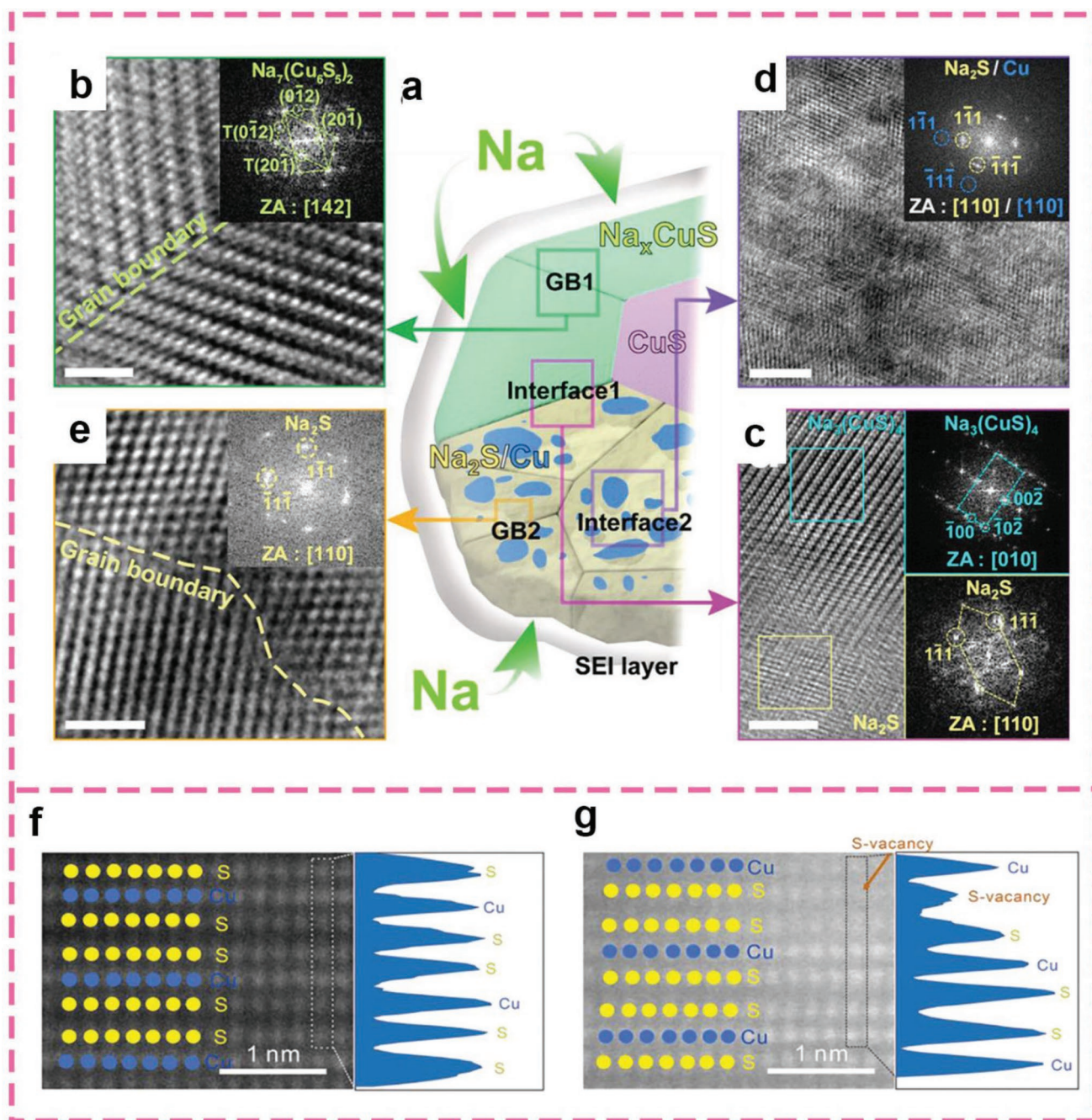


Figure 28. a) Schematic model demonstrating grain boundaries and phase interfaces formations in Na_xCuS phases. b) HR-TEM images of grain boundaries were formed by different Na inserting orientations (scale bar, 2 nm). c) Stress relaxation during the conversion reaction (scale bar, 2 nm). d) HR-TEM images of phase interfaces between the intercalation and the conversion phases (scale bar, 5 nm), and between a) Na_2S and Cu (scale bar, 5 nm). e) Between Na_2S and Cu (scale bar, 5 nm). HAADF-STEM images of f) pure CuS and g) $\text{CuS}_{1-x}@\text{PANI}$. a–e) Reproduced with permission.^[469] Copyright 2019, Wiley-VCH. f, g) Reproduced with permission.^[470] Copyright 2022, Wiley-VCH.

8.1.3. Atomic Force Microscopy

AFM is a mechanical microscope that converts the interaction force between the tip and the sample surface into the displacement of the cantilever tip sensor.^[471] It can monitor individual ultrathin nanostructured film and provide information on the size and thickness of the transverse sheet, which has attracted

significant attention in the analysis of 2D materials.^[29] Copper-based materials are similar to other 2D materials in this regard. AFM has better resolution and ease of operation than SEM and optical microscopy. For instance, the length-to-thickness ratio of Cu_3P was measured to be 3000 by Zhu et al., where the sizes of porous Cu_3P nanosheets ranged from a few nanometers to microns.^[289] Li et al. evaluated the thickness of 2D CuCo_2S_4

by AFM in 2018, showing a thickness of about 4–6 atomic layers.^[398] Chauhan et al. used AFM to measure the thickness of CuCo_2S_4 nanosheets, and observed an average thickness of the nanosheets in a similar range.^[428] Nevertheless, AFM measurements cannot reveal the thermodynamic and kinetic information of the growth process of nanomaterials.^[472]

8.2. In Situ X-Ray Spectroscopy

The advantage of X-rays as an analytical tool is that their interaction with substances leads to different kinds of phenomena, which has important implications in the quantitative and qualitative analysis of materials. X-ray waves are nondestructive and pollution-free to crystal materials.

8.2.1. In Situ X-Ray Diffraction

XRD is of great significance to understand the materials structures. Compared with the traditional XRD, in situ XRD can accurately and directly reflect the formation and evolution dynamics of the internal structure of materials.^[473] Upon X-rays irradiation on the sample, a series of diffraction peaks with different intensities appear at different angles. The crystal structure, phase composition and particle size of the sample can be determined by systematically analyzing the position, intensity, and shape of the peaks.^[474] In electrochemical systems, in situ XRD is a typical advanced technology to study the structural changes and energy storage mechanism of the electrode materials. Shi et al. synthesized MOF-derived copper-based nanosheets at different cathodization times, and determined the crystal structure and surface compositions of the samples by XRD measurements, as well as investigated their electrocatalysis in alkaline media.^[475] Jin et al. used in situ XRD as an effective tool to study CuS as electrodes for flexible SCs, and explored the phase changes of CuS nanosheets during the galvanostatic electrodeposition process.^[81] The results indicated that the deposited CuS contained a combined composition due to the coexistence of multiple Cu^{x+} between Cu^{2+} and Cu derived from the reduction of Cu^{2+} near the cathode. To explicate the effect of hierarchical core–shell architectures on the enhanced rate capability and special cycle life, Zhao's group carried out in situ XRD to examine the changes of the diffraction peaks during the whole galvanostatic test process to explore the electrode reaction.^[358] As shown in **Figure 29a,b**, the original CuS and CuSe signals showed significant declines, and the evolution of the patterns of the sample manifested new miscellaneous peaks when discharging from the initial open-circuit voltage to 1.5 V, which indicated the occurrence of intercalation reaction. Further deep discharges to 0.4 V strongly indicated the CuS/CuSe conversion reaction. Moreover, as the discharge process progressed, the relatively weak peaks of Cu_2S with (102) planes and Cu_2Se with (200) planes gradually appeared, which were not reversible during the subsequent charging process. The patterns of Na_2S and Na_2Se after delithiation still existed, accompanied by the disappearance of Cu_2S at a fully discharged state of 0.01 V. The corresponding peak of Na_2S , Na_2Se , and Cu gradually disappeared and intermediates were formed again

when the voltage changed between 0.01 and 3.0 V. The complete disappearance of byproducts NaCuSe and $\text{Na}_3\text{Cu}_4\text{S}_4$ phase represented the end of the reverse intercalation when continuously charged to 3.0 V. **Figure 29c** displayed the conversion mechanism of CuS@CuSe . However, in catalytic studies, XRD has some limitations because it underestimates the contribution of intermediates in the reaction, such as strongly disordered or low-dimensional phase and metastable states.^[476]

8.2.2. X-Ray Photoelectron Spectroscopy

Another powerful method for analyzing copper-based structure is X-ray photoelectron spectroscopy (XPS), also known as electron spectroscopy for chemical analysis (ESCA), which is mainly used for surface analysis and characterization in materials, physics, optoelectronics, and other fields, including molecular structure composition and chemical state of surface elements, especially atomic valence state, surface atomic electron cloud, and energy level structure.^[477,478] It typically uses X-rays to excite the core electrons of sample atoms and detect the generated photoelectron signals. XPS is widely applicable to almost all elements in the periodic table, with a concentration >0.1 at% and a surface resolution of 0.1 eV, except for hydrogen and helium.^[473] Tang et al. investigated the conversion reaction associated with Li insertion and extraction from CuO nanoparticle electrodes using in situ XPS and Auger electron spectroscopy. They observed the partial reversible conversion of Cu with Li and the formation of Li_2O in the conversion reaction of CuO in electrolyte.^[479] This can be specified as the first in situ XPS analysis under real battery conditions of Li^+ cycling. The importance of water vapor and adsorbed water in the transformation of CuS to CuSO_4 was directly studied by comparing the results in humid environments.^[480] **Figure 29d** displays the Cu 2p and S 2p XPS spectra of the covellite CuS prior to oxidation and after oxidation under different conditions. It was confirmed that sulfide was irreversibly oxidized to sulfate and copper ion initially had Cu^+ similar to the original oxidation state, but was oxidized to Cu^{2+} at higher relative humidity. However, due to the requirements of an ultrahigh vacuum condition, in situ applications of standard XPS are restricted.

8.2.3. X-Ray Absorption Spectrum

X-ray absorption spectrum (XAS) generally depends on synchrotron radiation X-ray light sources with high intensity, high brightness, and continuous energy variation.^[481] Unlike XRD, which provides information about the overall structure of the material, XAS provides information about the local environment of the element. It is worth mentioning that the XAS experiment usually does not need ultrahigh vacuum conditions, because it is usually detected at the K-edge, and the edge position of these elements is higher than 4 keV. XAS consists of two parts (**Figure 29e**): one is X-ray absorption near edge structure (XANES), which is strongly sensitive to valence and the coordination geometry, and the other is the extended X-ray absorption fine structure (EXAFS), which is mainly based on the scattering of photons by adjacent atoms. Information can

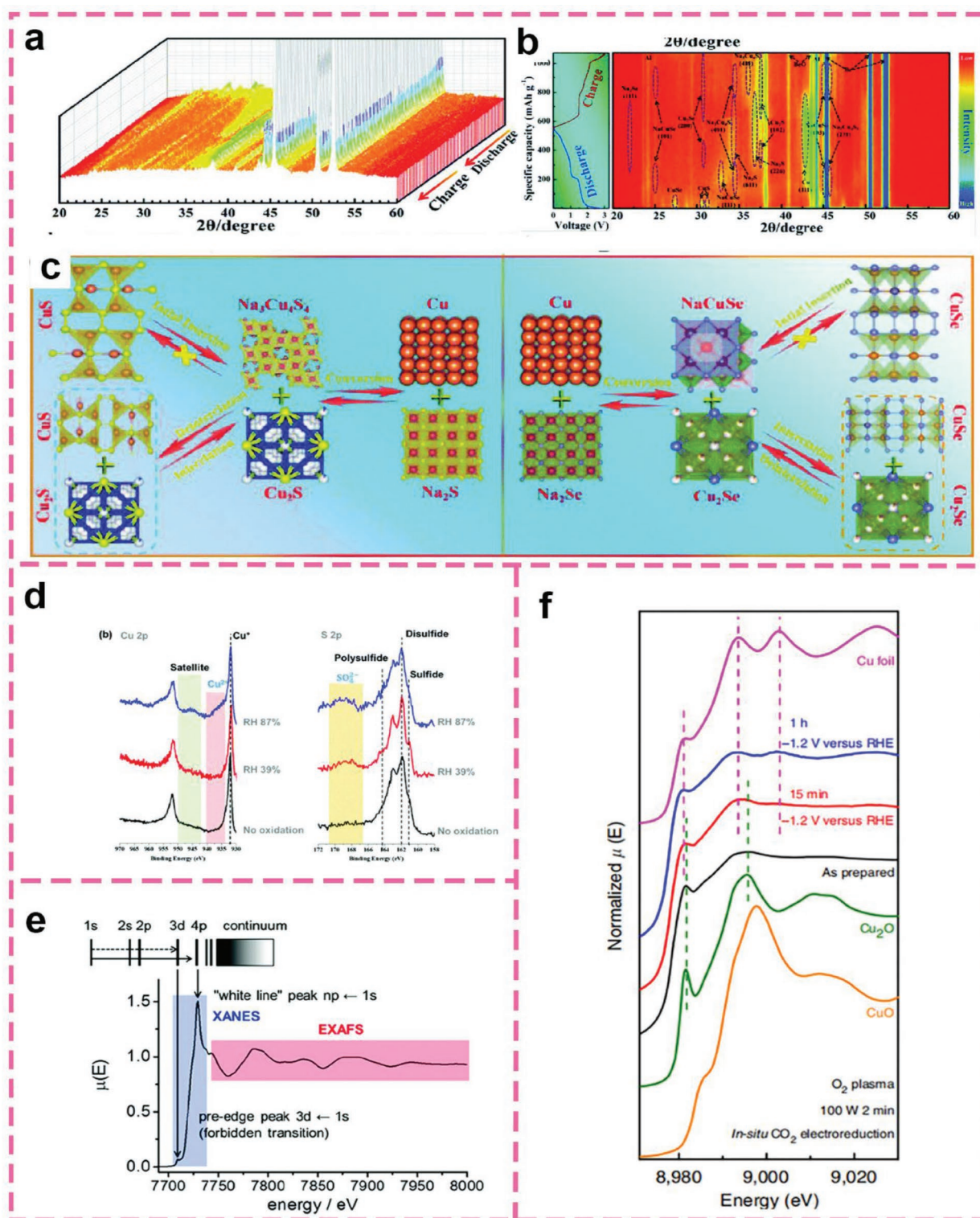


Figure 29. a) In situ XRD stacked patterns. b) Contour plots of the CuS@CuSe electrode during the initial cycle. c) The schematic graph of the sodium storage mechanism of the CuS@CuSe electrode. d) High-resolution XPS data for covellite NPs prior to oxidation and after oxidation under various humid conditions: Cu 2p region (left) and S 2p region (right). The Cu and S $2p_{1/2}$ peaks are labeled and marked with a dashed line in the spectra prior to oxidation. e) Schematic representation of a K-edge spectrum; blue: XANES region, red: EXAFS region. f) XANES spectra of the O_2 100 W 2 min treated sample measured under operando conditions in 0.1 M KHCO_3 during the first 15 min and after 1 h of reaction at -1.2 V versus RHE. Bulk Cu, Cu_2O , and CuO spectra are plotted as reference. a–c) Reproduced with permission.^[358] Copyright 2021, The Royal Society of Chemistry. d) Reproduced with permission.^[480] Copyright 2020, The Royal Society of Chemistry. e) Reproduced with permission.^[482] Copyright 2017, The Royal Society of Chemistry. f) Reproduced with permission.^[484] Copyright 2017, Springer Nature.

be used to quantify local geometry (such as the number, distance, and disorder of adjacent atoms).^[482] Both techniques are employed to discuss a wide range of nanomaterials, including crystalline, amorphous, and disordered materials, to determine local and electronic structures.^[483] Therefore, the XAS technique is suitable for in situ experiments. For example, Mistry et al. supplied experimental evidence for the change of the oxide layer structure and the survival of Cu⁺ species during CO₂RR through EXAFS and XANES measurements.^[484] The thickness of the sample led to the suppression of XAFS signals due to self-absorption. From the XANES spectra (Figure 29f), the as-prepared plasma-oxidized Cu contained the characteristics of Cu₂O (especially the green dotted line at about 8982 eV). When the catalytic activity of O₂ and H₂ plasma treating Cu at 100 W for 2 minutes was compared, operando EXAFS measurements of the Cu films treated with O₂ plasma showed that a combination of Cu and Cu₂O remained in the catalyst during the first 15 min of CO₂RR at 1.2 V, and after 1 h, only metallic Cu features were discernable. By eliminating the interference of roughness, they found that the presence of Cu⁺ was pivotal to reduce the starting potential and improving ethylene selectivity. In situ X-ray technology can accurately and directly reflect the formation and evolution of the internal structure of materials, which is of great scientific significance to explore the growth kinetics of materials.

8.3. Vibrational Analytical Techniques

The principle of vibration spectroscopy is that the radiation waves of the source interact with the bond frequency of the analyzed chemical substance.^[485] It is usually nondestructive, noncontact and nonvacuum. The most commonly used techniques are Raman spectroscopy and Fourier transform infrared spectroscopy (FT-IR). In addition to analyzing the chemical composition of samples, they can also be used to evaluate the structural characteristics.^[486,487] While vibration technology is harmless to substances, there are some limitations as vibration technology is not specific to all chemicals. Furthermore, it only provides chemical composition information, not the location and morphology of the species.

FT-IR utilizes the infrared band of electromagnetic radiation (14300–20 cm⁻¹) to analyze surface or interface species, and monitor the change of dipole moments by exciting their molecular vibration, rotation, lattice mode or their combination. It is mainly used to detect organic functional groups, ionic bonding, coordination, and other chemical conditions. Sarilmaz et al. prepared P-Cu₂WSe₄ nanosheets through a hot-injection route and performed FTIR analysis to see if organic molecules could be seen on the surface of the nanosheets.^[488]

Raman spectroscopy is a vibrational spectroscopy technology to observe low-frequency modes such as vibrations and rotations.^[462] It can determine molecular fingerprints, obtain lattice vibration information, and characterize the crystal quality and number of layers of samples.^[489] The combination of Raman spectroscopy and electrochemistry can provide real-time spectral information, which is helpful for understanding the electrochemically driven reaction mechanism.^[409] In Živcová's work,

the spectra of the dry CuSCN layers showed that SCN⁻ bound to Cu mainly through its S⁻ end (Cu–S–C≡N) in the form of thiocyanate resonance.^[490] Nevertheless, Raman spectroscopy (changes in frequency and intensity) can be influenced by double-layer charge (electrochemical doping) and the Faraday process on the electrode surface. In situ Raman microdroplet spectroelectrochemistry was used and the spectra of the original dry CuSCN layers electrodeposited on various substrates were collected at varied potentials and compared with the Raman spectra of dry CuSCN layers on each substrate. The main limitation of Raman spectroscopy is that the substances need to exhibit nonzero molecular polarizability. Therefore, some surface enhancement auxiliary technologies are usually required to enhance signals.

9. Summary and Perspective

Development of new energy technologies is a critical part of the sustainable economy, in which rational design and engineering of low-cost, high-performance catalysts represent an important first step. 2D copper-based materials have been attracting extensive attention. The 2D sheet morphology provides a large surface area for electrochemical reaction and electrolyte diffusion. The abundant transition metals on the earth significantly reduce the cost, which is conducive to large-scale applications of the electrochemical devices. In this review, we systematically examine the crystal structure, electronic structure design, synthesis methods, and advanced characterization techniques of a range of 2D copper-based materials, which have found diverse applications in the development of new electrochemical energy technologies, in particular, SCs, rechargeable ion batteries, metal–air batteries, and water electrolyzers.

Recently, there are many reports about the performance of various 2D copper-based electrode materials in EES and conversion applications, but they are far from the practical standards. Therefore, on the basis of a lot of precious work, the development and exploration directions of 2D copper-based nanomaterials can focus on the following aspects.

Compared with the 0D and 1D counterparts, 2D materials usually have the characteristics of a high surface energy, thermodynamic instability, and difficult synthesis. At present, due to the lack of large-scale and efficient synthetic approaches, their wide applications are limited. Therefore, it is an important research direction in the field of 2D copper-based materials to improve the existing synthesis methods, put forward new modification theories, and develop various efficient synthesis technologies. In addition, apart from vacancies and heterojunctions, there has been only little exploration on the manipulation of the electronic structure. An emerging method for electrode synthesis and design is expected. Exploring 2D copper-based materials with precise size and controllable structure, such as various compounds or MOFs, can provide potential possibilities for energy conversion and storage. Experimental and theoretical methods are needed to rationalize and solve the problems of comprehensive design and electrode manufacturing in commercial applications. However, the mechanism of these modification methods has not yet been solved, especially the

relationship between modification and the electrochemical properties of 2D copper-based materials needs to be further discussed to guide its specific application.

For energy storage applications, at present, the energy density of SCs is improved by using battery-like materials, redox electrolyte, and designing asymmetric devices, but these methods often sacrifice their power characteristics and lose the essential characteristics of SCs. Therefore, how to effectively improve the mass/volume energy density on the premise of maintaining the rapid charge and discharge capacity is a topic that warrants future research efforts. 2D copper-based materials are mainly used in LIBs. Yet, they are approaching the basic limit of these batteries and cannot be further enhanced. In order to achieve a higher energy density, the research of so-called “beyond Li⁺” technologies should be encouraged.

For energy conversion applications, various 2D copper-based materials electrocatalysts in water splitting/metal-air batteries/CO₂RR have been widely developed. However, the research of 2D copper-based materials in the catalytic reaction is still at an early stage, because the research of electrocatalysis is a wide and complex field. Considering the current situation, they are not as good as the most advanced precious metal catalysts. In order to ensure their stability and catalytic performance, the surface electronic structure of 2D copper-based materials needs to be manipulated by boundary state, functional group, defect state, and monatomic load. Through various characterization methods and theoretical calculations, the confinement effect and heterostructures of 2D materials, as well as the intrinsic relationship between the microstructure and catalytic performance will be revealed. This is of great significance to further develop more efficient 2D copper-based electrocatalysts. In addition, there are many factors that affect their practical application, including media (pH), temperature, solvent, etc. Activity evaluation is mostly based on the simplified semi-reaction device. Future research should pay more attention to the performance of materials in actual fuel cells or electrolytic cell devices, which will help to promote the application in related fields.

To sum up, 2D copper-based materials and their composites play an increasingly important role in energy storage and conversion, but there is still a long way to go for their wide application. Yet, further research is needed on multiple fronts, such as simplification of synthesis process, rapid development of characterization technology, and improvement and uniqueness of performance.

Acknowledgements

This work was supported by the National Natural Science Foundation of China (No. 21676036), the Fundamental Research Funds for the Central Universities of Chongqing University (No. 2019CDXYHG0013), and the Large-scale Equipment Sharing Fund of Chongqing University (No. 202103150115).

Conflict of Interest

The authors declare no conflict of interest.

Keywords

2D copper-based materials, Cu-based metal-organic frameworks, electrocatalysis, metal-ion batteries, supercapacitors

Received: July 5, 2022

Revised: November 23, 2022

Published online: December 16, 2022

- [1] L. Li, S. Zhao, Z. Hu, S.-L. Chou, J. Chen, *Chem. Sci.* **2021**, *12*, 2345.
- [2] J. V. Vidal, V. Slabov, A. L. Kholkin, M. P. S. dos Santos, *Nano-Micro Lett.* **2021**, *13*, 199.
- [3] C. Li, D. Raciti, T. Pu, L. Cao, C. He, C. Wang, T. Mueller, *J. Phys. Chem. C* **2018**, *122*, 18040.
- [4] Y. Zhang, H.-x. Mei, Y. Cao, X.-h. Yan, J. Yan, H.-l. Gao, H.-w. Luo, S.-w. Wang, X.-d. Jia, L. Kachalova, J. Yang, S.-c. Xue, C.-g. Zhou, L.-x. Wang, Y.-h. Gui, *Coord. Chem. Rev.* **2021**, *438*, 213910.
- [5] Y. Liu, G. He, H. Jiang, I. P. Parkin, P. R. Shearing, D. J. L. Brett, *Adv. Funct. Mater.* **2021**, *31*, 2010445.
- [6] Z.-Y. Yu, Y. Duan, X.-Y. Feng, X. Yu, M.-R. Gao, S.-H. Yu, *Adv. Mater.* **2021**, *33*, 2007100.
- [7] Y. Wang, F. Chu, J. Zeng, Q. Wang, T. Naren, Y. Li, Y. Cheng, Y. Lei, F. Wu, *ACS Nano* **2021**, *15*, 210.
- [8] H. Xie, T. Wang, J. Liang, Q. Li, S. Sun, *Nano Today* **2018**, *21*, 41.
- [9] P. Xie, W. Yuan, X. Liu, Y. Peng, Y. Yin, Y. Li, Z. Wu, *Energy Storage Mater.* **2021**, *36*, 56.
- [10] W. Zhang, J. Yin, W. Wang, Z. Bayhan, H. N. Alshareef, *Nat. Energy* **2021**, *83*, 105792.
- [11] Y. Yan, B. Y. Xia, B. Zhao, X. Wang, *J. Mater. Chem. A* **2016**, *4*, 17587.
- [12] H.-F. Wang, Q. Xu, *Matter* **2019**, *1*, 565.
- [13] D. Gao, T. Liu, G. Wang, X. Bao, *ACS Energy Lett.* **2021**, *6*, 713.
- [14] G. Wang, J. Chen, Y. Ding, P. Cai, L. Yi, Y. Li, C. Tu, Y. Hou, Z. Wen, L. Dai, *Chem. Soc. Rev.* **2021**, *50*, 4993.
- [15] S. Yuan, S.-Y. Pang, J. Hao, *Appl. Phys. Rev.* **2020**, *7*, 021304.
- [16] F. Bonaccorso, L. Colombo, G. Yu, M. Stoller, V. Tozzini, C. Ferrari Andrea, S. Ruoff Rodney, V. Pellegrini, *Science* **2015**, *347*, 1246501.
- [17] C. Tan, X. Cao, X.-J. Wu, Q. He, J. Yang, X. Zhang, J. Chen, W. Zhao, S. Han, G.-H. Nam, M. Sindoro, H. Zhang, *Chem. Rev.* **2017**, *117*, 6225.
- [18] C. Tan, H. Zhang, *Nat. Commun.* **2015**, *6*, 7873.
- [19] Z. Zhang, K. Zhao, T.-R. Wei, P. Qiu, L. Chen, X. Shi, *Energy Environ. Sci.* **2020**, *13*, 3307.
- [20] W.-D. Liu, L. Yang, Z.-G. Chen, *Nano Today* **2020**, *35*, 100938.
- [21] Q. Zhang, K. Zhang, D. Xu, G. Yang, H. Huang, F. Nie, C. Liu, S. Yang, *Prog. Mater. Sci.* **2014**, *60*, 208.
- [22] X. Rui, H. Tan, Q. Yan, *Nanoscale* **2014**, *6*, 9889.
- [23] Y. Tashiro, K. Taniguchi, H. Miyasaka, *Electrochim. Acta* **2016**, *210*, 655.
- [24] C. Panda, P. W. Menezes, M. Zheng, S. Orthmann, M. Driess, *ACS Energy Lett.* **2019**, *4*, 747.
- [25] A. B. Laursen, K. U. D. Calvino, T. A. Goetjen, K. M. K. Yap, S. Hwang, H. Yang, E. Garfunkel, G. C. Dismukes, *Electrochim. Acta* **2021**, *391*, 138889.
- [26] K. Zhang, X. Han, Z. Hu, X. Zhang, Z. Tao, J. Chen, *Chem. Soc. Rev.* **2015**, *44*, 699.
- [27] G. Kalimuldina, A. Nurpeissova, A. Adylkhanova, D. Adair, I. Taniguchi, Z. Bakenov, *ACS Appl. Energy Mater.* **2020**, *3*, 11480.
- [28] Y. Chen, Z. Fan, Z. Zhang, W. Niu, C. Li, N. Yang, B. Chen, H. Zhang, *Chem. Rev.* **2018**, *118*, 6409.
- [29] M. Shekhirov, C. E. Shuck, A. Sarycheva, Y. Gogotsi, *Prog. Mater. Sci.* **2021**, *120*, 100757.
- [30] M. Mustaqem, G. A. Naikoo, F. Rahimi, M. Z. Pedram, H. Pourfarzad, I. U. Hassan, F. Arshad, Y.-F. Chen, *J. Energy Storage* **2022**, *51*, 104330.

- [31] M. B. Gawande, A. Goswami, F.-X. Felpin, T. Asefa, X. Huang, R. Silva, X. Zou, R. Zboril, R. S. Varma, *Chem. Rev.* **2016**, *116*, 3722.
- [32] S. Sun, X. Zhang, Q. Yang, S. Liang, X. Zhang, Z. Yang, *Prog. Mater. Sci.* **2018**, *96*, 111.
- [33] C. Gattinoni, A. Michaelides, *Surf. Sci. Rep.* **2015**, *70*, 424.
- [34] Z. Liu, X. Yuan, S. Zhang, J. Wang, Q. Huang, N. Yu, Y. Zhu, L. Fu, F. Wang, Y. Chen, Y. Wu, *NPG Asia Mater.* **2019**, *11*, 12.
- [35] G. Döring, C. Sternemann, A. Kaprolat, A. Mattila, K. Hämäläinen, W. Schülke, *Phys. Rev. B* **2004**, *70*, 085115.
- [36] X. Han, L. Wang, H. Ling, Z. Ge, X. Lin, X. Dai, H. Chen, *Renewable Sustainable Energy Rev.* **2022**, *158*, 112076.
- [37] Q. Xu, B. Huang, Y. Zhao, Y. Yan, R. Noufi, S.-H. Wei, *Appl. Phys. Lett.* **2012**, *100*, 061906.
- [38] A. E. Powell, J. M. Hodges, R. E. Schaak, *J. Am. Chem. Soc.* **2016**, *138*, 471.
- [39] A. Morales-García, A. L. Soares, E. C. Dos Santos, H. A. de Abreu, H. A. Duarte, *J. Phys. Chem. A* **2014**, *118*, 5823.
- [40] Y. Lu, B. Li, S. Zheng, Y. Xu, H. Xue, H. Pang, *Adv. Funct. Mater.* **2017**, *27*, 1703949.
- [41] M. Liu, Y. Liu, B. Gu, X. Wei, G. Xu, X. Wang, M. T. Swihart, K.-T. Yong, *Chem. Soc. Rev.* **2019**, *48*, 4950.
- [42] D. Majumdar, *J. Electroanal. Chem.* **2021**, *880*, 114825.
- [43] I. Grozdanov, M. Najdoski, *J. Solid State Chem.* **1995**, *114*, 469.
- [44] L.-W. Wang, *Phys. Rev. Lett.* **2012**, *108*, 085703.
- [45] A. M. Zardkhouhou, S. S. H. Davarani, *Chem. Eng. J.* **2020**, *402*, 126241.
- [46] J. Yu, K. Zhao, P. Qiu, X. Shi, L. Chen, *Ceram. Int.* **2017**, *43*, 11142.
- [47] E. Eikeland, A. B. Blichfeld, I. A. Borup, K. Zhao, J. Overgaard, X. Shi, L. Chen, B. B. Iversen, *IUCrJ* **2017**, *4*, 476.
- [48] A. Ścigała, E. Szlyk, L. Dobrzańska, D. H. Gregory, R. Szczyński, *Coord. Chem. Rev.* **2021**, *436*, 213791.
- [49] N. Yamada, K. Maruya, Y. Yamaguchi, X. Cao, Y. Ninomiya, *Chem. Mater.* **2015**, *27*, 8076.
- [50] A. Wolff, T. Doert, J. Hunger, M. Kaiser, J. Pallmann, R. Reinhold, S. Yogendra, L. Giebeler, J. Sichelschmidt, W. Schnelle, R. Whiteside, H. Q. N. Gunaratne, P. Nockemann, J. J. Weigand, E. Brunner, M. Ruck, *Chem. Mater.* **2018**, *30*, 7111.
- [51] X. Zhao, L. Mao, Q. Cheng, J. Li, F. Liao, G. Yang, L. Xie, C. Zhao, L. Chen, *Chem. Eng. J.* **2020**, *387*, 124081.
- [52] Z. Zhuang, Q. Peng, Y. Li, *Chem. Soc. Rev.* **2011**, *40*, 5492.
- [53] T. Wang, X. Zhang, X. Zhu, Q. Liu, S. Lu, A. M. Asiri, Y. Luo, X. Sun, *Nanoscale* **2020**, *12*, 5359.
- [54] H. Bai, H. Guo, J. Wang, Y. Dong, B. Liu, Z. Xie, F. Guo, D. Chen, R. Zhang, Y. Zheng, *Sens. Actuators, B* **2021**, *337*, 129783.
- [55] J. Singh, S. Juneja, R. K. Soni, J. Bhattacharya, *J. Colloid Interface Sci.* **2021**, *590*, 60.
- [56] X. P. Gao, J. L. Bao, G. L. Pan, H. Y. Zhu, P. X. Huang, F. Wu, D. Y. Song, *J. Phys. Chem. B* **2004**, *108*, 5547.
- [57] H. Ning, Y. Zeng, S. Zuo, S. V. Kershaw, Y. Hou, Y. Li, X. Li, J. Zhang, Y. Yi, L. Jing, J. Li, M. Gao, *ACS Nano* **2021**, *15*, 873.
- [58] M. Kumar, A. Olajire Oyedun, A. Kumar, *Renewable Sustainable Energy Rev.* **2018**, *81*, 1742.
- [59] J. Demel, A. Zhigunov, I. Jirka, M. Klementová, K. Lang, *J. Colloid Interface Sci.* **2015**, *452*, 174.
- [60] R. Suresh Babu, R. Vinodh, A. L. F. de Barros, L. M. Samyn, K. Prasanna, M. A. Maier, C. H. F. Alves, H.-J. Kim, *Chem. Eng. J.* **2019**, *366*, 390.
- [61] Q. Gao, J. Wang, J. Wang, *J. Alloys Compd.* **2019**, *789*, 193.
- [62] A. T. Aqueel Ahmed, B. Hou, H. S. Chavan, Y. Jo, S. Cho, J. Kim, S. M. Pawar, S. Cha, A. I. Inamdar, H. Kim, H. Im, *Small* **2018**, *14*, 1800742.
- [63] X. Liu, F. Xu, Z. Li, Z. Liu, W. Yang, Y. Zhang, H. Fan, H. Y. Yang, *Coord. Chem. Rev.* **2022**, *464*, 214544.
- [64] A. E. Danks, S. R. Hall, Z. Schnepf, *Mater. Horiz.* **2016**, *3*, 91.
- [65] H.-Y. Chen, J.-H. Chen, *Mater. Lett.* **2017**, *188*, 63.
- [66] M. W. Kadi, R. M. Mohamed, *Appl. Nanosci.* **2020**, *10*, 4291.
- [67] V. Usha, S. Kalyanaraman, R. Thangavel, R. Vettumperumal, *Superlattices Microstruct.* **2015**, *86*, 203.
- [68] B. Yuan, X. Liu, J. Liu, M. Li, D. Wang, *Mater. Lett.* **2019**, *236*, 495.
- [69] Q. Liu, J. Zhu, L. Zhang, Y. Qiu, *Renewable Sustainable Energy Rev.* **2018**, *81*, 1825.
- [70] B. Sun, Y. Z. Long, H. D. Zhang, M. M. Li, J. L. Duvail, X. Y. Jiang, H. L. Yin, *Prog. Polym. Sci.* **2014**, *39*, 862.
- [71] Y. Lu, Y. Wang, S. Cui, W. Chen, L. Mi, *RSC Adv.* **2018**, *8*, 40589.
- [72] X. Zhang, X. Liu, Y. Zhang, R. Bao, D. Peng, T. Li, G. Gao, W. Guo, C. Pan, *J. Mater. Chem. C* **2016**, *4*, 8130.
- [73] C. Zhang, D. Wei, F. Wang, G. Zhang, J. Duan, F. Han, H. Duan, J. Liu, *J. Energy Chem.* **2021**, *53*, 26.
- [74] M. S. Pradeepkumar, H. V. Singh, S. Kumar, J. Basu, M. I. Ahmad, *Mater. Lett.* **2020**, *280*, 128560.
- [75] V. Sudha, K. Krishnamoorthy, S. M. Senthil Kumar, R. Thangamuthu, *J. Alloys Compd.* **2018**, *764*, 959.
- [76] D. P. Dubal, G. S. Gund, R. Holze, C. D. Lokhande, *J. Power Sources* **2013**, *242*, 687.
- [77] C. Venkata Thulasi-Varma, S. S. Rao, C. S. S. P. Kumar, C. V. V. M. Gopi, I. K. Durga, S.-K. Kim, D. Punnoose, H.-J. Kim, *John Dalton Prog. Sci., Pap. Conf. Hist. Sci.* **2015**, *44*, 19330.
- [78] S. K. Shinde, H. M. Yadav, G. S. Ghodake, A. A. Kadam, V. S. Kumbhar, J. Yang, K. Hwang, A. D. Jagdale, S. Kumar, D. Y. Kim, *Colloids Surf., B* **2019**, *181*, 1004.
- [79] L. M. Xie, *Nanoscale* **2015**, *7*, 18392.
- [80] Y. Fu, Q. Li, J. Liu, Y. Jiao, S. Hu, H. Wang, S. Xu, B. Jiang, *J. Colloid Interface Sci.* **2020**, *570*, 143.
- [81] K. Jin, M. Zhou, H. Zhao, S. Zhai, F. Ge, Y. Zhao, Z. Cai, *Electrochim. Acta* **2019**, *295*, 668.
- [82] T. D. Raju, A. Gopalakrishnan, S. Badhulika, *J. Alloys Compd.* **2020**, *845*, 156241.
- [83] G. H. Kim, Y. S. Park, J. Yang, M. J. Jang, J. Jeong, J.-H. Lee, H.-S. Park, Y. H. Park, S. M. Choi, J. Lee, *Nanomaterials* **2021**, *11*, 657.
- [84] E. S. Goda, S. E. Hong, K. R. Yoon, *J. Alloys Compd.* **2021**, *859*, 157868.
- [85] D. Majumdar, S. Ghosh, *J. Energy Storage* **2021**, *34*, 101995.
- [86] S. K. Shinde, G. S. Ghodake, V. J. Fulari, D. Y. Kim, *J. Ind. Eng. Chem.* **2017**, *52*, 12.
- [87] N. Kapuria, N. N. Patil, K. M. Ryan, S. Singh, *Nanoscale* **2022**, *14*, 2885.
- [88] S. Vikulov, F. Di Stasio, L. Ceseracciu, P. L. Saldanha, A. Scarpellini, Z. Dang, R. Krahne, L. Manna, V. Lesnyak, *Adv. Funct. Mater.* **2016**, *26*, 3670.
- [89] Y.-Q. Liu, H.-D. Wu, Y. Zhao, G.-B. Pan, *Langmuir* **2015**, *31*, 4958.
- [90] W. van der Stam, F. T. Rabouw, J. J. Geuchies, A. C. Berends, S. O. M. Hinterding, R. G. Geitenbeek, J. van der Lit, S. Prévost, A. V. Petukhov, C. de Mello Donega, *Chem. Mater.* **2016**, *28*, 6381.
- [91] Y. Zhang, L. Tao, C. Xie, D. Wang, Y. Zou, R. Chen, Y. Wang, C. Jia, S. Wang, *Adv. Mater.* **2020**, *32*, 1905923.
- [92] W. Li, D. Wang, Y. Zhang, L. Tao, T. Wang, Y. Zou, Y. Wang, R. Chen, S. Wang, *Adv. Mater.* **2020**, *32*, 1907879.
- [93] K. Li, Y. Ye, W. Zhang, Y. Hu, Y. Yang, Y. Zhou, C. Liu, *J. Mater. Chem. C* **2021**, *9*, 11261.
- [94] G. Durai, P. Kuppusami, S. Arulmani, S. Anandan, S. Khadeer Pasha, S. Kheawhom, *Int. J. Energy Res.* **2021**, *45*, 20001.
- [95] H. Yi, S. Liu, C. Lai, G. Zeng, M. Li, X. Liu, B. Li, X. Huo, L. Qin, L. Li, M. Zhang, Y. Fu, Z. An, L. Chen, *Adv. Energy Mater.* **2021**, *11*, 2002863.
- [96] J. Ma, F. Zhu, P. Ji, Q. Zou, H. Wang, G. Xu, *J. Alloys Compd.* **2021**, *863*, 158612.
- [97] W. Zhang, L. Ding, W. Sun, Z. Wu, Z. Chen, F. Gao, *Inorg. Chem.* **2021**, *60*, 14371.

- [98] H. Zhou, B. Xiong, L. Chen, J. Shi, *J. Mater. Chem. A* **2020**, *8*, 20286.
- [99] F. Bai, L. Xu, X. Zhai, X. Chen, W. Yang, *Adv. Energy Mater.* **2020**, *10*, 1902107.
- [100] T. Xiong, Z. G. Yu, H. Wu, Y. Du, Q. Xie, J. Chen, Y.-W. Zhang, S. J. Pennycook, W. S. V. Lee, J. Xue, *Adv. Energy Mater.* **2019**, *9*, 1803815.
- [101] Q. Xia, H. Liu, X. S. Zhao, *J. Mater. Chem. A* **2022**, *10*, 3889.
- [102] Z. Su, J. Liu, M. Li, Y. Zhu, S. Qian, M. Weng, J. Zheng, Y. Zhong, F. Pan, S. Zhang, *Electrochem. Eng. Energy* **2020**, *3*, 286.
- [103] L. Liang, K.-Y. Niu, L. Zhang, J. Tian, K. Zhou, X.-L. Wang, X.-M. Zhang, M. Hong, *ACS Appl. Nano Mater.* **2021**, *4*, 6135.
- [104] S. Mo, Y. Song, M. Lin, J. Wang, Z. Zhang, J. Sun, D. Guo, L. Liu, *J. Colloid Interface Sci.* **2022**, *608*, 2896.
- [105] X. Li, Y. Sun, J. Xu, Y. Shao, J. Wu, X. Xu, Y. Pan, H. Ju, J. Zhu, Y. Xie, *Nat. Energy* **2019**, *4*, 690.
- [106] C. Peng, G. Luo, J. Zhang, M. Chen, Z. Wang, T.-K. Sham, L. Zhang, Y. Li, G. Zheng, *Nat. Commun.* **2021**, *12*, 1580.
- [107] L. Kang, C. Huang, J. Zhang, M. Zhang, N. Zhang, S. Liu, Y. Ye, C. Luo, Z. Gong, C. Wang, X. Zhou, X. Wu, S. C. Jun, *Chem. Eng. J.* **2020**, *390*, 124643.
- [108] S. Back, S. Siahrostami, *Nanoscale Adv.* **2019**, *1*, 132.
- [109] K. Yao, Z. Xu, J. Huang, M. Ma, L. Fu, X. Shen, J. Li, M. Fu, *Small* **2019**, *15*, 1805405.
- [110] X. Zhang, X. Liu, Y. Zeng, Y. Tong, X. Lu, *Small Methods* **2020**, *4*, 1900823.
- [111] G. Wang, Y. Yang, D. Han, Y. Li, *Nano Today* **2017**, *13*, 23.
- [112] M.-Q. Yang, J. Wang, H. Wu, G. W. Ho, *Small* **2018**, *14*, 1703323.
- [113] Z. Deng, Z. Ma, Y. Li, Y. Li, L. Chen, X. Yang, H.-E. Wang, B.-L. Su, *Front. Chem.* **2018**, *6*, 428.
- [114] Y. Zhu, L. Peng, Z. Fang, C. Yan, X. Zhang, G. Yu, *Adv. Mater.* **2018**, *30*, 1706347.
- [115] B. You, X. Liu, G. Hu, S. Gul, J. Yano, D.-e. Jiang, Y. Sun, *J. Am. Chem. Soc.* **2017**, *139*, 12283.
- [116] H. Ju, X. D. Liu, C. Y. Tao, F. Yang, X. L. Liu, X. Luo, L. Zhang, *Electrochim. Acta* **2021**, *366*, 137410.
- [117] H. Zhao, Z.-Y. Yuan, *J. Energy Chem.* **2021**, *54*, 89.
- [118] B.-B. Chen, D.-K. Ma, Q.-P. Ke, W. Chen, S.-M. Huang, *Phys. Chem. Chem. Phys.* **2016**, *18*, 6713.
- [119] S. Chen, S. Cui, S. Chandrasekaran, C. Ke, Z. Li, P. Chen, C. Zhang, Y. Jiang, *Electrochim. Acta* **2020**, *341*, 135893.
- [120] X. Sun, H. Deng, W. Zhu, Z. Yu, C. Wu, Y. Xie, *Angew. Chem., Int. Ed.* **2016**, *55*, 1704.
- [121] S. Cheng, K. Yao, K. Zheng, Q. Li, D. Chen, Y. Jiang, W. Liu, Y. Feng, X. Rui, Y. Yu, *Energy Environ. Mater.* **2022**, *5*, 592.
- [122] H.-J. Yin, K. Yuan, Y.-L. Zheng, X.-C. Sun, Y.-W. Zhang, *J. Phys. Chem. C* **2021**, *125*, 16516.
- [123] X. Wang, J. Lv, J. Zhang, X.-L. Wang, C. Xue, G. Bian, D. Li, Y. Wang, T. Wu, *Nanoscale* **2020**, *12*, 772.
- [124] H. N. Jia, J. H. Lin, Y. L. Liu, S. L. Chen, Y. F. Cai, J. L. Qi, J. C. Feng, W.-D. Fei, *J. Mater. Chem. A* **2017**, *5*, 10678.
- [125] J. Wang, Q. Zhang, X. Li, D. Xu, Z. Wang, H. Guo, K. Zhang, *Nat. Energy* **2014**, *6*, 19.
- [126] D. Zhu, X. Sun, J. Yu, Q. Liu, J. Liu, R. Chen, H. Zhang, R. Li, J. Yu, J. Wang, *J. Colloid Interface Sci.* **2019**, *557*, 76.
- [127] J. Liu, M. Wang, M. C. Dipalo, J. Zhuang, W. Shi, X. Wang, *Chem. Sci.* **2021**, *12*, 11490.
- [128] L. Wu, L. Sun, X. Li, Q. Zhang, Y. Zhang, J. Gu, K. Wang, Y. Zhang, *Small* **2020**, *16*, 2001468.
- [129] X. Zhang, W. Shi, J. Zhu, D. J. Kharistal, W. Zhao, B. S. Lalia, H. H. Hng, Q. Yan, *ACS Nano* **2011**, *5*, 2013.
- [130] H. Li, Z. Li, Z. Wu, M. Sun, S. Han, C. Cai, W. Shen, X. Liu, Y. Fu, *J. Colloid Interface Sci.* **2019**, *549*, 105.
- [131] R. Wang, X.-Y. Dong, J. Du, J.-Y. Zhao, S.-Q. Zang, *Adv. Mater.* **2018**, *30*, 1703711.
- [132] X. Li, K. Zhou, J. Zhou, J. Shen, M. Ye, *J. Mater. Sci. Technol.* **2018**, *34*, 2342.
- [133] S. D. Jagdale, A. M. Teli, S. V. Kalake, A. D. Sawant, A. A. Yadav, P. S. Patil, *J. Electroanal. Chem.* **2018**, *816*, 99.
- [134] H.-J. Shin, S. M. Kim, S.-M. Yoon, A. Benayad, K. K. Kim, S. J. Kim, H. K. Park, J.-Y. Choi, Y. H. Lee, *J. Am. Chem. Soc.* **2008**, *130*, 2062.
- [135] J. Liu, J. Tang, J. J. Gooding, *J. Mater. Chem.* **2012**, *22*, 12435.
- [136] D. Chen, Y. Zou, S. Wang, *Mater. Today Energy* **2019**, *12*, 250.
- [137] Y. Li, X. Jiang, Z. Fu, Q. Huang, G.-E. Wang, W.-H. Deng, C. Wang, Z. Li, W. Yin, B. Chen, G. Xu, *Nat. Commun.* **2020**, *11*, 261.
- [138] G.-N. Liu, R.-D. Xu, M.-K. Li, Y. Sun, M.-J. Zhou, R.-Y. Cai, Z.-J. You, X.-M. Jiang, C. Li, *Chem. Commun.* **2022**, *58*, 2858.
- [139] J. He, B. Hu, Y. Zhao, *Adv. Funct. Mater.* **2016**, *26*, 5998.
- [140] P. Wang, T. Hayashi, Q. a. Meng, Q. Wang, H. Liu, K. Hashimoto, L. Jiang, *Small* **2017**, *13*, 1601250.
- [141] Z. Lu, W. Xu, J. Ma, Y. Li, X. Sun, L. Jiang, *Adv. Mater.* **2016**, *28*, 7155.
- [142] W. Xu, Z. Lu, X. Sun, L. Jiang, X. Duan, *Acc. Chem. Res.* **2018**, *51*, 1590.
- [143] Y.-I. Yao, J.-m. He, X. Yang, L. Peng, X.-d. Zhu, K.-s. Li, M.-n. Qu, *Colloids Surf., A* **2022**, *634*, 127934.
- [144] Y. Shao, M. F. El-Kady, J. Sun, Y. Li, Q. Zhang, M. Zhu, H. Wang, B. Dunn, R. B. Kaner, *Chem. Rev.* **2018**, *118*, 9233.
- [145] C. Zhong, Y. Deng, W. Hu, J. Qiao, L. Zhang, J. Zhang, *Chem. Soc. Rev.* **2015**, *44*, 7484.
- [146] M. S. Javed, N. Shaheen, S. Hussain, J. Li, S. S. A. Shah, Y. Abbas, M. A. Ahmad, R. Raza, W. Mai, *J. Mater. Chem. A* **2019**, *7*, 946.
- [147] R. R. Salunkhe, Y. V. Kaneti, Y. Yamauchi, *ACS Nano* **2017**, *11*, 5293.
- [148] K. Wang, C. Zhao, S. Min, X. Qian, *Electrochim. Acta* **2015**, *165*, 314.
- [149] K. S. Kumar, N. Choudhary, Y. Jung, J. Thomas, *ACS Energy Lett.* **2018**, *3*, 482.
- [150] D. He, S. Xing, B. Sun, H. Cai, H. Suo, C. Zhao, *Electrochim. Acta* **2016**, *210*, 639.
- [151] Y. Lu, X. Liu, K. Qiu, J. Cheng, W. Wang, H. Yan, C. Tang, J.-K. Kim, Y. Luo, *ACS Appl. Mater. Interfaces* **2015**, *7*, 9682.
- [152] A. C. Nwanya, D. Obi, K. I. Ozoemena, R. U. Osuji, C. Awada, A. Ruediger, M. Maaza, F. Rosei, F. I. Ezema, *Electrochim. Acta* **2016**, *198*, 220.
- [153] C. An, Z. Wang, W. Xi, K. Wang, X. Liu, Y. Ding, *J. Mater. Chem. A* **2019**, *7*, 15691.
- [154] C. J. Raj, M. Rajesh, R. Manikandan, W.-g. Lee, K. H. Yu, B. C. Kim, *J. Alloys Compd.* **2018**, *735*, 2378.
- [155] C. Justin Raj, B. C. Kim, W.-J. Cho, W.-G. Lee, Y. Seo, K.-H. Yu, *J. Alloys Compd.* **2014**, *586*, 191.
- [156] W. Xu, Y. Liang, Y. Su, S. Zhu, Z. Cui, X. Yang, A. Inoue, Q. Wei, C. Liang, *Electrochim. Acta* **2016**, *211*, 891.
- [157] S. Liu, K. S. Hui, K. N. Hui, *ACS Appl. Mater. Interfaces* **2016**, *8*, 3258.
- [158] S. Liu, Y. Yin, K. S. Hui, K. N. Hui, S. C. Lee, S. C. Jun, *Adv. Sci.* **2018**, *5*, 1800733.
- [159] G. Wang, J. Huang, S. Chen, Y. Gao, D. Cao, *J. Power Sources* **2011**, *196*, 5756.
- [160] S. K. Shinde, D. Y. Kim, G. S. Ghodake, N. C. Maile, A. A. Kadam, D. S. Lee, M. C. Rath, V. J. Fulari, *Ultrason. Sonochem.* **2018**, *40*, 314.
- [161] B. K. Singh, A. Shaikh, R. O. Dusane, S. Parida, *J. Energy Storage* **2020**, *31*, 101631.
- [162] Y. Zhan, J. Bai, F. Guo, H. Zhou, R. Shu, Y. Yu, L. Qian, *J. Alloys Compd.* **2021**, *885*, 161014.
- [163] B. Zhao, P. Liu, H. Zhuang, Z. Jiao, T. Fang, W. Xu, B. Lu, Y. Jiang, *J. Mater. Chem. A* **2013**, *1*, 367.
- [164] Y. Liu, H. Huang, X. Peng, *Electrochim. Acta* **2013**, *104*, 289.
- [165] M. G. T. N. D., J. M. B. S., P. Basu, M. R. H. S., S. Joseph, S. P., *Appl. Surf. Sci.* **2018**, *449*, 474.

- [166] A. Ghosh, M. Miah, A. Bera, S. K. Saha, B. Ghosh, *J. Alloys Compd.* **2021**, 862, 158549.
- [167] I. Hussain, T. Hussain, S. Yang, Y. Chen, J. Zhou, X. Ma, N. Abbas, C. Lamiel, K. Zhang, *Chem. Eng. J.* **2021**, 413, 127570.
- [168] Z. Hu, X. Xiao, L. Huang, C. Chen, T. Li, T. Su, X. Cheng, L. Miao, Y. Zhang, J. Zhou, *Nanoscale* **2015**, 7, 16094.
- [169] J. S. Shaikh, R. C. Pawar, R. S. Devan, Y. R. Ma, P. P. Salvi, S. S. Kolekar, P. S. Patil, *Electrochim. Acta* **2011**, 56, 2127.
- [170] J. Huang, H. Wu, D. Cao, G. Wang, *Electrochim. Acta* **2012**, 75, 208.
- [171] W. Lv, L. Li, Q. Meng, X. Zhang, *J. Mater. Sci.* **2020**, 55, 2492.
- [172] Y. Guo, X. Hong, Y. Wang, Q. Li, J. Meng, R. Dai, X. Liu, L. He, L. Mai, *Adv. Funct. Mater.* **2019**, 29, 1809004.
- [173] S. Wu, W. Lv, T. Lei, Y. Han, X. Jian, M. Deng, G. Zhu, M. Liu, J. Xiong, J. H. Dickerson, W. He, *Adv. Energy Mater.* **2017**, 7, 1700105.
- [174] Y. Li, S. Chang, X. Liu, J. Huang, J. Yin, G. Wang, D. Cao, *Electrochim. Acta* **2012**, 85, 393.
- [175] P. Liu, K. Qin, S. Wen, L. Wang, F. He, E. Liu, C. He, C. Shi, J. Li, Q. Li, L. Ma, N. Zhao, *Electrochim. Acta* **2018**, 283, 970.
- [176] D. Du, R. Lan, W. Xu, R. Beanland, H. Wang, S. Tao, *J. Mater. Chem. A* **2016**, 4, 17749.
- [177] D. He, G. Wang, G. Liu, H. Suo, C. Zhao, *John Dalton Prog. Sci., Pap. Conf. Hist. Sci.* **2017**, 46, 3318.
- [178] L. Xu, J. Li, H. Sun, X. Guo, J. Xu, H. Zhang, X. Zhang, *Front. Chem.* **2019**, 7, 420.
- [179] K. V. Gurav, U. M. Patil, S. W. Shin, G. L. Agawane, M. P. Suryawanshi, S. M. Pawar, P. S. Patil, C. D. Lokhande, J. H. Kim, *J. Alloys Compd.* **2013**, 573, 27.
- [180] R. N. Bulakhe, V. Q. Nguyen, D. Tuma, Y. R. Lee, H. Zhang, S. Zhang, J.-J. Shim, *J. Ind. Eng. Chem.* **2018**, 66, 288.
- [181] Q. Wang, D. O'Hare, *Chem. Rev.* **2012**, 112, 4124.
- [182] S. P. Adhikari, G. P. Awasthi, K.-S. Kim, C. H. Park, C. S. Kim, *John Dalton Prog. Sci., Pap. Conf. Hist. Sci.* **2018**, 47, 4455.
- [183] L. Zhang, H. Gong, *Electrochim. Acta* **2017**, 234, 82.
- [184] T. Wang, S. Zhang, H. Wang, *Sci. China Mater.* **2018**, 61, 296.
- [185] J. Huang, J. Xie, L. Wang, J. Zhang, P. Wang, P. Sun, Z. Yao, Y. Yang, *Energy Fuels* **2020**, 34, 13157.
- [186] X. Li, D. Du, Y. Zhang, W. Xing, Q. Xue, Z. Yan, *J. Mater. Chem. A* **2017**, 5, 15460.
- [187] L. Kumar, P. K. Boruah, S. Borthakur, L. Saikia, M. R. Das, S. Deka, *ACS Appl. Nano Mater.* **2021**, 4, 5250.
- [188] K. Xu, S. Ma, Y. Shen, Q. Ren, J. Yang, X. Chen, J. Hu, *Chem. Eng. J.* **2019**, 369, 363.
- [189] P. Liang, F. Wang, Z.-A. Hu, *Chem. Eng. J.* **2018**, 350, 627.
- [190] Y. Liu, X. Chang, M. Wang, H. Guo, W. Li, Y. Wang, *J. Alloys Compd.* **2021**, 871, 159555.
- [191] S. Liu, K. San Hui, K. N. Hui, J. M. Yun, K. H. Kim, *J. Mater. Chem. A* **2016**, 4, 8061.
- [192] K. Chanda, S. Maiti, S. Sarkar, P. Bairi, S. Thakur, K. Sardar, N. Besra, N. S. Das, K. K. Chattopadhyay, *ACS Appl. Nano Mater.* **2021**, 4, 1420.
- [193] L. Abbasi, M. Arvand, *Appl. Surf. Sci.* **2018**, 445, 272.
- [194] S. M. Pawar, B. S. Pawar, P. T. Babar, A. T. A. Ahmed, H. S. Chavan, Y. Jo, S. Cho, J. Kim, B. Hou, A. I. Inamdar, S. Cha, J. H. Kim, T. G. Kim, H. Kim, H. Im, *Appl. Surf. Sci.* **2019**, 470, 360.
- [195] S. K. Shinde, S. S. Karade, N. C. Maile, H. M. Yadav, G. S. Ghodake, A. D. Jagadale, D.-Y. Kim, *J. Mol. Liq.* **2021**, 334, 116390.
- [196] K.-J. Huang, J.-Z. Zhang, Y. Fan, *J. Alloys Compd.* **2015**, 625, 158.
- [197] M. Naveed, W. Younas, Y. Zhu, S. Rafai, Q. Zhao, M. Tahir, N. Mushtaq, C. Cao, *Electrochim. Acta* **2019**, 319, 49.
- [198] H. Liu, Z. Guo, X. Wang, J. Hao, J. Lian, *Electrochim. Acta* **2018**, 271, 425.
- [199] B. N. Reddy, G. Gupta, P. P. Ingole, *ChemistrySelect* **2018**, 3, 11293.
- [200] P. Naveenkumar, G. P. Kalaignan, *New J. Chem.* **2019**, 43, 12785.
- [201] J. Lin, H. Jia, H. Liang, S. Chen, Y. Cai, J. Qi, C. Qu, J. Cao, W. Fei, J. Feng, *Chem. Eng. J.* **2018**, 336, 2259.
- [202] X. Yang, H. Sun, P. Zan, L. Zhao, J. Lian, *J. Mater. Chem. A* **2016**, 4, 18857.
- [203] W. Xu, J. Lu, W. Huo, J. Li, X. Wang, C. Zhang, X. Gu, C. Hu, *Nanoscale* **2018**, 10, 14304.
- [204] X. Yin, H. Chen, C. Zhi, W. Sun, L.-P. Lv, Y. Wang, *Small* **2018**, 14, 1800589.
- [205] Y. Huang, L. Lin, T. Shi, S. Cheng, Y. Zhong, C. Chen, Z. Tang, *Appl. Surf. Sci.* **2019**, 463, 498.
- [206] J. Jiang, Y. Chen, X. Hu, H. Cong, Q. Zhou, H. Rong, Y. Sun, S. Han, *Vacuum* **2020**, 182, 109698.
- [207] M. Abuali, N. Arsalani, I. Ahadzadeh, *J. Energy Storage* **2020**, 32, 101694.
- [208] B. Yang, L. Wang, J. Han, Y. Zhou, H. Song, S. Chen, J. Zhong, L. Lv, D. Niu, J. Tang, *Chem. Mater.* **2014**, 26, 3135.
- [209] K. Ramasamy, R. K. Gupta, H. Sims, S. Palchoudhury, S. Ivanov, A. Gupta, *J. Mater. Chem. A* **2015**, 3, 13263.
- [210] V. K. Mariappan, K. Krishnamoorthy, P. Pazhamalai, S. Sahoo, S.-J. Kim, *Electrochim. Acta* **2018**, 275, 110.
- [211] E. Scalise, M. Houssa, G. Pourtois, V. Afanas'ev, A. Stesmans, *Nano Res.* **2012**, 5, 43.
- [212] X. Hu, W. Shao, X. Hang, X. Zhang, W. Zhu, Y. Xie, *Angew. Chem., Int. Ed.* **2016**, 55, 5733.
- [213] P. Pazhamalai, K. Krishnamoorthy, S. Sahoo, V. K. Mariappan, S. J. Kim, *Chem. Eng. J.* **2019**, 359, 409.
- [214] K. Karuppasamy, D. Vikraman, S. Hussain, G. Kumar Veerasubramani, P. Santhoshkumar, S.-H. Lee, R. Bose, A. Kathalingam, H.-S. Kim, *Chem. Eng. J.* **2022**, 427, 131535.
- [215] Y. Zhu, H. Tang, X. Yun, L. Xi, Z. Hu, *J. Alloys Compd.* **2021**, 866, 158972.
- [216] J. Gong, Y. Tian, Z. Yang, Q. Wang, X. Hong, Q. Ding, *J. Phys. Chem. C* **2018**, 122, 2002.
- [217] A. Li, M. Zhai, M. Luan, J. Hu, *Chemistry* **2021**, 27, 10134.
- [218] J. Gong, J.-C. Li, J. Yang, S. Zhao, Z. Yang, K. Zhang, J. Bao, H. Pang, M. Han, *ACS Appl. Mater. Interfaces* **2018**, 10, 38341.
- [219] J.-C. Li, J. Gong, Z. Yang, Y. Tian, X. Zhang, Q. Wang, X. Hong, *J. Phys. Chem. C* **2019**, 123, 29133.
- [220] J.-C. Li, J. Gong, X. Zhang, L. Lu, F. Liu, Z. Dai, Q. Wang, X. Hong, H. Pang, M. Han, *ACS Appl. Energy Mater.* **2020**, 3, 3692.
- [221] Y.-f. Deng, Y. Chen, X.-l. Zhang, Q. Zhang, Z.-j. Wei, D. Wang, *J. Alloys Compd.* **2022**, 892, 162159.
- [222] W. Zhao, W. Wang, J. Peng, T. Chen, B. Jin, S. Liu, W. Huang, Q. Zhao, *John Dalton Prog. Sci., Pap. Conf. Hist. Sci.* **2019**, 48, 9631.
- [223] E. Irandoost, H. Farsi, A. Farrokhi, *Electrochim. Acta* **2021**, 368, 137616.
- [224] P. Sun, J. Zhang, J. Huang, L. Wang, P. Wang, C. Cai, M. Lu, Z. Yao, Y. Yang, *Mater. Res. Bull.* **2021**, 137, 111196.
- [225] T. R. Cook, Y.-R. Zheng, P. J. Stang, *Chem. Rev.* **2013**, 113, 734.
- [226] J. Xu, Y. Wang, S. Cao, J. Zhang, G. Zhang, H. Xue, Q. Xu, H. Pang, *J. Mater. Chem. A* **2018**, 6, 17329.
- [227] W. Bai, S. Li, J. Ma, W. Cao, J. Zheng, *J. Mater. Chem. A* **2019**, 7, 9086.
- [228] T. Deng, X. Shi, W. Zhang, Z. Wang, W. Zheng, *iScience* **2020**, 23, 101220.
- [229] T. Yue, R. Hou, X. Liu, K. Qi, Z. Chen, Y. Qiu, X. Guo, B. Y. Xia, *ACS Appl. Energy Mater.* **2020**, 3, 11920.
- [230] A. Bahaa, J. Balamurugan, N. H. Kim, J. H. Lee, *J. Mater. Chem. A* **2019**, 7, 8620.
- [231] C. Huang, C. Hao, Z. Ye, S. Zhou, X. Wang, L. Zhu, J. Wu, *Nanoscale* **2019**, 11, 10114.
- [232] Y. Zhao, C. Huang, Y. He, X. Wu, R. Ge, X. Zu, S. Li, L. Qiao, *J. Power Sources* **2020**, 456, 228023.

- [233] N. Wu, H. Wu, J. Zhang, Y. Zang, D. Cao, L. Bai, T. Hu, *J. Alloys Compd.* **2021**, 856, 157466.
- [234] [CrossRef]234 Z.-X. Li, B.-L. Yang, K.-Y. Zou, L. Kong, M.-L. Yue, H.-H. Duan, *Carbon* **2019**, 144, 5408.
- [235] P. A. Shinde, S. Park, N. R. Chodankar, S. Park, Y.-K. Han, A. G. Olabi, S. C. Jun, *Appl. Mater. Today* **2021**, 22, 100951.
- [236] Y.-C. Chen, Z.-B. Chen, Y.-G. Lin, Y.-K. Hsu, *ACS Sustainable Chem. Eng.* **2017**, 5, 3863.
- [237] G. K. Sharma, B. Ranjan, D. Kaur, *Appl. Phys. Lett.* **2021**, 118, 203901.
- [238] J. Meng, Z. Yang, L. Chen, H. Qin, F. Cui, Y. Jiang, X. Zeng, *Mater. Today Energy* **2020**, 15, 100370.
- [239] F. Wu, J. Maier, Y. Yu, *Chem. Soc. Rev.* **2020**, 49, 1569.
- [240] Q. Li, H. Pan, W. Li, Y. Wang, J. Wang, J. Zheng, X. Yu, H. Li, L. Chen, *ACS Energy Lett.* **2018**, 3, 2259.
- [241] N. M. Ncube, H. Zheng, *Mater. Res. Express* **2020**, 7, 015504.
- [242] D. Chen, G. Chen, R. Jin, H. Xu, *CrystEngComm* **2014**, 16, 2810.
- [243] J. Mei, T. Liao, Z. Sun, *J. Energy Chem.* **2018**, 27, 117.
- [244] Z. Li, G. Li, W. Xu, M. Zhou, C. Xu, M. Shi, F. Li, L. Chen, B. He, *ChemElectroChem* **2018**, 5, 2774.
- [245] Y. Ali, S. Lee, *Int. J. Energy Res.* **2022**, 46, 3017.
- [246] Y. Zhang, L. Huang, X. Zhou, Y. Luo, Q. Chen, Y. Chen, *J. Alloys Compd.* **2021**, 881, 160536.
- [247] Z. Li, Q. He, C. Zhou, Y. Li, Z. Liu, X. Hong, X. Xu, Y. Zhao, L. Mai, *Energy Storage Mater.* **2021**, 37, 40.
- [248] R. Deshmukh, G. Zeng, E. Tervoort, M. Staniuk, D. Wood, M. Niederberger, *Chem. Mater.* **2015**, 27, 8282.
- [249] D. Lee, S. Sun, J. Kwon, H. Park, M. Jang, E. Park, B. Son, Y. Jung, T. Song, U. Paik, *Adv. Mater.* **2020**, 32, 1905573.
- [250] F. Poli, A. Wong, J. S. Kshetrimayum, L. Monconduit, M. Letellier, *Chem. Mater.* **2016**, 28, 1787.
- [251] D. Ji, H. Zhou, Y. Tong, J. Wang, M. Zhu, T. Chen, A. Yuan, *Chem. Eng. J.* **2017**, 313, 1623.
- [252] R. Dang, X. Jia, X. Liu, H. Ma, H. Gao, G. Wang, *Nat. Energy* **2017**, 33, 427.
- [253] Y. Kong, R. Jiao, H. Li, S. Xu, C. Cui, S. Zeng, L. Wang, *J. Alloys Compd.* **2020**, 843, 156005.
- [254] Y. Dong, X. Jiang, J. Mo, Y. Zhou, J. Zhou, *Chem. Eng. J.* **2020**, 381, 122614.
- [255] S. Mallakpour, E. Azadi, C. Mustansar Hussain, *Coord. Chem. Rev.* **2020**, 419, 213378.
- [256] W. Yang, J. Wang, W. Ma, C. Dong, G. Cheng, Z. Zhang, *J. Power Sources* **2016**, 333, 88.
- [257] B. Pecquenard, F. Le Cras, D. Poinot, O. Sicardy, J.-P. Manaud, *ACS Appl. Mater. Interfaces* **2014**, 6, 3413.
- [258] W. Chen, H. Zhang, Z. Ma, B. Yang, Z. Li, *J. Mater. Chem. A* **2015**, 3, 14202.
- [259] S. Mohapatra, S. V. Nair, D. Santhanagopalan, A. K. Rai, *Electrochim. Acta* **2016**, 206, 217.
- [260] X. Liu, G. Liu, L. Wang, Y. Li, Y. Ma, J. Ma, *J. Power Sources* **2016**, 312, 199.
- [261] Y. Liu, L. Xiong, P. Li, H. Fu, Z. Hou, L. Zhu, W. Li, *J. Power Sources* **2019**, 428, 20.
- [262] F. Pu, C. Kong, J. Lv, BoMa, W. Zhang, X. Zhang, S. Yang, H. Jin, Z. Yang, *J. Alloys Compd.* **2019**, 805, 355.
- [263] J. Ha, Y.-T. Kim, J. Choi, *ChemSusChem* **2020**, 13, 419.
- [264] S. Liu, S. Zhang, Y. Xing, S. Wang, R. Lin, X. Wei, L. He, *Electrochim. Acta* **2014**, 150, 75.
- [265] S. M. Pawar, B. S. Pawar, B. Hou, A. T. A. Ahmad, H. S. Chavan, Y. Jo, S. Cho, J. Kim, J. Seo, S. Cha, A. I. Inamdar, H. Kim, H. Im, *J. Ind. Eng. Chem.* **2019**, 69, 13.
- [266] J. Li, Y. Zhang, L. Li, L. Cheng, S. Dai, F. Wang, Y. Wang, X.-Y. Yu, *Sustainable Energy Fuels* **2019**, 3, 3370.
- [267] K. Jiang, Z. Chen, X. Meng, *ChemElectroChem* **2019**, 6, 2825.
- [268] Y. Liu, Y. Li, H. Kang, T. Jin, L. Jiao, *Mater. Horiz.* **2016**, 3, 402.
- [269] Y. Du, Z. Yin, J. Zhu, X. Huang, X.-J. Wu, Z. Zeng, Q. Yan, H. Zhang, *Nat. Commun.* **2012**, 3, 1177.
- [270] X. Wang, Y. Wang, X. Li, B. Liu, J. Zhao, *J. Power Sources* **2015**, 281, 185.
- [271] S. Iqbal, A. Bahadur, A. Saeed, K. Zhou, M. Shoaib, M. Waqas, *J. Colloid Interface Sci.* **2017**, 502, 16.
- [272] H. Qing, R. Wang, Z. Chen, M. Li, L. Zhang, Y.-N. Zhou, R. Wu, *J. Colloid Interface Sci.* **2020**, 566, 1.
- [273] S. Li, P. Ge, F. Jiang, C. W. Foster, C. E. Banks, W. Xu, Y. Zhang, W. Hong, C. Zhang, W. Sun, J. Hu, H. Hou, Y. Hu, X. Ji, *ACS Appl. Mater. Interfaces* **2018**, 10, 43669.
- [274] H. Liu, Y. He, H. Zhang, K. Cao, S. Wang, Y. Jiang, Q.-S. Jing, L. Jiao, *Chem. Eng. J.* **2021**, 425, 130548.
- [275] T. Lu, Y. Zhang, C. Cheng, Y. Wang, Y. Zhu, *Front. Chem. Sci. Eng.* **2020**, 14, 595.
- [276] Y. Liu, D. Lin, Y. Li, G. Chen, A. Pei, O. Nix, Y. Li, Y. Cui, *Nat. Commun.* **2018**, 9, 3656.
- [277] Y. Kim, B. J. Wieder, C. L. Kane, A. M. Rappe, *Phys. Rev. Lett.* **2015**, 115, 036806.
- [278] F. Gulo, A. Simon, J. Köhler, R. K. Kremer, *Angew. Chem., Int. Ed.* **2004**, 43, 2032.
- [279] J. Wang, F. Li, X. Liu, H. Zhou, X. Shao, Y. Qu, M. Zhao, *J. Mater. Chem. A* **2017**, 5, 8762.
- [280] S. Zhou, P. Huang, T. Xiong, F. Yang, H. Yang, Y. Huang, D. Li, J. Deng, M. S. Balogun, *Small* **2021**, 17, 2100778.
- [281] S. Ni, B. Zheng, J. Liu, D. Chao, X. Yang, Z. Shen, J. Zhao, *J. Mater. Chem. A* **2018**, 6, 18821.
- [282] M. S. Chandrasekar, S. Mitra, *Electrochim. Acta* **2013**, 92, 47.
- [283] V. Yarmiayev, Y. Miroshnikov, G. Gershinsky, V. Shokhen, D. Zitoun, *Electrochim. Acta* **2018**, 292, 846.
- [284] A. F. Harper, M. L. Evans, A. J. Morris, *Chem. Mater.* **2020**, 32, 6629.
- [285] J. Li, X. Li, P. Liu, X. Zhu, R. N. Ali, H. Naz, Y. Yu, B. Xiang, *ACS Appl. Mater. Interfaces* **2019**, 11, 11442.
- [286] L. De Trizio, A. Figuerola, L. Manna, A. Genovese, C. George, R. Brescia, Z. Saghi, R. Simonutti, M. Van Huis, A. Falqui, *ACS Nano* **2012**, 6, 32.
- [287] Y. Xie, Y. Dall'Agnese, M. Naguib, Y. Gogotsi, M. W. Barsoum, H. L. Zhuang, P. R. C. Kent, *ACS Nano* **2014**, 8, 9606.
- [288] G. Manna, R. Bose, N. Pradhan, *Angew. Chem., Int. Ed.* **2013**, 52, 6762.
- [289] J. Zhu, Q. Wu, J. Key, M. Wu, P. K. Shen, *Energy Storage Mater.* **2018**, 15, 75.
- [290] H.-J. Peng, G.-X. Hao, Z.-H. Chu, C.-L. He, X.-M. Lin, Y.-P. Cai, *J. Alloys Compd.* **2017**, 727, 1020.
- [291] T. Li, Y. Bai, Y. Wang, H. Xu, H. Jin, *Coord. Chem. Rev.* **2020**, 410, 213221.
- [292] L. Wang, X. Wang, Z. Meng, H. Hou, B. Chen, *J. Mater. Sci.* **2017**, 52, 7140.
- [293] D. Wang, D. Choi, J. Li, Z. Yang, Z. Nie, R. Kou, D. Hu, C. Wang, L. V. Saraf, J. Zhang, I. A. Aksay, J. Liu, *ACS Nano* **2009**, 3, 907.
- [294] Z. Guo, M. V. Reddy, B. M. Goh, A. K. P. San, Q. Bao, K. P. Loh, *RSC Adv.* **2013**, 3, 19051.
- [295] Y. Han, P. Qi, X. Feng, S. Li, X. Fu, H. Li, Y. Chen, J. Zhou, X. Li, B. Wang, *ACS Appl. Mater. Interfaces* **2015**, 7, 2178.
- [296] A. Nazir, H. T. T. Le, A. Kasbe, C.-J. Park, *Chem. Eng. J.* **2021**, 405, 126963.
- [297] G. Zheng, Z. Xing, X. Gao, C. Nie, Z. Xu, Z. Ju, *Appl. Surf. Sci.* **2021**, 559, 149701.
- [298] A. Y. Kim, M. K. Kim, K. Cho, J.-Y. Woo, Y. Lee, S.-H. Han, D. Byun, W. Choi, J. K. Lee, *ACS Appl. Mater. Interfaces* **2016**, 8, 19514.
- [299] S. Guo, J. Yi, Y. Sun, H. Zhou, *Energy Environ. Sci.* **2016**, 9, 2978.
- [300] X. Rui, X. Zhang, S. Xu, H. Tan, Y. Jiang, L. Y. Gan, Y. Feng, C. C. Li, Y. Yu, *Adv. Funct. Mater.* **2021**, 31, 2009458.
- [301] Y. Xu, M. Zhou, Y. Lei, *Adv. Energy Mater.* **2016**, 6, 1502514.

- [302] Y. You, A. Manthiram, *Adv. Energy Mater.* **2018**, *8*, 1701785.
- [303] T. Wang, D. Su, D. Shanmukaraj, T. Rojo, M. Armand, G. Wang, *Electrochim. Eng. Energy* **2018**, *1*, 200.
- [304] S. Yuan, X.-l. Huang, D.-l. Ma, H.-g. Wang, F.-z. Meng, X.-b. Zhang, *Adv. Mater.* **2014**, *26*, 2273.
- [305] Y. Xiao, X. Zhao, X. Wang, D. Su, S. Bai, W. Chen, S. Fang, L. Zhou, H.-M. Cheng, F. Li, *Adv. Energy Mater.* **2020**, *10*, 2000666.
- [306] M. Fan, Y. Chen, Y. Xie, T. Yang, X. Shen, N. Xu, H. Yu, C. Yan, *Adv. Funct. Mater.* **2016**, *26*, 5019.
- [307] F. Li, Z. Zhou, *Small* **2018**, *14*, 1702961.
- [308] M. Fan, H. Yu, Y. Chen, *Mater. Technol.* **2017**, *32*, 598.
- [309] P. C. Rath, J. Patra, D. Saikia, M. Mishra, C.-M. Tseng, J.-K. Chang, H.-M. Kao, *ACS Sustainable Chem. Eng.* **2018**, *6*, 10876.
- [310] W. Zhao, L. Gao, L. Yue, X. Wang, Q. Liu, Y. Luo, T. Li, X. Shi, A. M. Asiri, X. Sun, *J. Mater. Chem. A* **2021**, *9*, 6402.
- [311] J. Li, D. Yan, T. Lu, W. Qin, Y. Yao, L. Pan, *ACS Appl. Mater. Interfaces* **2017**, *9*, 2309.
- [312] N. R. Kim, J. Choi, H. J. Yoon, M. E. Lee, S. U. Son, H.-J. Jin, Y. S. Yun, *ACS Sustainable Chem. Eng.* **2017**, *5*, 9802.
- [313] Y. Gong, J. Zhao, H. Wang, J. Xu, *Electrochim. Acta* **2018**, *292*, 895.
- [314] B. Wang, J.-Y. Xue, F.-L. Li, H. Geng, J.-P. Lang, *ChemSusChem* **2021**, *14*, 5304.
- [315] J.-L. Yue, Q. Sun, Z.-W. Fu, *Chem. Commun.* **2013**, *49*, 5868.
- [316] H. Lin, M. Li, X. Yang, D. Yu, Y. Zeng, C. Wang, G. Chen, F. Du, *Adv. Energy Mater.* **2019**, *9*, 1900323.
- [317] D. Yu, X. Wei, D. Zhao, S. Gao, G. Zhao, H. Zhang, Z. Li, M. Yu, Y. Sun, *Electrochim. Acta* **2022**, *404*, 139703.
- [318] Z. Hu, Q. Liu, W. Lai, Q. Gu, L. Li, M. Chen, W. Wang, S.-L. Chou, Y. Liu, S.-X. Dou, *Adv. Energy Mater.* **2020**, *10*, 1903542.
- [319] Q. Li, D. Yang, H. Chen, X. Lv, Y. Jiang, Y. Feng, X. Rui, Y. Yu, *SusMat* **2021**, *1*, 359.
- [320] W.-J. Li, S.-L. Chou, J.-Z. Wang, H.-K. Liu, S.-X. Dou, *Chem. Commun.* **2015**, *51*, 3682.
- [321] J. Zhu, Q. He, Y. Liu, J. Key, S. Nie, M. Wu, P. K. Shen, *J. Mater. Chem. A* **2019**, *7*, 16999.
- [322] Y. Yin, Y. Zhang, N. Liu, L. Fan, N. Zhang, *Energy Environ. Mater.* **2020**, *3*, 529.
- [323] H. Kim, J. C. Kim, M. Bianchini, D.-H. Seo, J. Rodriguez-Garcia, G. Ceder, *Adv. Energy Mater.* **2018**, *8*, 1702384.
- [324] T. Hosaka, K. Kubota, A. S. Hameed, S. Komaba, *Chem. Rev.* **2020**, *120*, 6358.
- [325] Z. Zhang, M. Li, Y. Gao, Z. Wei, M. Zhang, C. Wang, Y. Zeng, B. Zou, G. Chen, F. Du, *Adv. Funct. Mater.* **2018**, *28*, 1802684.
- [326] R. Rajagopalan, Y. Tang, X. Ji, C. Jia, H. Wang, *Adv. Funct. Mater.* **2020**, *30*, 1909486.
- [327] W. Zhang, Y. Liu, Z. Guo, *Sci. Adv.* **2019**, *5*, eaav7412.
- [328] P. Liu, D. Mitlin, *Acc. Chem. Res.* **2020**, *53*, 1161.
- [329] L. Gao, Z. Wang, H. Hu, H. Cheng, L. Zhang, X. Yang, *J. Electroanal. Chem.* **2020**, *876*, 114483.
- [330] K. Cao, H. Liu, W. Li, Q. Han, Z. Zhang, K. Huang, Q. Jing, L. Jiao, *Small* **2019**, *15*, 1901775.
- [331] C. Nithya, G. Thiyagaraj, *Sustainable Energy Fuels* **2020**, *4*, 3574.
- [332] H. Lin, J. Liu, M. Li, N. Chen, W. Xuan, L. Liu, S. Yao, F. Du, *ACS Appl. Mater. Interfaces* **2021**, *13*, 58763.
- [333] K. Cao, R. Zheng, S. Wang, J. Shu, X. Liu, H. Liu, K.-J. Huang, Q.-S. Jing, L. Jiao, *Adv. Funct. Mater.* **2020**, *30*, 2007712.
- [334] J. Cao, J. Li, D. Li, Z. Yuan, Y. Zhang, V. Shulga, Z. Sun, W. Han, *Nano-Micro Lett.* **2021**, *13*, 113.
- [335] W. Ren, F. Xiong, Y. Fan, Y. Xiong, Z. Jian, *ACS Appl. Mater. Interfaces* **2020**, *12*, 10471.
- [336] Z. Guo, S. Zhao, T. Li, D. Su, S. Guo, G. Wang, *Adv. Energy Mater.* **2020**, *10*, 1903591.
- [337] Z. Wang, Y. Zhu, C. Qiao, S. Yang, J. Jia, S. Rafai, X. Ma, S. Wu, F. Ji, C. Cao, *Small* **2019**, *15*, 1902797.
- [338] Z. Wang, Y. Zhu, H. Peng, C. Du, X. Ma, C. Cao, *Electrochim. Acta* **2021**, *374*, 137965.
- [339] Z. Wang, S. Rafai, C. Qiao, J. Jia, Y. Zhu, X. Ma, C. Cao, *ACS Appl. Mater. Interfaces* **2019**, *11*, 7046.
- [340] J. Huang, Y. Zhu, C. Du, Z. Han, X. Yao, X. Yang, Y. Cao, Y. Zhang, X. Ma, C. Cao, *Electrochim. Acta* **2021**, *388*, 138619.
- [341] F. Xiong, Y. Fan, S. Tan, L. Zhou, Y. Xu, C. Pei, Q. An, L. Mai, *Nat. Energy* **2018**, *47*, 210.
- [342] Z. Wang, Y. Zhang, H. Peng, C. Du, Z. Han, X. Ma, Y. Zhu, C. Cao, *Electrochim. Acta* **2022**, *407*, 139786.
- [343] Y. Shen, Y. Wang, Y. Miao, M. Yang, X. Zhao, X. Shen, *Adv. Mater.* **2020**, *32*, 1905524.
- [344] D. Chen, Y. Zhang, X. Li, J. Shen, Z. Chen, S.-a. Cao, T. Li, F. Xu, *Chem. Eng. J.* **2020**, *384*, 123235.
- [345] X. Xue, R. Chen, X. Song, A. Tao, W. Yan, W. Kong, Z. Jin, *Adv. Funct. Mater.* **2021**, *31*, 2009394.
- [346] Y. Zhang, Y. Zhu, Z. Wang, H. Peng, X. Yang, Y. Cao, C. Du, X. Ma, C. Cao, *Adv. Funct. Mater.* **2021**, *31*, 2104730.
- [347] T. Cai, L. Zhao, H. Hu, T. Li, X. Li, S. Guo, Y. Li, Q. Xue, W. Xing, Z. Yan, L. Wang, *Energy Environ. Sci.* **2018**, *11*, 2341.
- [348] X. Zhang, G. Zhang, S. Wang, S. Li, S. Jiao, *J. Mater. Chem. A* **2018**, *6*, 3084.
- [349] S. Wang, S. Jiao, J. Wang, H.-S. Chen, D. Tian, H. Lei, D.-N. Fang, *ACS Nano* **2017**, *11*, 469.
- [350] G. Li, J. Tu, M. Wang, S. Jiao, *J. Mater. Chem. A* **2019**, *7*, 8368.
- [351] G. Li, M. Kou, J. Tu, Y. Luo, M. Wang, S. Jiao, *Chem. Eng. J.* **2021**, *421*, 127792.
- [352] Y. Wang, C. Wang, X. Yi, Y. Hu, L. Wang, L. Ma, G. Zhu, T. Chen, Z. Jin, *Energy Storage Mater.* **2019**, *23*, 741.
- [353] H. D. Yoo, Y. Liang, Y. Li, Y. Yao, *ACS Appl. Mater. Interfaces* **2015**, *7*, 7001.
- [354] W. Wang, Y. Yang, Y. NuLi, J. Zhou, J. Yang, J. Wang, *J. Power Sources* **2020**, *445*, 227325.
- [355] H. Yuan, N. Wang, Y. NuLi, J. Yang, J. Wang, *Electrochim. Acta* **2018**, *261*, 503.
- [356] Y. Zhang, Y. Li, Y. Wang, R. Guo, W. Liu, H. Pei, G. Yin, D. Ye, S. Yu, J. Xie, *J. Colloid Interface Sci.* **2019**, *553*, 239.
- [357] X. Hou, H. Shi, T. Chang, K. Hou, L. Feng, G. Suo, X. Ye, L. Zhang, Y. Yang, W. Wang, *Chem. Eng. J.* **2021**, *409*, 128271.
- [358] W. Zhao, X. Wang, X. Ma, L. Yue, Y. Ren, T. Li, J. Xia, L. Zhang, Q. Liu, Y. Luo, N. Li, B. Tang, Y. Liu, S. Gao, A. M. Asiri, X. Sun, *J. Mater. Chem. A* **2021**, *9*, 27615.
- [359] H. Jin, C. Guo, X. Liu, J. Liu, A. Vasileff, Y. Jiao, Y. Zheng, S.-Z. Qiao, *Chem. Rev.* **2018**, *118*, 6337.
- [360] Y. Sun, S. Gao, F. Lei, Y. Xie, *Chem. Soc. Rev.* **2015**, *44*, 623.
- [361] Y. Zheng, X. Li, C. Pi, H. Song, B. Gao, P. K. Chu, K. Huo, *FlatChem* **2020**, *19*, 100149.
- [362] Y. Sun, F. Lei, S. Gao, B. Pan, J. Zhou, Y. Xie, *Angew. Chem., Int. Ed.* **2013**, *52*, 10569.
- [363] S. Anantharaj, T. S. Amarnath, E. Subhashini, S. Chatterjee, K. C. Swaathini, K. Karthick, S. Kundu, *ACS Catal.* **2018**, *8*, 5686.
- [364] D. Chinnadurai, R. Rajendiran, P. Kandasamy, *J. Colloid Interface Sci.* **2022**, *606*, 101.
- [365] Z. Tan, T. Peng, X. Tan, W. Wang, X. Wang, Z. Yang, H. Ning, Q. Zhao, M. Wu, *ChemElectroChem* **2020**, *7*, 2020.
- [366] L. Pan, S. Sun, Y. Chen, P. Wang, J. Wang, X. Zhang, J.-J. Zou, Z. L. Wang, *Adv. Energy Mater.* **2020**, *10*, 2000214.
- [367] W. Qian, S. Xu, X. Zhang, C. Li, W. Yang, C. R. Bowen, Y. Yang, *Nano-Micro Lett.* **2021**, *13*, 156.
- [368] S. Xu, W. Qian, D. Zhang, X. Zhao, X. Zhang, C. Li, C. R. Bowen, Y. Yang, *Nat. Energy* **2020**, *77*, 105305.
- [369] I. A. Rutkowska, A. Wadas, E. Szaniawska, A. Chmielnicka, A. Zlotorowicz, P. J. Kulesza, *Curr. Opin. Electrochem.* **2020**, *23*, 131.

- [370] E. Kano, D. G. Kvashnin, S. Sakai, L. A. Chernozatonskii, P. B. Sorokin, A. Hashimoto, M. Takeguchi, *Nanoscale* **2017**, *9*, 3980.
- [371] Y. Liu, Y. Deng, Z. Sun, J. Wei, G. Zheng, A. M. Asiri, S. B. Khan, M. M. Rahman, D. Zhao, *Small* **2013**, *9*, 2702.
- [372] L. Isac, C. Cazan, L. Andronic, A. Enesca, *Catalysts* **2022**, *12*, 1135.
- [373] X. Wang, Z. Miao, Y. Ma, H. Chen, H. Qian, Z. Zha, *Nanoscale* **2017**, *9*, 14512.
- [374] M. L. Liu, B. B. Chen, R. S. Li, C. M. Li, H. Y. Zou, C. Z. Huang, *ACS Sustainable Chem. Eng.* **2017**, *5*, 4154.
- [375] K. Rajeshwar, M. K. Hossain, R. T. Macaluso, C. Janáky, A. Varga, P. J. Kulesza, *J. Electrochem. Soc.* **2018**, *165*, H3192.
- [376] H. Haroon, M. Wahid, K. Majid, *ACS Appl. Nano Mater.* **2022**, *5*, 2006.
- [377] Y. Zhong, S. Wang, M. Li, J. Ma, S. Song, A. Kumar, H. Duan, Y. Kuang, X. Sun, *Mater. Today Phys.* **2021**, *18*, 100354.
- [378] Q. Liu, Q. Li, S. Chen, *Curr. Opin. Electrochem.* **2020**, *21*, 46.
- [379] W. Zhu, S. Chen, *Electroanalysis* **2020**, *32*, 2591.
- [380] D. Zhu, M. Qiao, J. Liu, T. Tao, C. Guo, *J. Mater. Chem. A* **2020**, *8*, 8143.
- [381] H. Wang, J.-M. Lee, *J. Mater. Chem. A* **2020**, *8*, 10604.
- [382] L. Zhang, Z.-J. Zhao, J. Gong, *Angew. Chem., Int. Ed.* **2017**, *56*, 11326.
- [383] J. Zhao, S. Xue, J. Barber, Y. Zhou, J. Meng, X. Ke, *J. Mater. Chem. A* **2020**, *8*, 4700.
- [384] P. G. Bruce, S. A. Freunberger, L. J. Hardwick, J.-M. Tarascon, *Nat. Mater.* **2012**, *11*, 19.
- [385] J. Pan, Y. Y. Xu, H. Yang, Z. Dong, H. Liu, B. Y. Xia, *Adv. Sci.* **2018**, *5*, 1700691.
- [386] R. Cao, J.-S. Lee, M. Liu, J. Cho, *Adv. Energy Mater.* **2012**, *2*, 816.
- [387] Q. Hong, H. Lu, J. Wang, *ACS Sustainable Chem. Eng.* **2017**, *5*, 9169.
- [388] Y. Guan, N. Li, Y. Li, L. Sun, Y. Gao, Q. Zhang, C. He, J. Liu, X. Ren, *Nanoscale* **2020**, *12*, 14259.
- [389] Y. Liu, Y. Liu, H. Shi, M. Wang, S. H.-S. Cheng, H. Bian, M. Kamruzzaman, L. Cao, C. Y. Chung, Z. Lu, *J. Alloys Compd.* **2016**, *688*, 380.
- [390] J. Zhang, B. Sun, A. M. McDonagh, Y. Zhao, K. Kretschmer, X. Guo, G. Wang, *Energy Storage Mater.* **2017**, *7*, 1.
- [391] J. Tang, Y. Ge, J. Shen, M. Ye, *Chem. Commun.* **2016**, *52*, 1509.
- [392] K. Song, W. Ai, Y. Zhang, Y. Zeng, Y. Yu, H. Qiao, Z. Liu, X. Shen, X. Hu, X. Hu, *J. Mater. Chem. A* **2021**, *9*, 3007.
- [393] F. Niu, N. Wang, J. Yue, L. Chen, J. Yang, Y. Qian, *Electrochim. Acta* **2016**, *208*, 148.
- [394] Y. Huang, Y. Jiang, L. Zou, J. Cheng, B. Chi, J. Pu, J. Li, *J. Electrochem. Soc.* **2017**, *164*, A3896.
- [395] S. Zhao, Y. Wang, Q. Zhang, Y. Li, L. Gu, Z. Dai, S. Liu, Y.-Q. Lan, M. Han, J. Bao, *Inorg. Chem. Front.* **2016**, *3*, 1501.
- [396] Z. Hou, J. Long, C. Shu, R. Liang, J. Li, X. Liao, *J. Alloys Compd.* **2019**, *798*, 560.
- [397] J. Long, Z. Hou, C. Shu, C. Han, W. Li, R. Huang, J. Wang, *ACS Appl. Mater. Interfaces* **2019**, *11*, 3834.
- [398] Y. Li, J. Yin, L. An, M. Lu, K. Sun, Y.-Q. Zhao, F. Cheng, P. Xi, *Nanoscale* **2018**, *10*, 6581.
- [399] H. Cheng, M.-L. Li, C.-Y. Su, N. Li, Z.-Q. Liu, *Adv. Funct. Mater.* **2017**, *27*, 1701833.
- [400] Z. Pan, H. Chen, J. Yang, Y. Ma, Q. Zhang, Z. Kou, X. Ding, Y. Pang, L. Zhang, Q. Gu, C. Yan, J. Wang, *Adv. Sci.* **2019**, *6*, 1900628.
- [401] R. Zhang, Z. Hu, S. Cheng, W. Ke, T. Ning, J. Wu, X. Fu, G. Zhu, *Inorg. Chem.* **2021**, *60*, 6721.
- [402] L.-M. Cao, D. Lu, D.-C. Zhong, T.-B. Lu, *Coord. Chem. Rev.* **2020**, *407*, 213156.
- [403] J. Zhang, Q. Zhang, X. Feng, *Adv. Mater.* **2019**, *31*, 1808167.
- [404] G. Zhao, K. Rui, S. X. Dou, W. Sun, *Adv. Funct. Mater.* **2018**, *28*, 1803291.
- [405] S. Li, M. Li, Y. Ni, *Appl. Catal., B* **2020**, *268*, 118392.
- [406] A. Y. Faïd, A. O. Barnett, F. Seland, S. Sunde, *Electrochim. Acta* **2021**, *371*, 137837.
- [407] Y. Xu, H. Wang, R. Zhu, C. Liu, X. Wu, B. Zhang, *Chem. - Asian J.* **2013**, *8*, 1120.
- [408] L. An, P. Zhou, J. Yin, H. Liu, F. Chen, H. Liu, Y. Du, P. Xi, *Inorg. Chem.* **2015**, *54*, 3281.
- [409] Y. Deng, A. D. Handoko, Y. Du, S. Xi, B. S. Yeo, *ACS Catal.* **2016**, *6*, 2473.
- [410] S. M. Pawar, B. S. Pawar, B. Hou, J. Kim, A. T. Aqueel Ahmed, H. S. Chavan, Y. Jo, S. Cho, A. I. Inamdar, J. L. Gunjakar, H. Kim, S. Cha, H. Im, *J. Mater. Chem. A* **2017**, *5*, 12747.
- [411] Q. Liu, Q. Liu, X. Kong, *ACS Appl. Nano Mater.* **2019**, *2*, 6000.
- [412] A. T. Aqueel Ahmed, S. M. Pawar, A. I. Inamdar, H. Kim, H. Im, *Adv. Mater. Interfaces* **2020**, *7*, 1901515.
- [413] P. Zhang, H. He, *J. Alloys Compd.* **2020**, *826*, 153993.
- [414] S.-Q. Liu, H.-R. Wen, G. Ying, Y.-W. Zhu, X.-Z. Fu, R. Sun, C.-P. Wong, *Nat. Energy* **2018**, *44*, 7.
- [415] K. Cho, S.-H. Han, M. P. Suh, *Angew. Chem., Int. Ed.* **2016**, *55*, 15301.
- [416] L. He, D. Zhou, Y. Lin, R. Ge, X. Hou, X. Sun, C. Zheng, *ACS Catal.* **2018**, *8*, 3859.
- [417] G. Shi, Z. Fan, L. Du, X. Fu, C. Dong, W. Xie, D. Zhao, M. Wang, M. Yuan, *Mater. Chem. Front.* **2019**, *3*, 821.
- [418] G. Hai, X. Jia, K. Zhang, X. Liu, Z. Wu, G. Wang, *Nat. Energy* **2018**, *44*, 345.
- [419] J. Rong, J. Xu, F. Qiu, Y. Fang, T. Zhang, Y. Zhu, *Electrochim. Acta* **2019**, *323*, 134856.
- [420] S. Peng, L. Li, X. Han, W. Sun, M. Srinivasan, S. G. Mhaisalkar, F. Cheng, Q. Yan, J. Chen, S. Ramakrishna, *Angew. Chem., Int. Ed.* **2014**, *53*, 12594.
- [421] M. Li, Y. Qian, J. Du, H. Wu, L. Zhang, G. Li, K. Li, W. Wang, D. J. Kang, *ACS Sustainable Chem. Eng.* **2019**, *7*, 14016.
- [422] S. Swathi, R. Yuvakkumar, G. Ravi, S. I. Hong, D. Velauthapillai, M. Thambidurai, C. Dang, A. M. Al-Mohaimeed, W. A. Al-onazi, *Int. J. Hydrogen Energy* **2021**, *46*, 3387.
- [423] L. Yang, X. Zeng, W. Wang, D. Cao, *Adv. Funct. Mater.* **2018**, *28*, 1704537.
- [424] J. Kundu, S. Khilari, K. Bhunia, D. Pradhan, *Catal. Sci. Technol.* **2019**, *9*, 406.
- [425] J. Chen, M. Gu, S. Liu, T. Sheng, X. Zhang, *ACS Appl. Mater. Interfaces* **2021**, *13*, 16210.
- [426] N. Zang, Z. Wu, J. Wang, W. Jin, *J. Mater. Chem. A* **2020**, *8*, 1799.
- [427] Y. Liu, C. Xiao, M. Lyu, Y. Lin, W. Cai, P. Huang, W. Tong, Y. Zou, Y. Xie, *Angew. Chem., Int. Ed.* **2015**, *54*, 11231.
- [428] M. Chauhan, K. P. Reddy, C. S. Gopinath, S. Deka, *ACS Catal.* **2017**, *7*, 5871.
- [429] Z. Hao, P. Wei, Y. Yang, J. Sun, Y. Song, D. Guo, L. Liu, *Appl. Surf. Sci.* **2021**, *536*, 147826.
- [430] P. D. Tran, M. Nguyen, S. S. Pramana, A. Bhattacharjee, S. Y. Chiam, J. Fize, M. J. Field, V. Artero, L. H. Wong, J. Loo, J. Barber, *Energy Environ. Sci.* **2012**, *5*, 8912.
- [431] A. P. Tiwari, D. Kim, Y. Kim, O. Prakash, H. Lee, *Nat. Energy* **2016**, *28*, 366.
- [432] A. P. Tiwari, A. Azam, T. G. Novak, O. Prakash, S. Jeon, *J. Mater. Chem. A* **2018**, *6*, 7786.
- [433] Q. Wu, Y. Ma, R. Peng, B. Huang, Y. Dai, *ACS Appl. Mater. Interfaces* **2019**, *11*, 45818.
- [434] D. C. Nguyen, D. T. Tran, T. L. L. Doan, D. H. Kim, N. H. Kim, J. H. Lee, *Adv. Energy Mater.* **2020**, *10*, 1903289.
- [435] J. Hao, W. Yang, Z. Huang, C. Zhang, *Adv. Mater. Interfaces* **2016**, *3*, 1600236.

- [436] A. Han, H. Zhang, R. Yuan, H. Ji, P. Du, *ACS Appl. Mater. Interfaces* **2017**, *9*, 2240.
- [437] X. Zhang, M. Han, G. Liu, G. Wang, Y. Zhang, H. Zhang, H. Zhao, *Appl. Catal., B* **2019**, *244*, 899.
- [438] J. Lin, Y. Yan, T. Xu, J. Cao, X. Zheng, J. Feng, J. Qi, *J. Colloid Interface Sci.* **2020**, *564*, 37.
- [439] Y. Liu, Y. Yang, B. Chen, X. Li, M. Guo, Y. Yang, K. Xu, C. Yuan, *Inorg. Chem.* **2021**, *60*, 18325.
- [440] C. Tong, R. Xiang, L. Peng, L. Tan, X. Tang, J. Wang, L. Li, Q. Liao, Z. Wei, *J. Mater. Chem. A* **2020**, *8*, 3351.
- [441] D. D. Zhu, J. L. Liu, S. Z. Qiao, *Adv. Mater.* **2016**, *28*, 3423.
- [442] D. Karapinar, C. E. Creissen, J. G. Rivera de la Cruz, M. W. Schreiber, M. Fontecave, *ACS Energy Lett.* **2021**, *6*, 694.
- [443] S. Popović, M. Smiljanić, P. Jovanović, J. Vavra, R. Buonsanti, N. Hodnik, *Angew. Chem., Int. Ed.* **2020**, *59*, 14736.
- [444] Y. Wang, J. Liu, G. Zheng, *Adv. Mater.* **2021**, *33*, 2005798.
- [445] J.-Y. Li, L. Yuan, S.-H. Li, Z.-R. Tang, Y.-J. Xu, *J. Mater. Chem. A* **2019**, *7*, 8676.
- [446] L. Lv, X. He, J. Wang, Y. Ruan, S. Ouyang, H. Yuan, T. Zhang, *Appl. Catal., B* **2021**, *298*, 120531.
- [447] B. Zhang, J. Zhang, M. Hua, Q. Wan, Z. Su, X. Tan, L. Liu, F. Zhang, G. Chen, D. Tan, X. Cheng, B. Han, L. Zheng, G. Mo, *J. Am. Chem. Soc.* **2020**, *142*, 13606.
- [448] D. Wang, J. Xu, Y. Zhu, L. Wen, J. Ye, Y. Shen, T. Zeng, X. Lu, J. Ma, L. Wang, S. Song, *Chemosphere* **2021**, *278*, 130408.
- [449] K. P. Kuhl, E. R. Cave, D. N. Abram, T. F. Jaramillo, *Energy Environ. Sci.* **2012**, *5*, 7050.
- [450] Y. Wang, H. Liu, J. Yu, B. Hu, H. Zhao, P. Tsiakaras, S. Song, *Electrochim. Acta* **2019**, *328*, 135083.
- [451] A. S. Varela, M. Kroschel, T. Reier, P. Strasser, *Catal. Today* **2016**, *260*, 8.
- [452] Y. Pang, T. Burdyny, C.-T. Dinh, M. G. Kibria, J. Z. Fan, M. Liu, E. H. Sargent, D. Sinton, *Green Chem.* **2017**, *19*, 4023.
- [453] D. Gao, I. T. McCrum, S. Deo, Y.-W. Choi, F. Scholten, W. Wan, J. G. Chen, M. J. Janik, B. Roldan Cuenya, *ACS Catal.* **2018**, *8*, 10012.
- [454] H. Li, K. Shin, G. Henkelman, *J. Chem. Phys.* **2018**, *149*, 174705.
- [455] Z. Xia, S. Guo, *Chem. Soc. Rev.* **2019**, *48*, 3265.
- [456] Y. Lan, G. Niu, F. Wang, D. Cui, Z. Hu, *ACS Appl. Mater. Interfaces* **2020**, *12*, 36128.
- [457] H. Xiao, T. Cheng, W. A. Goddard, *J. Am. Chem. Soc.* **2017**, *139*, 130.
- [458] X. Wang, K. Klingan, M. Klingenhof, T. Möller, J. Ferreira de Araújo, I. Martens, A. Bagger, S. Jiang, J. Rossmeis, H. Dau, P. Strasser, *Nat. Commun.* **2021**, *12*, 794.
- [459] Z. Zhao, X. Peng, X. Liu, X. Sun, J. Shi, L. Han, G. Li, J. Luo, *J. Mater. Chem. A* **2017**, *5*, 20239.
- [460] T. Dou, Y. Qin, F. Zhang, X. Lei, *ACS Appl. Energy Mater.* **2021**, *4*, 4376.
- [461] L. Majidi, A. Ahmadiparidari, N. Shan, S. N. Misal, K. Kumar, Z. Huang, S. Rastegar, Z. Hemmat, X. Zou, P. Zapol, J. Cabana, L. A. Curtiss, A. Salehi-Khojin, *Adv. Mater.* **2021**, *33*, 2004393.
- [462] K. Zhu, X. Zhu, W. Yang, *Angew. Chem., Int. Ed.* **2019**, *58*, 1252.
- [463] J. Wang, J. Tang, *Chemosphere* **2021**, *276*, 130177.
- [464] Y. Lv, B. Shi, Y. Qi, X. Su, I. Liu, L. Tian, J. Ding, *J. Alloys Compd.* **2019**, *773*, 706.
- [465] C. Zhang, W. Lv, G. Zhou, Z. Huang, Y. Zhang, R. Lyu, H. Wu, Q. Yun, F. Kang, Q.-H. Yang, *Adv. Energy Mater.* **2018**, *8*, 1703404.
- [466] Y. Yang, Y. Xiong, R. Zeng, X. Lu, M. Krumov, X. Huang, W. Xu, H. Wang, F. J. DiSalvo, J. D. Brock, D. A. Muller, H. D. Abruña, *ACS Catal.* **2021**, *11*, 1136.
- [467] D. Zhang, Y. Zhu, L. Liu, X. Ying, C.-E. Hsiung, R. Sougrat, K. Li, Y. Han, *Science* **2018**, *359*, 675.
- [468] H. Liu, H. Zheng, L. Li, S. Jia, S. Meng, F. Cao, Y. Lv, D. Zhao, J. Wang, *Adv. Mater. Interfaces* **2018**, *5*, 1701255.
- [469] J. Y. Park, S. J. Kim, K. Yim, K. S. Dae, Y. Lee, K. P. Dao, J. S. Park, H. B. Jeong, J. H. Chang, H. K. Seo, C. W. Ahn, J. M. Yuk, *Adv. Sci.* **2019**, *6*, 1900264.
- [470] Q. Lei, J. Zhang, Z. Liang, Y. Yue, Z. Ren, Y. Sun, Z. Yao, J. Li, Y. Zhao, Y. Yin, P. Huai, Z. Lv, J. Li, Z. Jiang, W. Wen, X. Li, X. Zhou, D. Zhu, *Adv. Energy Mater.* **2022**, *12*, 2200547.
- [471] R. Garcia, *Chem. Soc. Rev.* **2020**, *49*, 5850.
- [472] Y. F. Dufrene, T. Ando, R. Garcia, D. Alsteens, D. Martinez-Martin, A. Engel, C. Gerber, D. J. Müller, *Nat. Nanotechnol.* **2017**, *12*, 295.
- [473] A. M. Tripathi, W.-N. Su, B. J. Hwang, *Chem. Soc. Rev.* **2018**, *47*, 736.
- [474] X. Ma, W. Luo, M. Yan, L. He, L. Mai, *Nat. Energy* **2016**, *24*, 165.
- [475] L. Shi, X. Niu, H. Zhao, M. Lan, *ChemElectroChem* **2017**, *4*, 246.
- [476] W. Li, M. Li, Y. Hu, J. Lu, A. Lushington, R. Li, T. Wu, T.-K. Sham, X. Sun, *Small Methods* **2018**, *2*, 1700341.
- [477] G. Greczynski, L. Hultman, *Prog. Mater. Sci.* **2020**, *107*, 100591.
- [478] G. Greczynski, L. Hultman, *Appl. Surf. Sci.* **2021**, *542*, 148599.
- [479] C.-Y. Tang, R. T. Haasch, S. J. Dillon, *Chem. Commun.* **2016**, *52*, 13257.
- [480] H. Wu, V. W. Or, S. Gonzalez-Calzada, V. H Grassian, *Nanoscale* **2020**, *12*, 19350.
- [481] C. Wang, S. Chen, L. Song, *Adv. Funct. Mater.* **2020**, *30*, 2000869.
- [482] J. Li, R. Güttinger, R. Moré, F. Song, W. Wan, G. R. Patzke, *Chem. Soc. Rev.* **2017**, *46*, 6124.
- [483] J. Yang, S. Muhammad, M. R. Jo, H. Kim, K. Song, D. A. Agyeman, Y.-I. Kim, W.-S. Yoon, Y.-M. Kang, *Chem. Soc. Rev.* **2016**, *45*, 5717.
- [484] H. Mistry, A. S. Varela, C. S. Bonifacio, I. Zegkinoglou, I. Sinev, Y.-W. Choi, K. Kisslinger, E. A. Stach, J. C. Yang, P. Strasser, B. R. Cuenya, *Nat. Commun.* **2016**, *7*, 12123.
- [485] S. Lohumi, S. Lee, H. Lee, B.-K. Cho, *Trends Food Sci. Technol.* **2015**, *46*, 85.
- [486] C. Hess, *Chem. Soc. Rev.* **2021**, *50*, 3519.
- [487] V. Țucureanu, A. Matei, A. M. Avram, *Crit. Rev. Anal. Chem.* **2016**, *46*, 502.
- [488] A. Sarilmaz, M. Can, F. Ozel, *J. Alloys Compd.* **2017**, *699*, 479.
- [489] S. Schlücker, *Angew. Chem., Int. Ed.* **2014**, *53*, 4756.
- [490] Z. Vlčková Živcová, M. Bouša, M. Velický, O. Frank, L. Kavan, *Nanomaterials* **2021**, *11*, 1256.



Xuehua Ren is currently a M.S. candidate at the School of Chemistry and Chemical Engineering, Chongqing University. She received his B.S. degree in chemistry from Guizhou University in 2020. Her research interests focus on 2D porous materials and their applications for supercapacitors and aqueous zinc-ion batteries.



Shaowei Chen received his B.S. degree in Chemistry from the University of Science and Technology of China in 1991, and his M.S. and Ph.D. degrees from Cornell University in 1993 and 1996, respectively. Following a postdoctoral appointment at the University of North Carolina at Chapel Hill, he started his independent career in Southern Illinois University in 1998. In 2004, he moved to UCSC. He is currently a professor of chemistry and the faculty director of the UCSC COSMOS program. His research interests are primarily focused on high-performance catalysts for electrochemical energy conversion and storage, impacts of core–ligand interfacial bonding interactions on nanoparticle charge-transfer dynamics, Janus nanoparticles by interfacial engineering, and antimicrobial activity of functional nanocomposites.



Lingyun Chen received his Ph.D. degree from Nanjing University in 2008. After that, he joined the School of Chemistry and Chemical Engineering, Chongqing University. He is now a full professor at the School of Chemistry and Chemical Engineering, Chongqing University. His research interests focus on 2D porous functional materials and their application for electrochemical energy storage.